Doktorarbeit

Plasmonic enhancement in graphene: A resonance Raman study

Im Fachbereich Physik der Freien Universität Berlin eingereichte Dissertation zur Erlangung des Grades Doctor Rerum Naturalium

Christian Lehmann

Juni 2015

1. Gutachterin: Prof. Dr. Stephanie Reich

2. Gutachter: Prof. Dr. Joachim Heberle

Tag der Einreichung: 24. Juni 2015

Tag der Disputation: 23. Oktober 2015

Eidesstattliche Erklärung

Hiermit versichere ich, Christian Lehmann, dass ich die vorliegende Dissertation mit dem Titel:

"Plasmonic enhancement in graphene: A resonance Raman study"

selbstständig und ausschließlich unter der Zuhilfenahme der angegebenen Hilfsmittel und Hilfen angefertigt habe. Ich versichere des Weiteren, dass diese Arbeit in keinem früheren Promotionsverfahren angenommen oder als ungenügend beurteilt wurde.

Berlin, den 22. Juni 2015

Christian Lehmann

Curriculum Vitae

For reasons of data protection,
the curriculum vitae is not included in the online version.

Curriculum Vitae

For reasons of data protection,
the curriculum vitae is not included in the online version.

FREIE UNIVERSITÄT BERLIN
Fachbereich Physik

Zusammenfassung

Plasmonic enhancement in graphene: A resonance Raman study

von Christian Lehmann

Diese Arbeit untersucht die Interaktion zwischen Graphen und plasmonischen Antennen mittels wellenlängenabhängiger Raman-Streuung. Zunächst wurden die optischen Eigenschaften von plasmonischen Dimerantennen mittels der Finite-Differenzen-Methode im Zeitbereich berechnet. Das Streuverhalten im Nah- und Fernfeld wurde numerisch bestimmt und experimentell mittels Dunkelfeldspektroskopie untersucht. Zusätzlich wurde die Feldverteilung simuliert, der ein Analyt in der Nähe einer plasmonischen Dimerantenne ausgesetzt ist. In dieser Arbeit wurde durchgehend Graphen als Analyt benutzt, um die Verstärkungseigenschaften von dreieckigen und runden Dimerantennen zu analysieren. Bei allen Proben befand sich Graphen auf der Oberfläche der Antennen. Durch die ortsabhängige Abbildung der Intensität des Raman-Signals bei verschiedenen Wellenlängen wurde nachgewiesen, dass plasmonische Antennen eine Verstärkung nur nahe der lokalisierten Oberflächenplasmonenresonanz zeigen. Plasmonische Hotspots wurden mittels wellenlängenabhängiger Raman-Streuung des 2D-Signals von Graphen untersucht. Diese Messungen ergaben scharfe Resonanzen, die durch die etablierte Theorie der oberflächenverstärkten Raman-Streuung nicht erklärt werden konnten. Daher wurde eine neue Theorie der plasmonisch verstärkten Raman-Streuung entwickelt. Diese nutzt eine quantenmechanische Beschreibung des Raman-Prozesses unter Einbeziehung einer plasmonischen Antenne. Die Theorie wurde mittels wellenlängenabhängiger Raman-Streuung an einzelnen Dimerantennen verifiziert. Die Messungen bestätigten die Vorhersagen der neuen Theorie der plasmonisch verstärkten Raman-Streuung. Die beobachtete Verstärkung wird durch das Nahfeld einer plasmonischen Antenne hervorgerufen. Zusätzlich wurden Hinweise darauf gefunden, dass die plasmonische Verstärkung die elektronische Bandstruktur und Phononendispersion von Graphen verändert. Diese Erkenntnisse geben neue Einsichten in die physikalischen Prozesse, die zur Verstärkung des Raman-Signals durch plasmonische Antennen beitragen. Die Erkenntnisse in dieser Arbeit werden langfristig zur Entwicklung extrem sensitiver Sensoren beitragen.

FREIE UNIVERSITÄT BERLIN
Fachbereich Physik

Abstract

Plasmonic enhancement in graphene: A resonance Raman study

by Christian Lehmann

This thesis investigates the interaction between graphene and plasmonic antennas by wavelength-scanned Raman scattering. The optical properties of plasmonic dimer antennas are investigated using numerical simulations with the finite difference time domain method. The scattering behavior of the near and far field was calculated and experimentally verified using dark field spectroscopy. Additionally, the field distribution around a plasmonic dimer antenna was studied to assess the field distribution an analyte is exposed to. Throughout this thesis graphene was used as an analyte to measure the enhancement properties of triangular and cylindrical dimer antennas. All samples were designed with graphene lying on top of the antennas. Using spatial Raman mapping at different wavelengths it was found that plasmonic antennas show enhancement only in the energetic region of their localized surface plasmon resonance (LSPR). Plasmonic hotspots were investigated by wavelength-scanned Raman measurements of the 2D mode of graphene. These measurements revealed sharp resonances that could not be explained by the conventional theory of surface-enhanced Raman scattering. Thus, a new theory of plasmon-enhanced Raman scattering was developed using a quantum mechanical treatment of the Raman process adding a plasmonic antenna. To verify this theory, single dimer antennas were investigated using wavelength-scanned Raman spectroscopy. These measurements confirmed the predictions made by the new theory of plasmon-enhanced Raman scattering. The observed Raman enhancement is caused by the near field around a plasmonic antenna. Additionally, evidence was found that plasmonic enhancement may alter the electronic band structure and phonon dispersion of graphene. All these findings give new insight into the processes involved in the Raman enhancement caused by plasmonic antennas. In the long run they may lead to the development of extremely sensitive sensors.

Contents

Abbreviations

ABC	**A**bsorbing **B**oundary **C**onditions
BEM	**B**oundary **E**lement **M**ethod
CFL	**C**ourant **F**riedrichs **L**ewy
CW	**C**ontinuous **W**ave
DDA	**D**irect **D**ipole **A**pproximation
DFT	**D**ensity **F**unctional **T**heory
EM	**E**lectro **M**agnetic
FDTD	**F**inite **D**ifference **T**ime **D**omain
FEM	**F**inite **E**lement **M**ethod
FWHM	**F**ull **W**idth (at) **H**alf **M**aximum
IR	**I**nfra **R**ed
LD	**L**orentz-**D**rude
LSPR	**L**ocalized **S**urface **P**lasmon **R**esonance
Meep	**M**it **e**lectromagnetic **e**quation **p**ackage
MIT	**M**assachusetts **I**nstitute (of) **T**echnology
MWE	**M**ax**w**ell **E**quation
NSL	**N**ano **S**phere **L**ithography
PDE	**P**artial **D**ifferential **E**quation
PECVD	**P**lasma **E**nhanced **C**hemical **V**apor **D**eposition
SPP	**S**urface **P**lasmon **P**olariton
TE	**T**ransverse **E**lectric
TM	**T**ransverse **M**agnetic
UV	**U**ltra **V**iolet
VIS	**VIS**ual

Symbols

a	characteristic length scale	1
c	speed of light	$\mathrm{m/s^2}$
n	refractive index	1
OD	optical density (logarithmic transmittance)	1
S	Courant factor	$\mathrm{s\,m^{-1}}$
f	frequency	1/s
$\vec{q}$	phonon wave vector	1/cm
$\vec{k}$	wave vector	1/cm
f_n	oscillator strength in LD model	1
$\mathfrak{R}$	Raman tensor	$1/\mathrm{Å}^2$
$\Re(c)$	real part of complex number c	1
$\Im(c)$	imaginary part of complex number c	1

ω	angular frequency	rad/s
ω_n	angular frequency of oscillator n in LD model	rad/s
ω_p	plasmon frequency	rad/s
ω_{sp}	bulk plasmon frequency	rad/s
σ_n	electrical conductivity	S/m
ρ_s	surface charge density	$\mathrm{C/m^2}$
χ	dielectric susceptibility	1
ϵ	electric permittivity	F/m
μ	magnetic permeability	H/m

The history of science shows that theories are perishable. With every new truth that is revealed we get a better understanding of Nature and our conceptions and views are modified.

Nikola Tesla

Chapter 1

Introduction

Many centuries ago painters used small metal particles for their amazing scattering properties, creating the stunning glow which is often found in church window paintings. Metal nanoparticles were being used for this purpose since Roman times [1]. An understanding of the physics involved was given by Gustav Mie in 1908 [2], explaining the extinction spectra and polarization behavior of small spherical metal nanoparticles. Thereafter, interest in the physics of small metal nanoparticles was quite low due to a lack of useful applications. In 1974 Fleischmann et al. [3] observed enhancement of the Raman scattering cross section of pyridine adsorbed on a rough silver surface. This observation was called surface-enhanced Raman scattering (SERS) and through it the detection of small amounts of molecules using Raman spectroscopy became possible [4, 5]. Later on even the detection of a single molecule was demonstrated [6, 7]. All this was achieved without knowing the physics behind this remarkable Raman signal enhancement. For more than 30 years a lot of effort has been put into understanding the physical process boosting the scattering cross section by up to 12 orders of magnitude [5, 8–11]. A theoretical understanding was established which consisted of an electromagnetic part (cf. Ref. [12, 13]) and a chemical part (cf. Ref. [14, 15]) causing the enhancement. The chemical contribution to the amplified signal proved to be small [16]. Thus, research mainly focused on understanding the electromagnetic contribution to SERS. Within the last decade huge advances have been made in understanding the design of nanoantennas (cf. Ref. [17]). This became possible by new developments in the finite difference time domain (FDTD) method. It is used to compute electromagnetic boundary problems [18, 19] and thus the optical properties of arbitrarily shaped nanoantennas. Simultaneously, high-performance computers became available, making such computations possible.

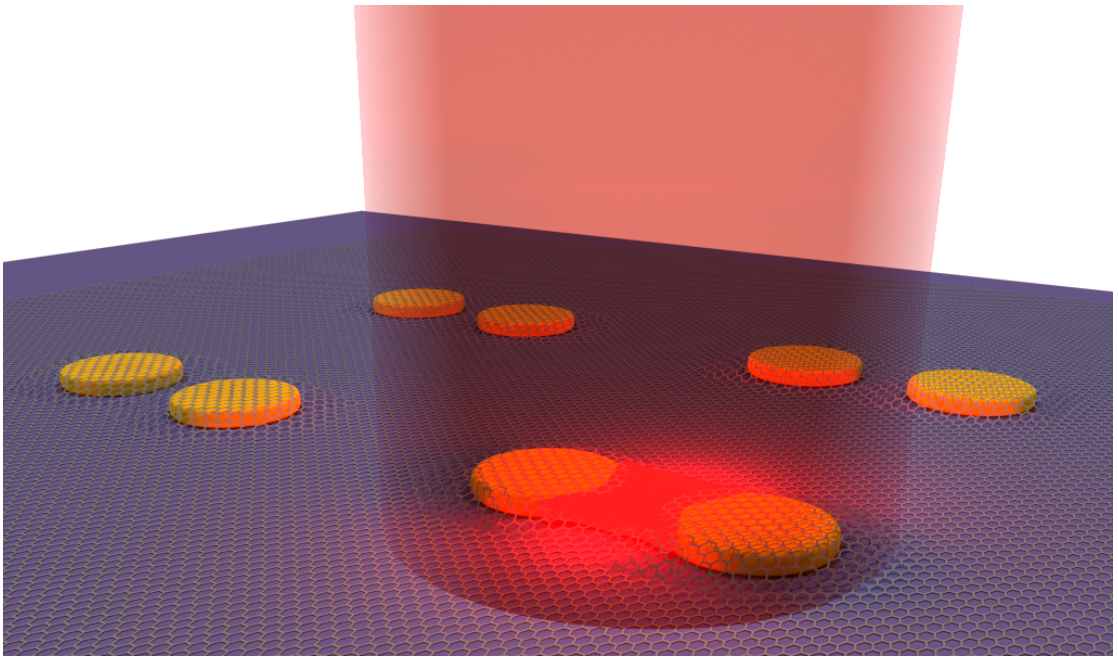

FIGURE 1.1: Schematic representation of the plasmonic system consisting of a cylindrical dimer antenna covered with graphene.

Recent developments in electron beam-lithography allowed the precise manufacturing of antennas down to sizes in the 5 nm range [20, 21]. This made it possible to create arbitrary antenna shapes and to characterize their optical properties [22, 23]. Additionally, these antennas could now be used to assess their SERS enhancement properties. However, until today there are many unanswered questions regarding SERS:

- Why do some scattering configurations show Raman modes that are forbidden by the Raman selection rules (cf. Ref.[9, 24])?
- At which excitation energy does the maximum Raman enhancement occur for a given configuration of antenna and analyte?
- Which parameters determine the total enhancement of an antenna analyte system?

In order to address these questions, the focus of this thesis is to investigate a well defined plasmonic system. Initially, our approach was to do wavelength-scanned Raman scattering using bowtie antennas manufactured by nanosphere lithography (NSL) (cf. Ref. [25]) covered with graphene. This proved to be difficult due to the high variance in the antenna dimensions and the fact that NSL produces arrays of closely spaced antennas. As a result the measured signals were an average of the contribution from many antennas. In later experiments we used dimer antennas consisting of two cylindrical antennas covered with graphene. This plasmonic system is schematically shown in Fig. 1.1. Most of the results presented in this thesis were obtained from this plasmonic system. The

system was designed to specifically probe the optical properties of free-standing plasmonic dimer antennas [26]. We used them for their polarization behavior i.e. to switch the plasmonic hotspot on and off by simply changing the polarization of the incident laser beam. In comparison to the literature a novelty of our measurements was to use only single dimer antennas instead of averaging over multiple antennas. This was done for the first time parallel to another group that published their work in October 2014 (cf. Ref. [27]). They used also dimer antennas but with another analyte and in respect to another research question.

There has only been a small amount of publications treating wavelength-scanned Raman measurements on a plasmonic system [27–29]. One reason may be that microscopic wavelength-scanned Raman measurements require a triple grating monochromator and tunable laser systems that are very expensive. The main reason however is that a triple monochromator system is much less sensitive than common notch filter Raman systems resulting in very long integration times. This leads to very demanding and time consuming measurements. Van Duyne et al. [4, 5, 29] conducted wavelength-scanned Raman measurements on a plasmonic system. They used silver NSL surfaces covered by benzenethiol with results averaged over multiple antennas. As will be shown later, NSL surfaces are inhomogeneous. Thus, one obtains a broad distribution of different resonance wavelengths. Therefore, the plasmonic resonances reported in Ref. [29] are broadened.

Our approach has some significant improvements. By using graphene we exclude any intrinsic Raman resonances from the analyte that could alter the plasmonic resonance (cf. Refs. [4, 30]). Furthermore, graphene is an inert solid. Thus, we did not expect any chemical reactions to occur that might alter the graphene in the vicinity of the antenna which is otherwise a common problem (cf. Refs. [10, 16]). Additionally, graphene is extensively characterized and has a well known band structure and phonon dispersion. It needs to be emphasized that we measured single dimer antennas having enough distance to adjacent dimer antennas to exclude interactions (cf. Fig. 1.1). Additionally, by using a dimer antenna it was possible to investigate the influence of the cavity that forms in between the cylindrical antennas forming the dimer that produces a very high field enhancement. This enhancement is higher than the enhancement created by a single antenna (cf. Refs. [17, 31]). By changing the polarization of the incoming light we were able to switch the cavity on and off which will also be shown by simulations.

Finally, our approach allows a more complete analysis of the basic processes involved in surface enhanced Raman scattering due to the following reasons:

1. We used an analyte having no intrinsic Raman resonances (cf. Sec. 3.4.4).

2. The Raman spectra of a single dimer antenna were obtained.

3. The strain induced Raman shift and mode splitting (cf. Sec. 3.4.3) was used to determine the microscopic origin of the Raman signal.

4. The excitation was done using ring lasers having a mode separation of $\Delta\lambda = 0.8\,\mathrm{nm}$. This made it possible to observe spectrally narrow features in wavelength-scanned Raman scattering.

The scattering behavior of the dimer antennas was simulated using the finite difference time domain method (FDTD). The field distribution around the dimer antenna was analyzed to assess the area where the enhanced Raman signal is being created. Additionally, the size of the single antennas and the size of the gap in between them were varied within a reasonable range. Hence, the influence of these parameters on the scattering properties was calculated and analyzed.

The overall goal of this thesis is to further elucidate the fundamental physics involved in plasmonic enhanced Raman scattering. This is necessary to improve the knowledge about the process causing the signal enhancement. This work is a first step towards a fundamental understanding. Successive work may enable the specific design of antennas capable to detect single molecules approaching a plasmonic antenna using optical spectroscopy. This may lead to incredibly sensitive gas detectors. Additionally, it may be possible to create plasmonic surfaces that control chemical reactions. This may be achieved by specific antenna designs that excite chemical reactions in a surfactant due to their high near field intensity when they are illuminated. In such a design the plasmonic antenna may act as a kind of photo-active catalyst.

This thesis is divided into two parts. The first part gives an introduction to plasmonics and the physics of metallic nanoantennas. As it is not possible to give an analytical solution of the scattering behavior of cylindrical dimer antennas it will be calculated using the FDTD method. For the calculations an open source simulation environment called Meep will be used. After testing the simulation environment for its reliability, the influence of the diameter, gap size and the substrate on dimer antennas will be presented. The second part will start by introducing the physical properties of graphene and its Raman modes with a focus on the effects of strain to the Raman spectrum of graphene. Subsequently, the theory of double resonant Raman scattering will be introduced as it describes the 2D mode of graphene, recorded in the measurements. This will be continued by the derivation of a new theory of plasmon-enhanced Raman scattering. Eventually, wavelength-scanned Raman measurements will be shown and analyzed using the new theory of plasmon-enhanced Raman scattering.

Chapter 2

Plasmonics

A brief introduction about plasmons and their properties will be given. Despite the nanoscale dimensions of plasmonic antennas, a classical approach using Maxwell's equations (MWE's) is sufficient. This may be done as the differences in energy levels are small compared to thermal excitation levels at room temperature [1].

After derivation of the most important properties of plasmons, Mie theory will be introduced. Subsequently, the finite difference time domain (FDTD) method employed to calculate the scattering properties of plasmonic antennas will be described. The calculations were done using an open source simulation environment called Meep[1].

The numerical calculations will be verified by analytical test cases before using Meep to derive the scattering behavior of cylindrical dimer antennas. This type of dimer antenna was utilized to carry out the Raman experiments presented in Chap. 3. The plasmonic properties of this antenna type will be simulated and analyzed before finishing the chapter.

[1] Meep stands for MIT electromagnetic equation propagation [32]. It is available as Open Source software under http://ab-initio.mit.edu/wiki/index.php/Meep

2.1 Fundamentals

2.1.1 Maxwell's equations and basic assumptions

Maxwell's equations completely describe the scattering behavior of arbitrary objects. In differential form they are written as (cf. Ref. [33])

$$\vec{\nabla} \cdot \vec{D} = \rho_{ext} \tag{2.1a}$$

$$\vec{\nabla} \cdot \vec{B} = 0 \tag{2.1b}$$

$$\vec{\nabla} \times \vec{E} = -\frac{\partial \vec{B}}{\partial t} \tag{2.1c}$$

$$\vec{\nabla} \times \vec{H} = \vec{J}_{ext} + \frac{\partial \vec{D}}{\partial t}. \tag{2.1d}$$

The macroscopic fields are linked to their microscopic counterparts by the polarization $\vec{P}$ and magnetization $\vec{M}$

$$\vec{D} = \epsilon_0 \vec{E} + \vec{P} \tag{2.2a}$$

$$\vec{H} = \frac{1}{\mu_0} \vec{B} - \vec{M} \tag{2.2b}$$

The rapidly varying microscopic fields are averaged over distances much larger than the underlying atomic structure as the antennas have dimensions in the tens of nanometers. This is called quasistatic approximation. Thus, we do not need to consider the microscopic fields [1] which will become more clear in Sec. 2.3.4. Furthermore, only linear, isotropic and nonmagnetic media without residual polarization $\vec{P}$ or magnetization $\vec{M}$ will be considered. Thus, we obtain

$$\vec{D} = \epsilon_0 \epsilon \vec{E} \tag{2.3a}$$

$$\vec{B} = \mu_0 \mu \vec{H} \tag{2.3b}$$

with ϵ being the relative dielectric constant and μ being the relative permittivity. Setting $\mu = 1$ for simplification is justified as we treat antennas made of nonmagnetic metals.

2.1.2 The dielectric function

The Drude model is used to describe electrical conduction in a solid [33]. It may also be extended to describe optical properties. Here, a short introduction will be given. A more elaborate derivation will be found in Ref. [33].

The equation of motion of an electron of charge e bound by a harmonic force will be used. Additionally, an external electrical field $\vec{E}(x,t)$ is applied. Thus, we find

$$\ddot{\vec{x}} + \gamma\dot{\vec{x}} + \omega_0^2\vec{x} = -e\vec{E}(\vec{x},t) \tag{2.4}$$

with γ being a damping constant. It is reasonable to assume that the excitation of the electron is small. As such it is possible to evaluate the electrical field at the mean location of the electron. Using a harmonic excitation $\vec{E}(\vec{x},t) = exp(-i\omega t)$, we are able to find a solution that constitutes the contribution from one electron to the dipole moment

$$-e\vec{x} = \vec{p} = \frac{e^2}{m}\frac{1}{\omega_0^2 - \omega^2 - i\omega\gamma}\vec{E}. \tag{2.5}$$

By multiplying $\vec{p}$ with the amount of oscillators N we describe the ensemble of oscillators as an effective medium. This approach is well justified for structure sizes $a \ll \lambda$ [34].

Now that we constructed an effective medium, it is reasonable to assume that there are $N \cdot f_i$ electrons at resonance frequency ω_i and damping constant γ_i. This may be used as a description of interband transitions in noble metals [1]. Using the relation $\epsilon/\epsilon_0 = 1 + \chi_e$ we find

$$\epsilon(\omega) = 1 + \frac{Ne^2}{\epsilon_0 m}\sum_j \frac{f_j}{\omega_j^2 - \omega^2 - i\omega\gamma_j}. \tag{2.6}$$

This equation contains the plasma frequency ω_p of the free electron gas

$$\omega_p^2 = \frac{Ne^2}{\epsilon_0 m}. \tag{2.7}$$

For high excitation frequencies we find negligible damping, approaching ω_p. At these frequencies $\epsilon(\omega)$ in Eq. (2.6) becomes predominantly real with $\epsilon(\omega) = 1 - \omega_p^2/\omega^2$ and thus the metal transparent.

Until now, an ideal free-electron metal was assumed. In a real metal, the positive ion cores cause a residual polarization, expressed by the dielectric constant ϵ_∞ for $\omega \gg \omega_p$. In this regime the optical response is dominated by free s-electrons [1]. Thus, Eq. (2.6) may be rewritten in the Lorentz-Drude (LD) form [34] commonly found in textbooks such as Refs. [1, 33, 34]

$$\epsilon(\omega) = \epsilon_\infty + \sum_j \frac{\omega_p^2 f_j}{\omega_j^2 - \omega^2 - i\omega\gamma_j}. \tag{2.8}$$

Using Eq. (2.8) we are able to describe the optical properties of a metal using only a set of individual constants $\{f_i, \omega_i, \gamma_i\}$. Later on this will be employed for the FDTD

simulations in Sec. 2.3.

2.1.3 Plasmons

Plasmons are collective oscillations of an electron plasma [1]. They are the quantized version of Langmuir waves[2]. As plasmons are a quantization of classical plasma oscillations, the macroscopic Maxwell equations (Eqns. (2.1)) are sufficient to derive the basic equations for their description.

As already mentioned, a large density of free electrons is required to sustain plasmons [34]. Thus, plasmons only occur in metals and solids having a high density of electrons such as graphene or highly doped semiconductors [36]. Having a spatially confined free-electron gas, we may assume a surface charge density $\rho_s = ne\Delta x$ with n being the electron density, e being the electron charge and Δx representing the displacement of the electron gas in x-direction. Inside the medium this induces an E-field

$$E_x = \frac{ne}{\epsilon\epsilon_0}\Delta x, \tag{2.9}$$

neglecting boundary effects in the y- and z-direction. The induced E-field acts back on the electrons and we obtain an equation of motion

$$eE_x = \frac{e^2 n}{\epsilon\epsilon_0}\Delta x = m_e \frac{\partial^2}{\partial t^2}\Delta x. \tag{2.10}$$

We find that Eq. (2.10) describes a harmonic oscillation with the bulk plasmon frequency

$$\omega_{Pl} = \sqrt{\frac{e^2 n}{m_e \epsilon\epsilon_0}} = \sqrt{\frac{\omega_p^2}{\epsilon}}. \tag{2.11}$$

So the assumption of a free-electron gas led to the description of induced electron-plasma oscillations within a solid. The quantization of this oscillation leads to quasiparticles called plasmons, obeying Bose statistics [34].

For normal electron densities, ω_{Pl} is situated in the energy range of 10 meV to 100 meV (IR) for typical semiconductors [34] and in the VIS or UV part of the spectrum for metals, due to their high electron density (cf. Eq. (2.11)) [34].

As plasmons are oscillations of free electrons, their contribution to the dielectric function is considered via the motion of free electrons. It is derived using Eq. (2.4), setting $\omega_0 = 0$ as we are now dealing with unbound carriers. The solution is obtained analogously to

[2] Langmuir waves are rapid oscillations of the electron density in conducting media such as plasmas or metals (cf. Ref. [35]).

Eq. (2.8) and we find

$$\epsilon(\omega) = \epsilon_\infty + \frac{\omega_p^2}{-\omega^2 - i\omega\gamma_e} \tag{2.12}$$

with n in ω_p now being the density of free electrons and $\gamma_e = 1/\tau_e$ being their damping constant. τ_e is the lifetime of the corresponding excitation. This result may also be found assuming an equation of motion for free carriers with an incident electric field oscillating at the frequency ω. The derivation is analogous to the one presented in Sec. 2.1.2.

Referring to the description above, the LD model considers bound and unbound charges separately [34], we find a total dielectric function according to

$$\epsilon(\omega) = \epsilon_{\text{free carrier}}(\omega) + \epsilon_{\text{bound carrier}}(\omega). \tag{2.13}$$

The bound carrier term represents Lorentz oscillations as treated in Sec. 2.1.2, Eq. (2.8). The free carrier term includes the contribution from the bulk plasmon, Eq. (2.12). As we write the total dielectric function, we need to be careful, considering ϵ_∞ only once. Eventually, we obtain

$$\epsilon(\omega) = \epsilon_\infty - \frac{\omega_p^2}{\omega^2 + i\omega\gamma_e} + \sum_j \frac{\omega_p^2 f_j}{\omega_j^2 - \omega^2 - i\omega\gamma_j}, \tag{2.14}$$

which is the general Lorentz-Drude model [34, 37] which will be used below to describe the optical properties of metals within the FDTD simulations. Equation (2.14) may also be found having the free carrier term incorporated into the sum [34].

The free carrier term in Eq. (2.14) describes the contribution of bulk plasmons to the dielectric function. This should not be mixed up with surface plasmon polaritons (SPP's) which are responsible for the resonances investigated in Sec. 2.3 and below.

2.1.4 The wave equation at a planar interface

We will now use Maxwell's equations (Eq. (2.1)) at a flat interface between a dielectric and a conductor in order to find propagating solutions at the interface. These are called surface plasmon polaritons (SPP's), in contrast to bulk plasmons which were treated in the previous section. A very detailed derivation will be found in [1].

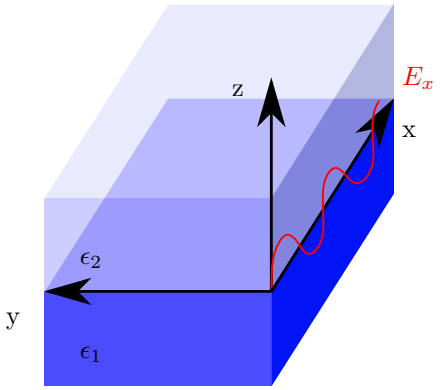

FIGURE 2.1: Interface between a metal with dielectric constant ϵ_1 and a dielectric with ϵ_2. The red wave represents a possible TM polarized wave.

Assuming there are no surface charges ($\rho_{ext} = 0$), the curl ($\vec{\nabla}\times$) equations from (2.1) may be combined with the aid of some differential identities[3]. This leads to

$$\vec{\nabla}\left(-\frac{1}{\epsilon}\vec{E}\cdot\vec{\nabla}\epsilon\right) - \nabla^2\vec{E} = -\mu_0\epsilon_0\epsilon\frac{\partial^2\vec{E}}{\partial t^2} \tag{2.15}$$

Assuming a constant dielectric profile $\epsilon(\vec{r})$ at the interface over at least one wavelength, we obtain $\epsilon(\vec{r}) = \epsilon$ and the first term of Eq. (2.15) becomes 0. Additionally, a harmonic time dependence of the electric field $\vec{E}(\vec{r},t) = \vec{E}(\vec{r})exp(-i\omega t)$ is assumed. Thus, Eq. (2.15) simplifies to the Helmholtz equation

$$\nabla^2\vec{E} - k_0^2\epsilon\vec{E} = 0 \tag{2.16}$$

with $k_0 = \omega/c$. For simplicity, let us assume that the described waves propagate along the x-direction. Thus, ϵ only varies in z-direction. Furthermore, the interface is put at $z = 0$. A solution is a propagating wave in x-direction $\vec{E}(x,y,z) = \vec{E}(z)exp(i\beta x)$ with the complex paramter $\beta = k_x$, called the propagation constant (cf. Fig. 2.1). Inserting this into Eq. (2.16) we find

$$\frac{\partial^2\vec{E}(z)}{\partial t^2} + (k_0^2\epsilon - \beta^2)\vec{E} = 0. \tag{2.17}$$

Similarly, a wave equation for the magnetic field $\vec{H}$ can be found.

Using the curl equations from (2.1), inserting a harmonic time dependence of $\partial/\partial t = -i\omega$, propagation in x-direction $\partial/\partial x = i\beta$ and assuming homogeneity in y-direction by

[3] $\vec{\nabla}\times\vec{\nabla}\vec{E} = \vec{\nabla}(\vec{\nabla}\cdot\vec{E}) - \nabla^2\vec{E}$ and $\vec{\nabla}\cdot(\epsilon\vec{E}) = \vec{E}\cdot\vec{\nabla}\alpha + \alpha\vec{\nabla}\cdot\vec{E}$ with $\alpha \in \mathbb{C}$ being a constant

$\partial/\partial y = 0$, we find the following set of equations

$$\frac{\partial E_y}{\partial z} = -i\omega\mu_0 H_x \tag{2.18a}$$

$$\frac{\partial E_x}{\partial z} - i\beta E_z = i\omega\mu_0 H_y \tag{2.18b}$$

$$i\beta E_y = i\omega\mu_0 H_z \tag{2.18c}$$

$$\frac{\partial H_y}{\partial z} = i\omega\epsilon_0\epsilon E_x \tag{2.18d}$$

$$\frac{\partial H_x}{\partial z} - i\beta H_z = -i\omega\epsilon_0\epsilon E_y \tag{2.18e}$$

$$i\beta H_y = -i\omega\epsilon_0\epsilon E_z. \tag{2.18f}$$

This system allows two sets of solutions with different polarization properties. A transverse magnetic (TM) solution with E_x, E_z and H_y being nonzero and a transverse electric (TE) one with H_x, H_z and E_y being nonzero [1].

For TM polarization the set of governing equations is

$$E_x = -i\frac{1}{\omega\epsilon_0\epsilon}\frac{\partial H_y}{\partial z} \tag{2.19a}$$

$$E_z = -\frac{\beta}{\omega\epsilon_0\epsilon}H_y \tag{2.19b}$$

$$0 = \frac{\partial^2 H_y}{\partial z^2} + (k_0^2\epsilon - \beta^2)H_y \tag{2.19c}$$

and for TE polarization we find

$$H_x = i\frac{1}{\omega\mu_0}\frac{\partial E_y}{\partial z} \tag{2.20a}$$

$$H_z = \frac{\beta}{\omega\epsilon_0}E_y \tag{2.20b}$$

$$0 = \frac{\partial^2 E_y}{\partial z^2} + (k_0^2\epsilon - \beta^2)E_y \tag{2.20c}$$

2.1.5 Surface plasmon polaritons

SPP's are electromagnetic excitations propagating at the interface between a dielectric and a conductor (cf. Fig. 2.1) [1]. They are confined to the interface plane having an evanescent field[4] reaching into the insulator and the conductor.

[4]Evanescent fields (or waves) are solutions to the wave equation at the boundary between two media with different wave motion properties ϵ and/or μ. They decay exponentially into both media but are neither absorbed nor propagate into the media (cf. Ref. [38]).

In order to have a better understanding of SPP's, their dispersion relation will be calculated. Therefore, we need propagating wave solutions at the interface between a metal ($Re(\epsilon_1) < 0$) and a dielectric ($\epsilon_2 \in \mathbb{R}$).

Using Eqns. (2.19) for TM polarization we find the following solutions for $z > 0$

$$H_y(z) = A_2 e^{i\beta x} e^{-k_2 z} \tag{2.21a}$$

$$E_x(z) = iA_2 \frac{k_2}{\omega\epsilon_0\epsilon_2} e^{i\beta x} e^{-k_2 z} \tag{2.21b}$$

$$E_z(z) = -A_1 \frac{\beta}{\omega\epsilon_0\epsilon_2} e^{i\beta x} e^{-k_2 z}. \tag{2.21c}$$

And for $z < 0$

$$H_y(z) = A_1 e^{i\beta x} e^{-k_1 z} \tag{2.22a}$$

$$E_x(z) = -iA_1 \frac{k_1}{\omega\epsilon_0\epsilon_1} e^{i\beta x} e^{-k_1 z} \tag{2.22b}$$

$$E_z(z) = -A_1 \frac{\beta}{\omega\epsilon_0\epsilon_1} e^{i\beta x} e^{-k_1 z} \tag{2.22c}$$

with k_1 and k_2 being the propagation constant in z-direction for the respective half-space. The reciprocal value $\tilde{z} = 1/|k_z|$ represents the decay length of the evanescent fields into the media.

As H_y and $\epsilon_i E_z$ need to be continuous and H_y needs to fulfill the wave equation, we find that the interface requires

$$A_1 = A_2 \tag{2.23a}$$

$$\frac{k_2}{k_1} = -\frac{\epsilon_2}{\epsilon_1} \tag{2.23b}$$

$$k_1^2 = \beta^2 - k_0^2\epsilon_1 \tag{2.23c}$$

$$k_2^2 = \beta^2 - k_0^2\epsilon_2. \tag{2.23d}$$

Combining all previous equations, the dispersion relation of SPP's propagating at the interface between a dielectric and a metal calculates to

$$\beta = k_0 \sqrt{\frac{\epsilon_1\epsilon_2}{\epsilon_1 + \epsilon_2}}. \tag{2.24}$$

Considering TE polarized surface modes, we use the same approach as above for TM polarization and find

$$A_1(k_1 + k_2) = 0 \tag{2.25}$$

with the requirement of $Re(k_1) > 0$ and $Re(k_2) > 0$ in order to get a confinement of the wave to the interface [1]. Thus Eq. (2.25) will only be fulfilled when $A_1 = 0$, which

implies $A_1 = A_2 = 0$. Therefore, no TE polarized SPP exists.

We will now have a look into the dispersion relation of an SPP. Figure 2.2 (a) shows the dispersion relation (Eq. (2.24)) of a metal having negligible damping at an interface between air (grey) and fused silica (black). For small k, the plasmon dispersion behaves like that of a photon but starts to bend over for higher values of k, until it approaches the surface plasmon frequency

$$\omega_{sp} = \frac{\omega_p}{\sqrt{1+\epsilon_2}}, \tag{2.26}$$

called $\omega_{sp,air}$ or $\omega_{sp,silica}$ in Fig. 2.2 (a). The light line $\omega = kc$ is situated to the left of the SPP dispersion relation. Thus, a SPP always has a shorter wavelength compared to free-space radiation with the out-of-plane component of the SPP wavevector being purely imaginary. This means that the SPP decays evanescently out of the plane [1]. It is not possible for a photon to excite a SPP as their respective dispersion curves do not intersect. Thus, the excitation of a SPP by direct light irradiation is not possible.

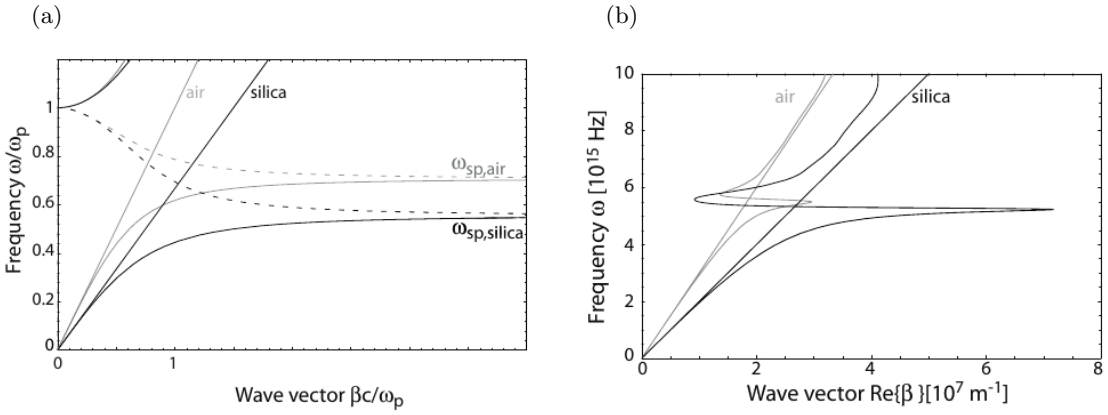

FIGURE 2.2: Dispersion relation without damping (a) and with damping (b) at a silver/air and silver/silica interface for SPP's. In (a) the frequency ω was normalized to the plasma frequency ω_p. Taken from Ref. [1].

For negligible damping we find that β converges to ∞ as ω approaches ω_{sp} and the group velocity v_g approaches 0. Thus, the SPP acquires electrostatic character [1]. This limiting case is called a surface plasmon as it does not couple to a photon.

In a real metal, interband transitions and electron damping result in $\mathrm{Im}(\epsilon_1) \neq 0$. Therefore, β becomes complex and the SPP's are damped with an energy attenuation length of $L = 1/2 \cdot \mathrm{Im}(\beta)$ [1]. This case is shown in Fig. 2.2 (b) for silver. In reality, the bound SPP's maintain a finite wave vector at ω_{sp}.

2.1.6 Excitation of surface plasmon polaritons

As described in the previous section, light is not able to couple directly to SPP's as the wave vector of an incident photon is always smaller than the wave vector needed to excite a SPP (cf. Fig. 2.2). Thus, phase matching is required for the excitation of SPP's.

When a wave is incident onto a surface, the projection to the interface is $k_x = k \sin\theta$ with θ being the angle to the surface normal. Thus, phase matching may never be achieved. However, using a medium with a higher optical density provides additional momentum to k_x as it changes the projection to $k_x = k\sqrt{\epsilon}\sin\theta$ with ϵ being the dielectric constant of the medium. This principle is shown in Fig. 2.3 using prisms as medium of higher optical density. With these setups it is possible to acquire phase matching and optically excite SPP's along a metal/dielectric interface.

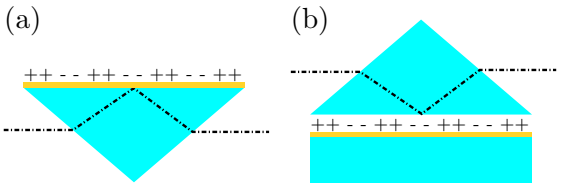

FIGURE 2.3: Prism coupling using attenuated total internal reflection using Kretschmann configuration (a) and Otto configuration (b). The plasmon is depicted by the alternating charge distribution $(++--)$.

Another way to acquire phase matching is to use the additional momentum provided by a grating. Incident radiation, incoming at an angle θ will be scattered by the grating and therefore the k_x component of the wave vector will be increased or decreased, depending on the order of diffraction. Thus, we find a wave vector $k_x = k\sin\theta \pm \nu g$ with $g = 2\pi/l$ being the reciprocal vector of the grating and $\nu \in \mathbb{N}^+$ being the diffraction order [1]. This is the reason why SPP's are observable on rough surfaces, as the surface corrugations act as grating and enable the coupling of light to SPP's. However, for a rough surface the phase matching condition changes to $k_x = k\sin\theta \pm \Delta k$ as no grating order exists [1]. Small antennas can be considered a grating. This is the reason why we observe SPP's on plasmonic antennas by direct illumination.

2.1.7 The Lorentz-Drude model

The dielectric function of gold will be modeled using Eq. (2.14) as described in Sec. 2.1.2. There are better models like the Brendel-Borman model (cf. Ref. [37]), however the LD model is widely used within many FDTD packages as it provides easy implementation

and numerical stability. As such we will use the LD model to describe the optical properties of gold in the simulations below.

i	0	1	2	3	4	5
f_j	0.760	0.024	0.010	0.071	0.601	4.384
Γ_j	0.053	0.241	0.345	0.870	2.494	2.214
ω_j	-	0.415	0.830	2.969	4.304	13.32

TABLE 2.1: The full set of parameters for the Lorentz-Drude model of gold. All values are given in eV and were extracted from Tab. 2 in Ref. [37]. The plasma frequency of gold is $\omega_p = 9.03\,\mathrm{eV}$ [37].

Reference [37] provides a full set of parameters for all noble metals. As all plasmonic antennas, used for the measurements presented later on, were manufactured from gold, its parameters are given in Tab. 2.1.

In order to obtain the correct values for the dielectric function we may use Eq. (2.14) with a slightly different notation

$$\epsilon(\omega) = \epsilon_\infty - \frac{f_0\omega_p^2}{\omega^2 + i\omega\Gamma_0} + \sum_{j=1}^{k} \frac{\omega_p^2 f_j}{\omega_j^2 - \omega^2 + i\omega\Gamma_j}. \tag{2.27}$$

Here k represents the amount of Lorentz oscillators, f_0 and Γ_0 the strength and damping of the free electron part. ϵ_∞ will be set to 1 as metals become transparent for infinite frequencies [37]. Figure 2.4 compares measured data to the LD model using the values of Tab. 2.1 and Eq. 2.27. In conclusion, the LD model fits the dielectric function of gold quite well using the data from Ref. [37].

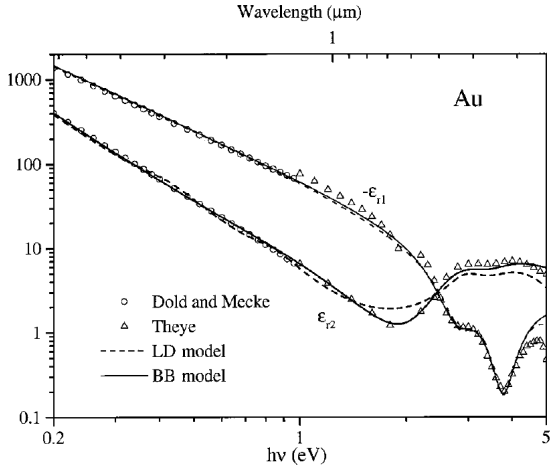

FIGURE 2.4: Comparison of experimental data to the calculated values from the Lorentz-Drude (LD) and Brendel-Borman model (BB). Taken from Ref. [37].

2.1.8 Mie scattering

Gustav Mie introduced the analytical solution of light scattering by a homogeneous sphere in 1908 [2]. His approach was to use an incident plane wave and to describe the scattered field by a sum of waves, weighting each one with a scattering coefficient. Additionally, he separated the external scattered fields from the fields inside the sphere. Below, only external fields are treated as internal fields are of no interest for the focus of this thesis. A very exhaustive description of Mie theory is given in Ref. [2]. Other descriptions will be found in Refs. [39, 40].

We will start using Maxwell's equations (2.1) without any charges present and combine them in the same way as already shown in Sec. 2.1.4. Thus, wave equations in $\vec{H}$ and $\vec{E}$ (cf. Eq. (2.16)) are obtained. They are

$$\Delta\vec{E} - k_0^2\vec{E} = 0 \tag{2.28a}$$

$$\Delta\vec{H} - k_0^2\vec{H} = 0. \tag{2.28b}$$

As we are considering a sphere it is obvious to use the spherical solutions to the Helmholtz equations above. The interested reader may find a detailed derivation in Ref. [33] and a more mathematical treatment in Ref. [41]. Here, equations will only be introduced as they are required to understand the derivation of the scattering coefficients of a sphere in vacuum. The following formulas were taken from Ref. [39] but may also be found in Ref. [2].

At the boundary between sphere and vacuum the fields need to be continuous in order to fulfill Eqns. (2.1c) and (2.1d). Thus, we obtain the following conditions

$$\left[\vec{E}_s(\vec{r}) - \vec{E}_v(\vec{r})\right]\Big|_{|\vec{r}|=\frac{d}{2}} \times \vec{n} = \vec{0} \tag{2.29a}$$

$$\left[\vec{H}_s(\vec{r}) - \vec{H}_v(\vec{r})\right]\Big|_{|\vec{r}|=\frac{d}{2}} \times \vec{n} = \vec{0}. \tag{2.29b}$$

With $\vec{n}$ being a unit vector, standing radially on the surface of the sphere. The indices s and v are referring to the sphere and vacuum, respectively. In order to write the scattering coefficients we will define the following functions, being a solution to the Helmholtz equation in spherical coordinates

$$\psi_n(x) = \sqrt{\frac{\pi x}{2}} I_{n+\frac{1}{2}}(x) \tag{2.30a}$$

$$\zeta_n(x) = \sqrt{\frac{\pi x}{2}} H_{n+\frac{1}{2}}(x) \tag{2.30b}$$

with $I_{n+\frac{1}{2}}(x)$ being the Bessel function of the first kind and $H_{n+\frac{1}{2}(x)}$ being the Hankel function of the first kind. Using these definitions we are able to write the scattering coefficients in a convenient way [39]

$$a_n = \frac{\psi_n(x)\psi_n'(mx) - m\psi_n(mx)\psi_n'(x)}{\zeta_n(x)\psi_n'(mx) - m\psi_n(mx)\zeta_n'(x)} \tag{2.31a}$$

$$b_n = \frac{m\psi_n(x)\psi_n'(mx) - \psi_n(mx)\psi_n'(x)}{m\zeta_n(x)\psi_n'(mx) - \psi_n(mx)\zeta_n'(x)}. \tag{2.31b}$$

Here, m is the complex refractive index of the sphere. In the equations it was already considered that the sphere is surrounded by vacuum ($n_{vac} = 1$). Another important parameter is the size parameter x used above. It relates the circumference of the sphere to the incident wavelength λ

$$x = \frac{\pi d}{\lambda}. \tag{2.32}$$

We are interested in the scattering properties of the sphere, depending on its size. As such we need to evaluate the following series [2]

$$Q_{ext}(x) = \frac{2}{x^2}\sum_{n=1}^{\infty}(2n+1)\Re(a_n + b_n) \tag{2.33a}$$

$$Q_{sca}(x) = \frac{2}{x^2}\sum_{n=1}^{\infty}(2n+1)(|a_n|^2 + |b_n|^2) \tag{2.33b}$$

with $\Re()$ being the real part of a complex number. Q_{ext} describes the extinction properties of the sphere and $Q_{sca} = Q_{ext} + Q_{abs}$ the scattering properties, including absorption. Therefore, we find the absolute value being considered in Eq. (2.33b) as the complex part of the scattering coefficients describes absorption.

Using Eqns. (2.33a) and (2.33b) we will calculate the scattering spectra of a sphere in vacuum. For comparison reasons the LD model (cf. Sec. 2.1.2) was used with values obtained from Rakic et al. (Ref. [37]) as the same values will be used later on for the FDTD simulations. The calculations were done using Wolfram Mathematica.

The result for a sphere having a diameter of 100 nm is shown in Fig. 2.5 (a). The scattering spectra differ in intensity, which may be understood investigating the refractive index of gold. We find $k > 1$ for the wavelength range considered (cf. Fig. 2.5 (b)), resulting in absorption of the incident wave which is the reason for $Q_{sca}(\lambda) < Q_{ext}(\lambda)$ within the wavelength range shown in Fig. 2.5 (a). Additionally, we find a shift of the maximum scattering peak to higher wavelengths. This may be understood by increased absorption of the sphere for higher wavelengths. Figure 2.5 (b) shows the real and imaginary part of the refractive index of gold. The imaginary part k increases approximately

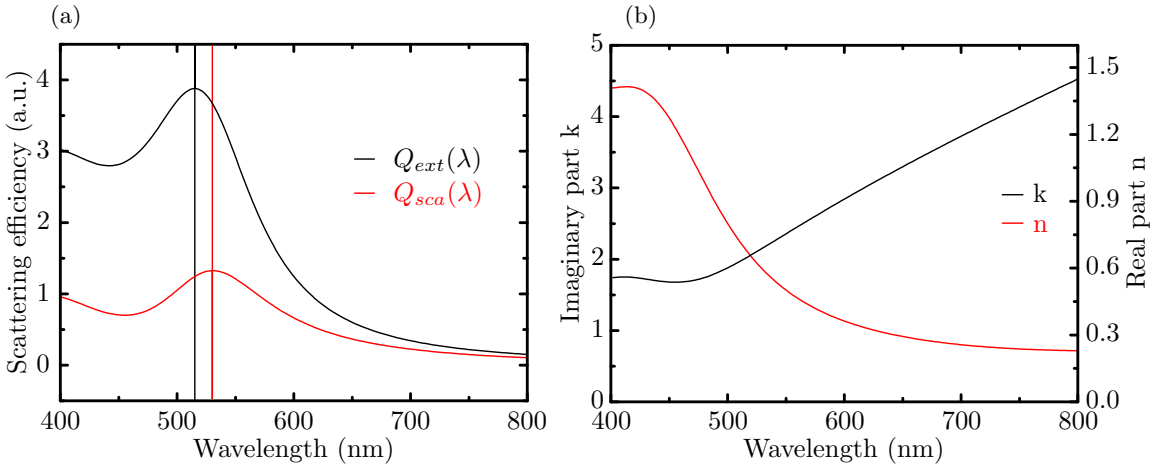

FIGURE 2.5: (a) scattering efficiency of a homogeneous golden sphere considering only the scattered field $Q_{ext}(\lambda)$ and the scattered field including absorption $Q_{sca}(\lambda)$. The diameter of the sphere was $d = 100\,\text{nm}$. (b) the complex refractive index $m = n + ik$ of gold calculated using Eq. (2.14) and the values of Tab. 2.1.

linear from 500 nm on, resulting in higher absorption by the sphere. This causes $Q_{sca}(\lambda)$ to shift to higher wavelengths.

Later on the scattering intensity of plasmonic antennas will be investigated experimentally using dark field spectroscopy which relates to $Q_{sca}(\lambda)$.

2.2 The finite difference time domain method

As there are no analytical solutions to MWE's for arbitrary shaped objects it is necessary to use a numerical approach in order to obtain the scattering properties of arbitrary plasmonic structures. Therefore, the FDTD algorithm was used and will be introduced below. The description will be quite general and not very detailed as a full treatment of the FDTD method is far beyond the scope of this work. A focus will be put on understanding the basic properties of the FDTD algorithm, including its advantages and disadvantages.

After introducing the FDTD algorithm the reliability and accuracy of the Meep FDTD code will be shown. For this purpose the FDTD calculation of a golden sphere surrounded by vacuum will be compared to the analytical solution obtained by Mie scattering.

2.2.1 Methods to solve Maxwell's equations numerically

Maxwell's equations contain continuous derivatives, being only analytically solvable for special boundary problems. In order to calculate the scattering properties and field distribution around arbitrary antennas it is necessary to use numerical methods in order to find a solution. There are different approaches, divided into two main categories[5].

Category one uses the integral form of MWE's. One often finds the direct dipole approximation (DDA), where a grid of polarizable points is used to approximate an object. The dipole moment of each point reacts to a local external field and to the field of each dipole in the grid. The resulting system of equations is commonly solved using conjugate gradient iterations[6]. Another common method is the boundary element method where MWE's are only solved at boundaries.

Category two uses the differential form of MWE's. Very widely used is the finite element method (FEM). It subdivides a problem into smaller elements and solves them according to a set of partial differential equations (PDE's), defined at each element. Thus, FEM is normally used in engineering and adaptable to complex calculations combining many PDE's, like heat conductivity and mechanical stress. FDTD uses a discretization of MWE's to solve a boundary problem by doing several time steps as will be explained later in detail. It is much easier to implement on a computer compared to FEM. Therefore, it is easier to understand the code and the numerical solution. Due to this reason FDTD was chosen to investigate the scattering properties of the antennas used for the Raman measurements. It is a very delicate procedure to write FDTD code without errors. Therefore, an open source FDTD implementation called Meep was used. It was written at the Massachusetts Institute of Technology (MIT) and was released in 2006 [44]. As it is open source software it is widely used and well tested. Especially in the field of plasmonics and photonics. Furthermore, it was adapted for parallel computation using the Open MPI[7] interface enabling parallel computing on the computer cluster of the university.

2.2.2 Discretization of Maxwell's equations

When solving a mathematical problem on a computer it is not possible to have a continuous computation. A discrete mesh, holding all values is needed. FDTD uses a simple

[5] This overview uses the Wikipedia article on computational electrodynamics (Ref. [42]) as a reference to present only methods that are currently in use. This was done as computational physics is a very fast evolving field in modern physics.

[6] The conjugate gradient method is an algorithm to solve particular systems of linear equations numerically [43].

[7] www.open-mpi.org

two-point centered difference method to evaluate the derivative of a field component ξ, for example in z-direction we get

$$\left.\frac{\partial \xi}{\partial z}\right|_{i,j,k}^{n} = \frac{\xi^{n}_{i,j,k+1/2} - \xi^{n}_{i,j,k-1/2}}{\Delta z} + O[(\Delta z)^2]. \tag{2.34}$$

The indices $\{i, j, k\} \in \mathbb{N}_+^3$ describe the index of the grid point. ξ is the field component and $n \in \mathbb{N}_+$ the time step.

The numerical grid needs to be structured. Following the suggestion initially made by Yee et al. [45], a mesh having the electric field components aligned along the grid lines and the magnetic field components centered between them is employed. This grid is shown in Fig. 2.6 with Tab. 2.2 showing the respective coordinate for each component. Please note that this alignment is a choice as it is possible to distribute the field components differently. We follow the description given in the Book written by Inan and Marshall [18] closely for the description of the FDTD algorithm.

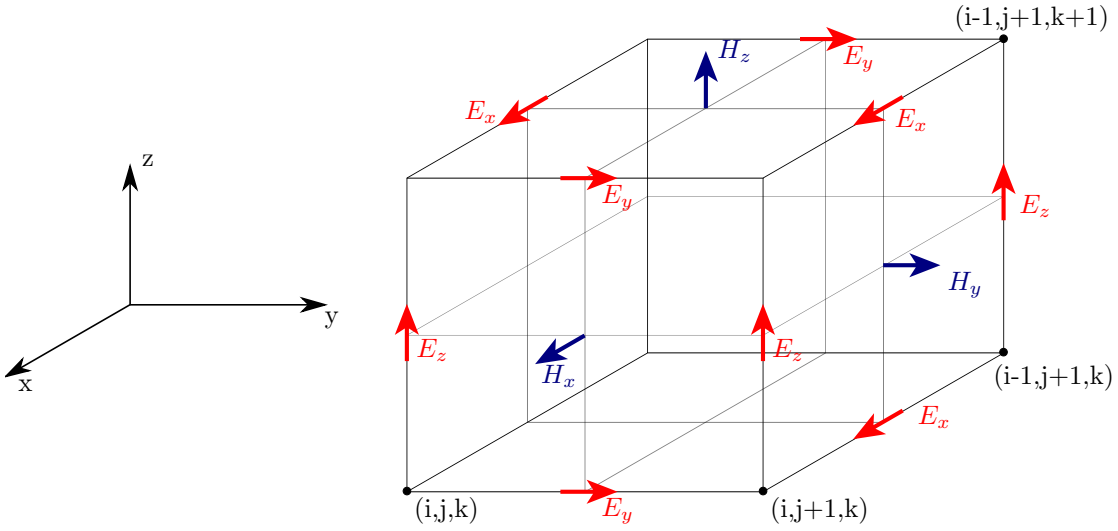

FIGURE 2.6: Position of the $\vec{E}$ and $\vec{H}$ field components within the Yee cell.

As MWE's include time derivatives we also need to express the time dependence using a two-point centered difference method. Thus, we obtain

$$\left.\frac{\partial \vec{E}}{\partial t}\right|^{n+\frac{1}{2}} = \frac{\vec{E}^{n+1} - \vec{E}^{n}}{\Delta t} = \frac{1}{\epsilon}\left[\vec{\nabla} \times \vec{H}\right]^{n+\frac{1}{2}} \tag{2.35a}$$

$$\left.\frac{\partial \vec{H}}{\partial t}\right|^{n+1} = \frac{\vec{H}^{n+\frac{3}{2}} - \vec{H}^{n+\frac{1}{2}}}{\Delta t} = -\frac{1}{\mu}\left[\vec{\nabla} \times \vec{E}\right]^{n+1}. \tag{2.35b}$$

Rearrangement gives an update procedure in time

$$\vec{E}^{n+1} = \vec{E}^{n} + \frac{\Delta t}{\epsilon}\left[\vec{\nabla}\times\vec{H}\right]^{n+\frac{1}{2}} \tag{2.36a}$$

$$\vec{H}^{n+\frac{3}{2}} = \vec{H}^{n+\frac{1}{2}} - \frac{\Delta t}{\mu}\left[\vec{\nabla}\times\vec{E}\right]^{n+1}. \tag{2.36b}$$

With Eqns. (2.34) and (2.36) we have everything we need to express MWE's using two-point centered differences in space and time. Assuming no external currents $\vec{J}_{ext} = 0$ we may now write down the time derivative of each component of $\partial\vec{E}/\partial t$ and $\partial\vec{H}/\partial t$ using the curl equations of Eqns. (2.1)

$$\begin{aligned}
\frac{\partial E_x}{\partial t} &= \frac{1}{\epsilon}\left(\frac{\partial H_z}{\partial y} - \frac{\partial H_y}{\partial z}\right) & \frac{\partial H_x}{\partial t} &= -\frac{1}{\mu}\left(\frac{\partial E_z}{\partial y} - \frac{\partial E_y}{\partial z}\right)\\
\frac{\partial E_y}{\partial t} &= \frac{1}{\epsilon}\left(\frac{\partial H_x}{\partial z} - \frac{\partial H_z}{\partial x}\right) & \frac{\partial H_y}{\partial t} &= -\frac{1}{\mu}\left(\frac{\partial E_x}{\partial z} - \frac{\partial E_z}{\partial x}\right)\\
\frac{\partial E_z}{\partial t} &= \frac{1}{\epsilon}\left(\frac{\partial H_y}{\partial x} - \frac{\partial H_x}{\partial y}\right) & \frac{\partial H_z}{\partial t} &= -\frac{1}{\mu}\left(\frac{\partial E_y}{\partial x} - \frac{\partial E_x}{\partial y}\right)
\end{aligned} \tag{2.37}$$

In order to show the basic approach on how to derive numerically friendly equations that allow the computation of electromagnetic boundary problems it is not necessary to deduce the full set of equations. Instead, the derivation will be done for the one dimensional case where the basic principle already becomes clear.

The x-direction is chosen for propagation. Therefore, we have no variations in y- and z-direction with all the respective derivatives in Eqns. (2.37) set to 0. Thus, we end up having two pairs that are completely independent of each other

$$\text{TM-mode} \qquad \frac{\partial H_y}{\partial t} = \frac{1}{\mu}\frac{\partial E_z}{\partial x} \qquad \frac{\partial E_z}{\partial t} = \frac{1}{\epsilon}\frac{\partial H_y}{\partial x} \tag{2.38a}$$

$$\text{TE-mode} \qquad \frac{\partial E_y}{\partial t} = -\frac{1}{\epsilon}\frac{\partial H_z}{\partial x} \qquad \frac{\partial H_z}{\partial t} = -\frac{1}{\mu}\frac{\partial E_y}{\partial x} \tag{2.38b}$$

As Eqns. (2.38a) only contain the E_z and H_y field components they are called transverse magnetic (TM) modes. Accordingly, Eqns. (2.38b) are called transverse electric (TE) as they contain only the E_y and H_z components. This should not be confused with the common notation of TE and TM waves in electromagnetic theory. Here, it is just a way of naming both independent sets of equations.

We will combine and apply centered differences in space (Eq. (2.34)) and time (Eqns. (2.35)). According to the Yee cell in Fig. 2.6 we place the components of $\vec{E}$ at full-integer points and the components of $\vec{H}$ at half-integer points in space and time. Thus,

Field component	x location	y location	z location
E_x	$i+\frac{1}{2}$	j	k
E_y	i	$j+\frac{1}{2}$	k
E_z	i	j	$k+\frac{1}{2}$
H_x	i	$j+\frac{1}{2}$	$k+\frac{1}{2}$
H_y	$i+\frac{1}{2}$	j	$k+\frac{1}{2}$
H_z	$i+\frac{1}{2}$	$j+\frac{1}{2}$	k

TABLE 2.2: Locations of the field components of the Yee cell depicted in Fig. 2.6.

we find the update equations for the TE-mode

$$E_y\Big|_i^{n+1} = E_y\Big|_i^{n} - \frac{\Delta t}{\epsilon_i \Delta x}\left[H_z\Big|_{i+\frac{1}{2}}^{n+\frac{1}{2}} - H_z\Big|_{i-\frac{1}{2}}^{n+\frac{1}{2}}\right] \tag{2.39a}$$

$$H_z\Big|_{i+\frac{1}{2}}^{n+\frac{1}{2}} = H_z\Big|_{i+\frac{1}{2}}^{n-\frac{1}{2}} - \frac{\Delta t}{\mu_{i+\frac{1}{2}} \Delta x}\left[E_y\Big|_{i+1}^{n} - E_y\Big|_{i}^{n}\right] \tag{2.39b}$$

and for the TM-mode

$$E_z\Big|_i^{n+1} = E_z\Big|_i^{n} + \frac{\Delta t}{\epsilon_i \Delta x}\left[H_y\Big|_{i+\frac{1}{2}}^{n+\frac{1}{2}} - H_y\Big|_{i-\frac{1}{2}}^{n+\frac{1}{2}}\right] \tag{2.40a}$$

$$H_y\Big|_{i+\frac{1}{2}}^{n+\frac{1}{2}} = H_y\Big|_{i+\frac{1}{2}}^{n-\frac{1}{2}} + \frac{\Delta t}{\mu_{i+\frac{1}{2}} \Delta x}\left[E_z\Big|_{i+1}^{n} - E_z\Big|_{i}^{n}\right]. \tag{2.40b}$$

Within these equations we find the material properties ϵ_i and $\mu_{i+1/2}$ which we may use to describe media within the numerical grid. However, they need to be isotropic i.e. they do not vary with direction.

Using the same approach we are able to derive the discretized form of MWE's (Eq. (2.37)) by applying centered differences in three dimensions. Therefore, we need to know the location of the field components as they will be found in Fig. 2.6. Their coordinates are listed in Tab. 2.2. The full set of equations is quite lengthy[8]. They are not given here as we will not get any new insight from writing them down.

As a short reminder, we are still assuming no losses or external currents and an isotropic medium. To incorporate these, external currents may be discretized directly. Losses are incorporated using centered differences as shown for the derivatives in MWE's. As we do not require external currents or losses within our medium the derivation of these discretizations is omitted. The interested reader will find them in Ref. [18].

[8] The interested reader will find them on page 85 in Ref. [18].

2.2.3 Stability criterion

We have already seen that the update equations (cf. Eqns. (2.39) & (2.40)) contain the fraction $\Delta t/\Delta x$. Varying this ratio, we find that only for $\Delta t \leq \Delta x$, the solution of a simulation is stable as time progresses [18]. This condition is called the Courant-Friedrich-Lewy (CFL) condition (cf. Ref. [46]). Reference [18] does a von Neumann stability analysis (cf. Ref. [47]) on the FDTD algorithm and derives

$$\Delta t \leq \frac{\Delta x}{\sqrt{D} v_p} \tag{2.41}$$

with D being the dimension (1,2 or 3) and v_p being the highest phase velocity of a wave inside of the numerical cell. This may be reformulated to

$$\frac{\Delta t}{\Delta x} = S \leq \frac{n}{\sqrt{D} c} \tag{2.42}$$

with S being called the Courant factor or CFL number and n being the smallest index of refraction within a simulation (usually 1).

2.2.4 Sources

A simulation may be driven from one or more points within the numerical cell. One way to directly apply a source is to include it into the desired points. This is done by adding the fields to the respective point source. E.g. we may use the E_y-field component (Eq. (2.39a))

$$E_y\Big|_i^{n+1} = E_y\Big|_i^{n} - \frac{\Delta t}{\epsilon_i \Delta x}\left[H_z\Big|_{i+\frac{1}{2}}^{n+\frac{1}{2}} - H_z\Big|_{i-\frac{1}{2}}^{n+\frac{1}{2}}\right] + E_{y,\text{source}}\Big|_i^{n+1}. \tag{2.43}$$

With $E_{y,\text{source}}|_i^{n+1}$ being the source field at time $n+1$ applied to the grid point i. Consequently, $E_{y,\text{source}}|_i^{n+1}$ will only be nonzero at grid points where the source is situated.

A sinusoidal source for single frequency excitation may be applied by setting

$$E_{y,\text{source}}\Big|_i^{n} = E_0 \sin(2\pi f_0 n \Delta t) \tag{2.44}$$

with E_0 being the field amplitude and f_0 being the frequency of the source. For broadband excitation we may apply a Gaussian source by setting

$$E_{y,\text{source}}\Big|_i^{n} = E_0 \sin(2\pi f_0 (n - n_s)\Delta t) e^{-\frac{(n\Delta t - n_s \Delta t)^2}{(n_{1/2}\Delta t)^2}} \tag{2.45}$$

with n_s being the time delay of the source and $n_{1/2}\Delta t$ being the full width at half maximum time of the pulse. In order to ensure numerical stability the first derivative

in time of Eq. (2.45) is being used in Meep [48]. This does only negligible changes to the results of a simulation but ensures a smooth transition of the fields when turning the source on and off [44]. Doing so, numerical instabilities due to high field gradients will not occur at the source boundary and increase the overall numerical stability for a simulation.

Another way of implementing sources is to use currents [18]. These are typically required when an object like an antenna excites the fields. A current excites a field through the curl equation in (2.35a)

$$\left.\frac{\partial \vec{E}}{\partial t}\right|^{n+\frac{1}{2}} = \frac{1}{\epsilon}\left[\vec{\nabla}\times\vec{H}\right]^{n+\frac{1}{2}} - \left.\frac{1}{\epsilon}\vec{J}_{\text{source}}\right|^{n+\frac{1}{2}} \tag{2.46}$$

with the source being located at the same grid location as the E-field. However, having the same point in time as the H-field.

2.2.5 Absorbing boundary conditions

Every numerical cell has a finite cell size. Thus, propagating fields will at some point hit the cell boundary. At this point the update equations (Eqns. (2.36)) are missing a value for the field component lying outside of the numerical cell. We may set the missing component to zero and thus create a perfect electrical conductor. However, this will cause the fields to be reflected at the boundary, which is not the desired behavior as we want to simulate an "infinite" space. Therefore, it is necessary to create a boundary at the numerical cell which absorbs all incident fields.

There have been several approaches to create an absorbing boundary [18, 19]. The main difficulty was to create a small layer that absorbs all frequencies, independent on the angle of incidence of a wave. Many absorbing boundary conditions (ABC's) have been developed but had the problem of bad absorption for high angles of incidence. The interested reader may find some approaches like the Mur boundary in Ref. [18]. An overview of different ABC's may be found in Ref. [19].

In 1994 Bérenger (cf. Ref. [49]) addressed the problem, described above, by splitting the fields in MWE's and selectively choosing different values for the conductivities in different directions. Splitting means he divided each component of the vector fields into two orthogonal components[9]. Thus, he obtained a set of 12 coupled partial differential equations. By choosing conductivities, consistent with a dispersionless medium he created a planar interface without reflection.

[9] These components do not have a physical interpretation. They are purely mathematical.

The basic principle will be shown by investigating a TE mode in two dimensions (xy-plane). Using Maxwell's equations including magnetic currents and dividing E_z according to $E_z = E_{zx} + E_{zy}$ results in the following set of differential equations

$$\mu_2 \frac{\partial H_x}{\partial t} + \sigma_{m,y} H_x = -\frac{\partial E_z}{\partial y} \tag{2.47a}$$

$$\mu_2 \frac{\partial H_y}{\partial t} + \sigma_{m,x} H_y = \frac{\partial E_z}{\partial x} \tag{2.47b}$$

$$\epsilon_2 \frac{\partial E_{zx}}{\partial t} + \sigma_x E_{zx} = \frac{\partial H_y}{\partial x} \tag{2.47c}$$

$$\epsilon_2 \frac{\partial E_{zy}}{\partial t} + \sigma_y E_{zy} = -\frac{\partial H_x}{\partial y}. \tag{2.47d}$$

The index 2 refers to the absorbing medium. Now that σ_m and E_z were divided into two parts it is possible to selectively attenuate the waves in the respective direction. In the equations above we obtain attenuation in x-direction for $\sigma_{m,x} \neq 0$ and $\sigma_x \neq 0$ and in y-direction when setting $\sigma_{m,y} \neq 0$ and $\sigma_y \neq 0$. In order to obtain the wave equation we may write Eqns. (2.47) conveniently in time-harmonic form

$$i\omega\mu_2 \underbrace{\left(1 + \frac{\sigma_{m,y}}{i\omega\mu_2}\right)}_{s_{m,y}} H_x = -\frac{\partial}{\partial y}(E_{zx} + E_{zy}) \tag{2.48a}$$

$$i\omega\mu_2 \underbrace{\left(1 + \frac{\sigma_{m,x}}{i\omega\mu_2}\right)}_{s_{m,x}} H_y = \frac{\partial}{\partial x}(E_{zx} + E_{zy}) \tag{2.48b}$$

$$i\omega\epsilon_2 \underbrace{\left(1 + \frac{\sigma_x}{i\omega\epsilon_2}\right)}_{s_x} E_{zx} = \frac{\partial}{\partial x} H_y \tag{2.48c}$$

$$i\omega\epsilon_2 \underbrace{\left(1 + \frac{\sigma_y}{i\omega\epsilon_2}\right)}_{s_y} E_{zy} = -\frac{\partial}{\partial y} H_x. \tag{2.48d}$$

After differentiation of the first two equations in x and y and insertion of the last two equations we find

$$0 = \frac{1}{s_y s_{m,y}} \frac{\partial^2}{\partial y^2}(E_{zx} + E_{zy}) + \omega^2 \epsilon_2 \mu_2 E_{zy} \tag{2.49a}$$

$$0 = \frac{1}{s_x s_{m,x}} \frac{\partial^2}{\partial x^2}(E_{zx} + E_{zy}) + \omega^2 \epsilon_2 \mu_2 E_{zx} \tag{2.49b}$$

Now let us assume there is no E_{zx} component. By subsequently adding the equations above we find

$$\omega^2 \epsilon_2 \mu_2 E_{zy} + \frac{1}{s_x s_{m,x}} \frac{\partial^2 E_{zy}}{\partial x^2} + \frac{1}{s_y s_{m,y}} \frac{\partial^2 E_{zy}}{\partial y^2} = 0 \tag{2.50}$$

which is a wave equation with the solution

$$E_{zy} = TE_0 e^{-i\sqrt{s_x s_{m,x}}k_{2x}x - i\sqrt{s_y s_{m,y}}k_{2y}y}. \tag{2.51}$$

With T being the amount of the field transmitted into the absorbing medium. The wave vectors need to follow the condition

$$k_{2x}^2 + k_{2y}^2 = \omega^2 \epsilon_2 \mu_2. \tag{2.52}$$

Using Eqns. (2.48a) and (2.48b) we find the corresponding solutions for H_x and H_y

$$H_x = TE_0 \frac{k_{2y}}{\omega\mu_2}\sqrt{\frac{s_y}{s_{m,y}}} e^{-i\sqrt{s_x s_{m,x}}k_{2x}x - i\sqrt{s_y s_{m,y}}k_{2y}y} \tag{2.53a}$$

$$H_y = -TE_0 \frac{k_{2x}}{\omega\mu_2}\sqrt{\frac{s_x}{s_{m,x}}} e^{-i\sqrt{s_x s_{m,x}}k_{2x}x - i\sqrt{s_y s_{m,y}}k_{2y}y}. \tag{2.53b}$$

Now that we have the solutions for all wave components we are able to derive the reflection coefficient R by applying continuity of the tangential electric and magnetic fields across the interface between region 1 (simulation space) and region 2 (absorber). We obtain

$$R = \frac{\frac{k_{1x}}{\omega\epsilon_1} - \frac{k_{2x}}{\omega\epsilon_2}\sqrt{\frac{s_{m,x}}{s_x}}}{\frac{k_{1x}}{\omega\epsilon_1} + \frac{k_{2x}}{\omega\epsilon_2}\sqrt{\frac{s_{m,x}}{s_x}}}. \tag{2.54}$$

As we want zero reflection ($R = 0$) it is a good choice to assume $\epsilon_1 = \epsilon_2$, $\mu_1 = \mu_2$ and $s_{m,x} = s_x$. Thus, we find $k_{1x} = k_{2x}$ and also obtain $k_{1y} = k_{2y}$ from Eq. (2.52). This results in $R = 0$ for all angles of incidence.

Now we may derive the fields passing the boundary between region 1 and 2 by using Eqns. (2.51) and (2.53), inserting the assumptions and the relation $k_{1x} = \omega\sqrt{\epsilon_2\mu_2}\cos\theta$ with θ being the angle of incidence of the incoming wave.

$$\begin{aligned} E_{zy} &= E_0 e^{-s_x k_{1x}x - ik_{1y}y} \\ &= E_0 e^{-k_{1x}x - ik_{1y}y} e^{-\sigma_x \eta x\cos\theta} \end{aligned} \tag{2.55a}$$

$$H_x = E_0\eta^{-1}\sin\theta e^{-k_{1x}x - ik_{1y}y} e^{-\sigma_x\eta x\cos\theta} \tag{2.55b}$$

$$H_y = -E_0\eta^{-1}\cos\theta e^{-k_{1x}x - ik_{1y}y} e^{-\sigma_x\eta x\cos\theta} \tag{2.55c}$$

with $\eta = \sqrt{\mu_2/\epsilon_2}$. In Eqns. (2.55) we find the wave in region 2 propagating in the same direction as in region 1 (from $e^{-k_{1x}x - ik_{1y}y}$). But more importantly the transmitted wave decays exponentially ($e^{-\sigma_x\eta x\cos\theta}$). We also find that the attenuation is independent of the frequency. This makes the Bérenger perfectly matched layer (PML) a very good ABC with no reflection as long as there is enough space to fully attenuate the wave in

the PML region. However, due to numerical discretization some frequency-dependent reflections may be observed within the simulation.

2.2.6 Reflection and transmission spectra

The most frequent task done using an FDTD simulation is to compute the frequency response of a structure to an excitation of interest. Using a spectrally broad source (normally a Gaussian source) a structure is probed for all frequencies present at once.

The first question that needs to be answered is which quantity needs to be evaluated. Generally, one is interested in the transmitted or reflected power which is expressed by the Pointing vector, giving us the direction of the energy flowing through an area of interest

$$P(\omega) = \Re\ \vec{n} \cdot \int \vec{E}(x,\omega)^* \cdot \vec{H}(x,\omega) d^2x \tag{2.56}$$

with $\vec{n}$ being the normalized vector in the direction of the energy flux and d^2x being the area investigated.
As time-dependent field values $\vec{E}(x,t)$ are obtained from an FDTD simulation, Fourier transformation of the fields $\mathfrak{F}(x,t) = \{\vec{E}, \vec{H}\}$ is required

$$\widetilde{\mathfrak{F}}(x,\omega) = \frac{1}{\sqrt{2\pi}} \int \mathfrak{F}(x,t) e^{i\omega t} dt \approx \frac{1}{\sqrt{2\pi}} \sum_n \mathfrak{F}(x, n\Delta t) e^{i\omega n \Delta t} \tag{2.57}$$

in order to calculate the frequency-dependent energy spectrum.

The computation of the transmission and reflection spectra is a bit more tricky than just computing $P(\omega)$ at the respective area. This is a consequence of $P(\omega)$ containing the spectrum of the source, the spectrum of the scatterer and eventually also the spectrum of adjacent structures. In order to separate the contribution of the source and adjacent structures the simulation needs to be calculated twice. Once without and once with the scatterer and subsequent subtraction of the fields. However, as interference may occur it would be a mistake to subtract the power calculated using Eq. (2.56) with and without the structure. It is necessary to subtract the fields before adding them up by evaluating

$$P_s(\omega) = \Re\ \vec{n} \cdot \int \left(\vec{E}(x,\omega) - \vec{E}_0(x,\omega)\right)^* \cdot \left(\vec{H}(x,\omega) - \vec{H}_0(x,\omega)\right) d^2x \tag{2.58}$$

with $\vec{E}_0$ and $\vec{H}_0$ being the Fourier transformed fields from the simulation without the structure. This approach prevents interferences that would occur when using only $P(\omega)$.

Initially, this is obvious only for the reflectance as we find the field coming from the source and the fields being reflected by the structure. However, in transmission we also find that there are different contributions to the energy flux. For example, when

investigating an antenna situated on a substrate with a SiO_2 layer, reflections within that layer are observed. Additionally, there are often reflections coming from the boundary of the numerical cell. This is the case as the absorbing boundary layer is not perfect (cf. Sec. 2.2.5). Therefore, it is also necessary to use Eq. (2.58) also for the transmission spectrum.

In order to correct for the excitation spectrum, the scattered spectrum $P_s(\omega)$ has to be corrected by the unscattered one $P(\omega)$ using

$$[R, T] = \frac{P_s(\omega)}{P(\omega)} \tag{2.59}$$

2.2.7 Materials

To model a material in FDTD the approach already presented in Sec. 2.1.2 will be used. The basic idea is to model a material response via

$$\vec{D} = \epsilon_\infty \vec{E} + \vec{P} \tag{2.60}$$

and use $\epsilon_\infty \vec{E}$ for an instantaneous response as it was already modeled in the update equations and $\vec{P}$ to modify the fields for the frequency-dependent polarization response of the material. Therefore, Eq. (2.4) is being used and rewritten to account for every resonance j and the time dependence of the incident fields $\partial E/\partial t$ at the spatial point $\vec{x}$

$$\frac{\partial^2 \vec{x}}{\partial t^2} + \gamma_j \frac{\partial \vec{x}}{\partial t} + \omega_{0j}^2 \vec{x} = \epsilon_0 \omega_p^2 f_j \frac{\partial E}{\partial t}. \tag{2.61}$$

This equation may be discretized and rearranged in order to be incorporated into Eq. (2.35a) via its $\partial E/\partial t$ term. The details may be found in chapter 10.2.3 of Ref. [18]. They will not be presented here as the full derivation is quite long and does not give new insight into the FDTD algorithm or its properties.

An important outcome of the discretization of Eq. (2.61) is that the final update equation requires E^{n-1} and E^n. Meaning an additional storage requirement to model dispersive media. Additionally, it has to be considered that a high frequency Lorentzian resonance ω_j may require time stepping to be increased as the condition $(\omega_j/2\pi)\Delta t > 2$ needs to be fulfilled [50].

2.3 Meep

Before calculating the scattering spectra of dimer antennas, it is necessary to verify that Meep is a reliable FDTD code, capable of calculating the scattering properties of plasmonic antennas. This will be done by comparing simulations done using Meep to analytical solutions.

Subsequently, the scattering spectra and field distributions of gold dimer antennas will be shown and the dependence on antenna size and influence of the gap will be calculated. The section will close with a brief introduction of the scattering spectra of gold bowtie antennas.

Before investigating the test cases we need to make some general considerations about Meep and its properties.

As MWE's are scale invariant, it is not required to use real field strengths to obtain correct results. As already described in Sec. 2.2.6, the quotient of the fields with and without the antenna present will be evaluated. Thus, units do not matter as they cancel out. Concerning the field distribution, the relation of the fields with and without antenna are of interest, also canceling out the unit.

However, we need to choose a characteristic length scale a[10]. A reasonable value $a = 100\,\text{nm}$ was chosen as it is convenient since the antenna dimension and wavelength are in the 100 nm scale. Due to MWE's being scale invariant, Meep was written setting $\{\epsilon_0, \mu_0, c\} = 1$ [44]. Thus, we find that a is also the time unit (as $c = \lambda f$). The frequency ω is defined as usual by $\omega = 2\pi c/a = 2\pi f$.

As Meep does not provide adaptive meshing[11] we need to deal with a static mesh, i.e. Meep provides a rectangular mesh of uniform size. Therefore, every object that we create will be approximated by cubes (in 3D) or rectangles (in 2D). Thus we will never encounter round corners (cf. Fig. 2.7). Every object will be fitted to the simulation grid, resulting in sharp corners. This has some fundamental consequences

- Round objects will show a different curvature, depending on the size of the mesh.
- Field hotspots may be encountered at edges when the curvature becomes too high due to discretization.
- A certain minimum mesh size is required to sufficiently let discretized objects look like their continuous counterparts. This is especially important when investigating problems where the results depend on the curvature of an object.

[10] The length scale is not to be confused with the resolution of the simulation.
[11] e.g. supporting a variable spatial distance between grid points

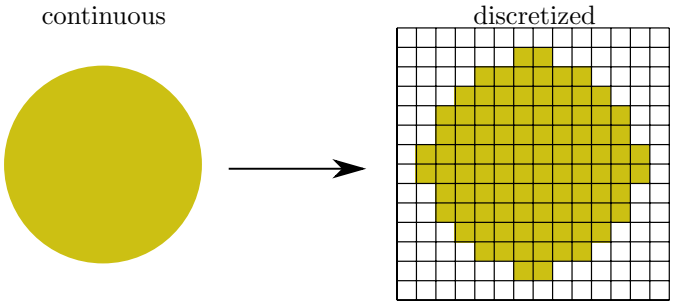

FIGURE 2.7: Demonstration of spatial discretization as it occurs when simulating a round object like a circle.

Meep uses a clever way of discretizing objects according to their dielectric function $\epsilon(\vec{r}, \omega)$ [51]. However, it is required to check if the resolution is sufficient every time before running a simulation.

Meep supports dispersive materials via the LD model [50]. Thus, gold will be defined using the LD model described in Sec. 2.1.2. However, we need to recalculate the parameters of Tab. 2.1, adapting them to Meep units with $a = 100\,\text{nm}$.

The LD implementation within Meep also considers electric conductivity σ_D by an alternative formulation of Eq. (2.14) [50]

$$\epsilon_{\omega,\vec{x}} = \left(1 + \frac{i\sigma_D(\vec{x})}{\omega}\right)\left[\epsilon_\infty(\vec{x}) + \sum_n \frac{\sigma_n(\vec{x})\omega_n^2}{\omega_n^2 - \omega^2 - i\omega\gamma_n}\right]. \tag{2.62}$$

Comparing this equation to Eq. (2.14), we immediately find $\sigma_D(\vec{x}) = 0$. Additionally, the free carrier part was incorporated into the sum for convenience. Comparing the coefficients we find $\sigma_n = f_n\omega_p^2/\omega_n$. It is obvious that Eq. (2.62) expects units of angular frequency. Thus, the energy values of Tab. 2.1 will be multiplied by the factor $\mathfrak{n} = \omega/\hbar = 2\pi c/a\hbar$. The adapted values of various metals may be found in the source code used for the simulations presented below.

2.3.1 Testing the simulation environment

Before doing calculations on antennas it is necessary to test the simulation on its reliability. Therefore, two test scenarios were employed. The first test calculates the reflection spectrum of a gold plane in two dimensions. Thus, the LD gold model in Meep will be verified and the LD parameters will be checked for their correctness. After verifying the gold model, the second test case is the scattering spectrum of a gold sphere. It will be compared to the analytical solution obtained using Mie scattering (cf. Sec. 2.1.8). As the LD model of gold was used with the same parameters, any differences between simulation and analytical solution may originate from the simulation.

2.3.1.1 Reflection spectrum of gold

The values found in Ref. [37] were implemented into Meep as described in Sec. 2.3. The reflection of a gold plane under normal incidence was calculated analytically using Wolfram Research Mathematica.

The analytical solution of the reflection coefficient was obtained using Fresnel's equations at an angle of incidence of $\theta = \pi/2$. Using the formula

$$R(\omega) = \frac{(n_0 - n_1(\omega))^2 + k_1(\omega)^2}{(n_0 + n_1(\omega))^2 + k_1(\omega)^2} \tag{2.63}$$

with $n_0 = 1$. The complex refractive index $n_1(\omega) + ik_1(\omega)$ for gold was calculated using the LD-model with the parameters tabulated in Tab. 2.1.

Figure 2.8 (a) shows the numerical cell used for simulating the reflectance of a gold plane under normal incidence. A Gaussian source is situated 400 nm above the gold surface and a fluxplane is situated 4.5 µm above the gold surface. The numerical cell is terminated by a PML.

Figure 2.8 (b) compares the obtained spectra. They are very similar with the Meep solution being slightly higher. This may be attributed to the finite size of the numerical cell and the discretization of the LD model as described in Sec. 2.2.7. Additionally, the simulation was done in 2D. Thus, we find the fields of the source e.g. not to impinge perpendicular on the surface (i.e. $\theta \neq \pi/2$). Numerical inaccuracies could occur for Lorentz oscillators having a small linewidth as it is the case for the $\omega_j = 2.969\,\text{eV}$ oscillator. These deviations are avoidable by adjusting the Courant factor (cf. Sec. 2.2.3) at the cost of a massive increase in computation time. The error is strongly dependent of the resolution of the simulation but will be kept below 5% within the simulations presented here as all simulations were checked for convergence and the resolution was chosen as high as possible.

Additionally, Fig. 2.8 (b) shows that the FDTD simulation systematically overestimates reflectance. The reason is the Fourier transformation of a finite amount of field points. This causes oscillations at high and low frequencies and has influence on the intensity of the spectrum. The oscillations are avoided by decreasing the frequency width of both the source and the fluxregions such that any oscillation occurs outside of the spectral region shown. This was already considered in Fig. 2.8 (b). Increasing the amount of points in the fluxplane and the simulation time would lead to convergence of the simulation to the analytical solution in case such oscillations are observed. In conclusion, Meep is able to model gold via the LD model and calculate the reflection properties of a Gold block in good agreement with the analytical solution. Any deviations originate

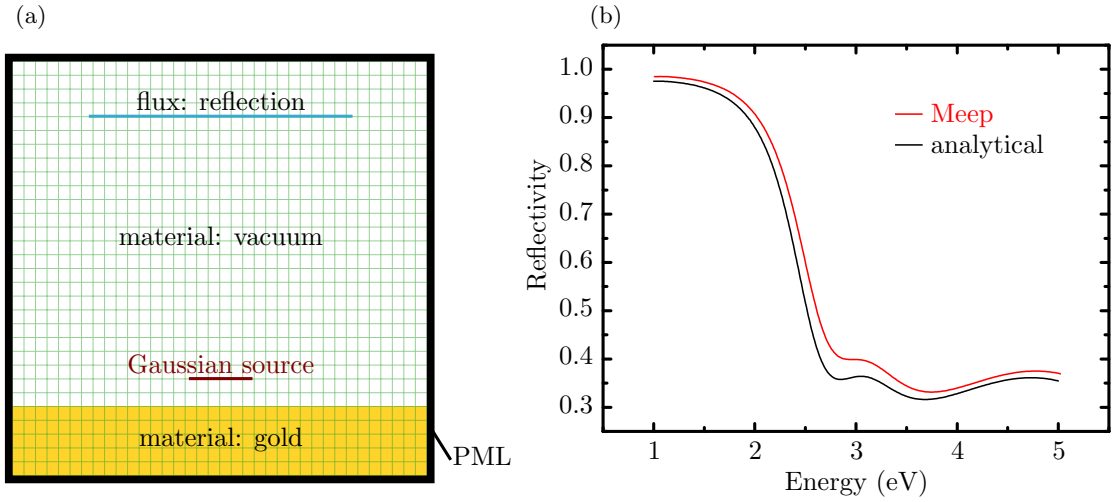

FIGURE 2.8: (a) 2D numerical cell used to calculate the Reflection of a vacuum/gold interface with the green mesh indicating the numerical grid. (b) comparison of analytical and simulated spectrum of the reflectance at a vacuum gold interface under normal incidence.

from the finite size of the computational cell and the limited amount of CPU time and memory available. To be sure, a commercial software, FDTD solutions from Lumerical solutions[12] was used to independently verify the simulations. This software was only available on one computer and could not be used on the university cluster to calculate the more sophisticated simulations on dimer antennas. However, the results of both simulation packages were in very good agreement for the test cases presented here.

2.3.1.2 Scattering spectrum of a gold sphere in vacuum

The scattering spectrum of a gold sphere in vacuum was calculated using Meep and compared to the analytical solution obtained by Mie scattering (cf. Sec. 2.1.8). As the LD model also considers absorption, Q_{sca} (Eq. (2.33b)) was used as an analytical reference.

The scattering properties of a gold sphere were calculated in three dimensions, showing the stability of the simulation later on. This was also done as all consecutive simulations were calculated in three dimensions. In general, a calculation in 2D is also possible as the problem has spherical symmetry. Because Q_{sca} describes the scattered radiation in all directions, a fluxregion was created that forms a cube around the sphere. This is seen in Fig. 2.9 (a) via the light blue region. The entire cell is surrounded by a PML layer indicated by the gray planes. In general, only the upper and lower planes are shown for clarity. This scheme will also be used later on. The fluxplanes were 400 nm

[12] www.lumerical.com

away from the sphere in order to let the fields propagate before performing a Fourier transformation of the fields. This way, interferences with the sphere and the source were avoided. Additionally, it is required to verify if the near field or far field is investigated. From antenna theory it is known that the distance of transition between near and far field is given by $d_f = 2D^2/\lambda$ [18, 33], where D is the largest dimension of the antenna. Thus, we find $d_f \approx 33\,\text{nm}$ for a 100 nm sphere and 600 nm irradiation. Therefore, the fluxplanes were placed 450 nm away from the center of the sphere, ensuring the calculation of far field spectra for spheres of up to 300 nm. The source was placed 470 nm away from the sphere, just outside of the fluxregions. As all spectra are corrected by a blank run (without the sphere) as described in Sec. 2.2.6, the position of the source does not matter as long as it is not touching a PML region or is too close to the scatterer. Doing so would alter the spectrum of the fields and lead to incorrect results.

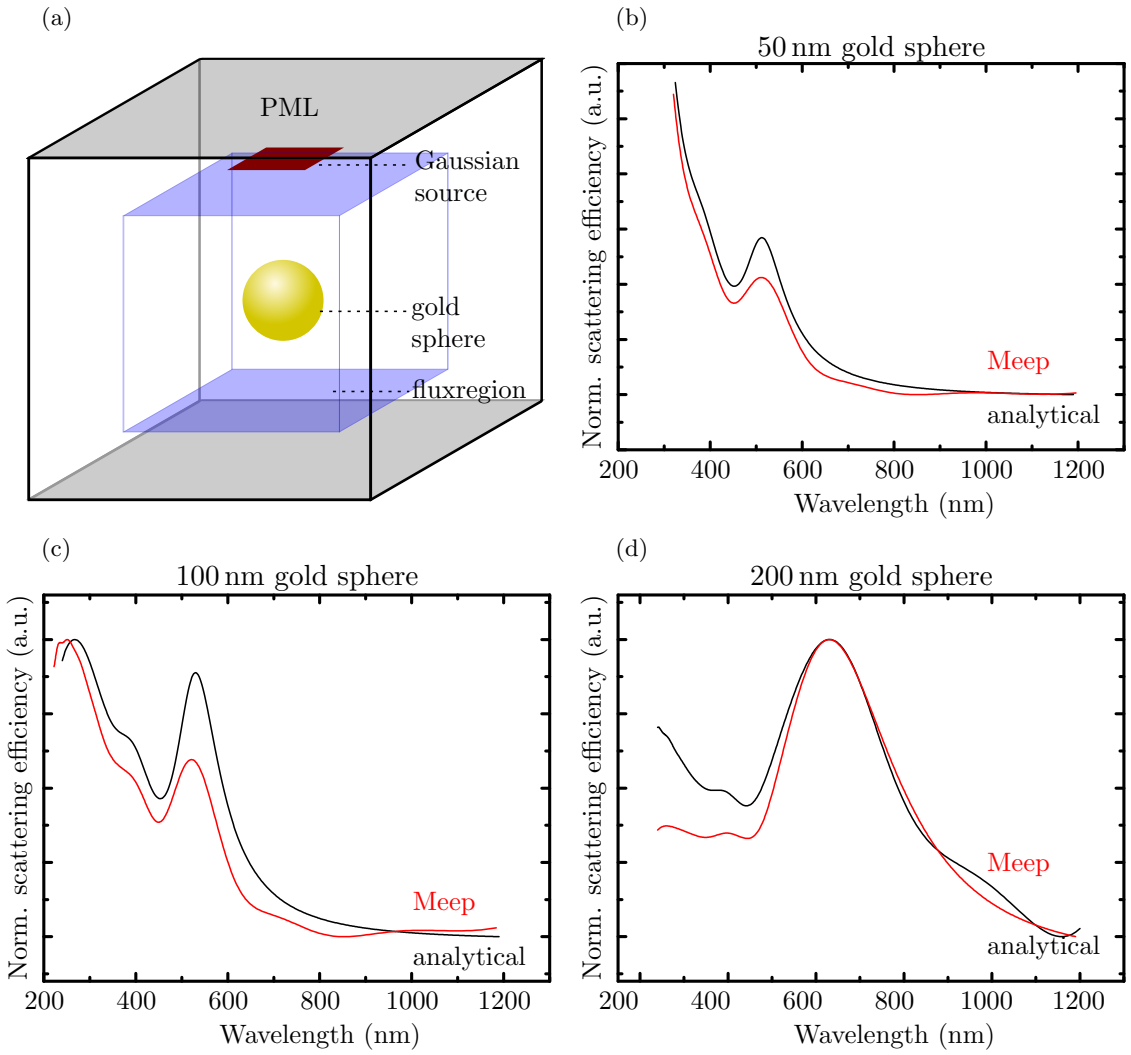

FIGURE 2.9: Scattering spectra of a golden sphere surrounded by vacuum. (a) 3D numerical cell. Comparisons of the scattering spectra obtained by Meep and the analytical solution for spheres with a diameter of (b) 50 nm, (c) 100 nm and (d) 200 nm.

In Figs. 2.9 (b) through 2.9 (d) we find that FDTD is very well able to reproduce the scattering behavior of a sphere. The main resonance was reproduced correctly for each diameter. However, we also find features originating from the FDTD simulation. In Figs. 2.9 (c) and 2.9 (d) we find quadrupole resonances at 390 nm and 400 nm, respectively. As the size of the sphere is being increased we find that the dominant dipole moment is redshifted and broadened. Additionally, higher-order dipole moments start contributing. The general increase in scattering efficiency towards the UV is a result of high oscillator strength in the dielectric function of gold in the UV region.

In conclusion, Meep is able to reproduce the scattering behavior of nanoparticles sufficiently. Deviations may arise due to the discretization of the sphere which may be circumvented by increasing the mesh resolution.

2.3.2 Scattering spectra of gold dimer antennas

Now, we calculate the plasmonic properties of gold dimer antennas. These antennas were used for Raman measurements that will be presented in Chapter 5. Therefore, it is important to understand their plasmonic properties. There are two main parameters determining the plasmonic resonance, the diameter of the cylindrical antennas and the size of the gap in between them. The diameter was varied within a range of 50 nm to 200 nm and the gap within a range of 10 nm to 150 nm. Throughout the remainder of this chapter we will only investigate single dimer antennas consisting of two single cylindrical or triangular antennas. We will sometimes refer to a dimer antenna having a certain diameter referring to the diameter of the two cylindrical antennas forming the dimer antenna.

2.3.2.1 Far field scattering behavior

Figure 2.10 shows the simulation setup used to calculate the reflected far field. The goal is to develop an understanding of the plasmonic behavior of the dimer antennas used. Thus, no substrate is included as a SiO_2 layer alters the resonance. The influence of a SiO_2 layer will be treated later in this chapter in Sec. 2.3.3. The dimer antenna is situated in the center of the numerical cell, having at least 500 nm of free space in every direction. Thus, an interaction between the near field of the dimer antenna and the PML is excluded. The fluxregion is placed 310 nm above the dimer antenna to let the fields propagate. This way, the far field spectrum is collected which is also seen in dark field spectroscopy (cf. Sec. 5.1). 210 nm above the fluxregion, a Gaussian source is placed. This is far enough to ensure a smooth calculation of the fields within the fluxplane. The entire simulation space is surrounded by a PML layer, absorbing all incident fields.

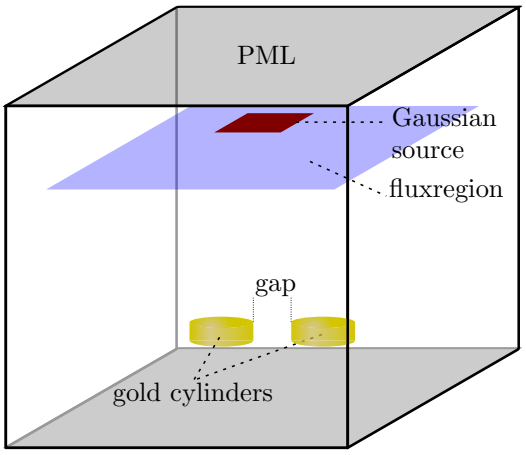

FIGURE 2.10: 3D numerical cell used to calculate the scattering spectrum of a dimer antenna in the center of the numerical grid.

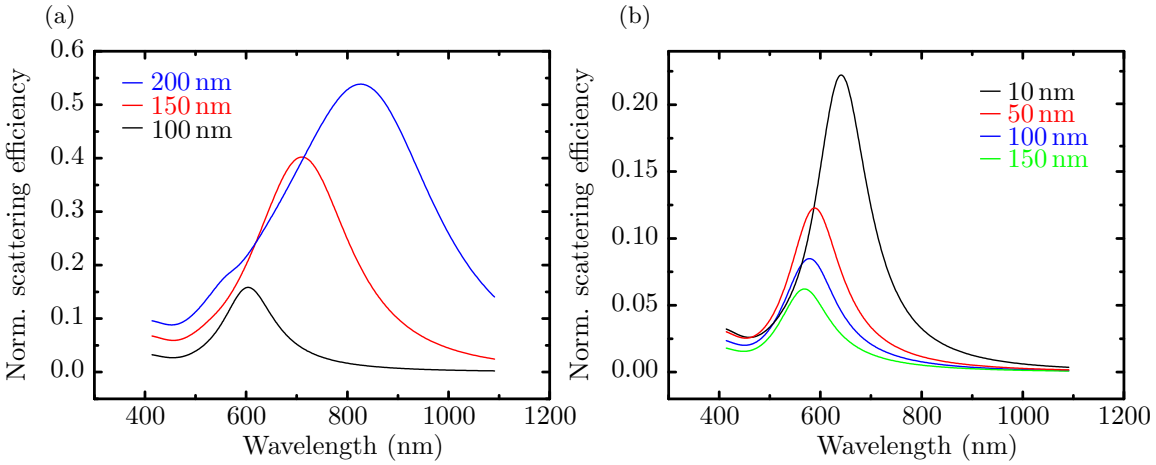

FIGURE 2.11: Far field scattering spectra for dimer antennas with a constant gap size of 30 nm and different diameters (a) and with a constant diameter of 100 nm and different gap sizes (b).

Figure 2.11 (a) shows the influence of the diameter on the reflection spectrum of the dimer antenna. We find a strong redshift of the resonance wavelength as described in Refs. [25, 52–55]. Additionally, the dipole mode broadens for increasing diameters of the dimer antenna. This is a well known behavior [1, 25, 55] that is caused by increased damping of the plasmon by intraband and interband transitions [56] due to the higher area of the two cylindrical antennas. Below 2.3 eV (540 nm) radiative damping becomes dominant for antennas made of gold [56]. This is observable in the increase of the scattering efficiency in Fig. 2.11 for wavelengths below 500 nm. For the 200 nm dimer antenna we find an additional mode around 550 nm which is the quadrupole mode. This mode is being excited for dimer antennas with a diameter above 200 nm.

Figure 2.11 (b) shows the influence of the size of the gap in between the cylindrical antennas. We find a redshift for decreasing gap size. This effect was described in Refs.

[31, 57]. For decreasing gap size, the evanescent fields of the cylindrical antennas start to couple and we find a coupled plasmon mode to cause the redshift. This happens as the effective propagation length of the surface plasmon becomes longer and damping increases. As Ref. [31] explains, this effect is important until the gap size approaches twice the diameter of the cylindrical antennas[13]. Additionally, we find broadening, originating from increased damping as described above.

Figure 2.12 shows a detailed analysis of the far field scattering behavior of a gold dimer antenna. Figs. 2.12 (a), 2.12 (c) and 2.12 (e) show 2D plots of the dipole amplitude, position and width, respectively. All values were obtained by fitting simulated spectra to a single Lorentzian model. As the quadrupole mode is being excited for dimer antennas with a diameter above 200 nm, the analysis was restricted to diameters up to 200 nm. The gap size was varied from 10 nm to 150 nm as this is the plasmonic coupling region of the cylindrical antennas where the highest amplification is expected.

In Fig. 2.12 (a) we find that the scattering amplitude of the dipole mode is increased for decreasing gap size and increasing antenna size. It is obvious that bigger antennas have an increased reflectance due to their larger scattering area. However, smaller gaps also increase the reflectance due to plasmon coupling. This causes an exponential decay of the scattering amplitude as the evanescent waves from each dimer show an exponential amplitude decay over the distance to the dimer [38]. This causes the exponential distance dependence shown in Fig. 2.12 (b).

Plasmon coupling is also the reason for the exponential change in position of the dipole mode (cf. Fig. 2.12 (d)). As the coupling between the cylindrical antennas becomes stronger, the dipole mode starts to redshift as already described for the scattering amplitude.

The width of the dipole mode follows also an exponential decay (cf. Fig. 2.12 (f)) for constant diameters and decreasing gap size. This is caused by broadening of the dipole mode when the cylindrical antennas start to couple. Figure 2.12 (e) indicates that a minimum width of the dipole mode is reached for antennas smaller than 100 nm in diameter. This is due to minimal damping of the plasmon. However, the mode starts to broaden up again for diameters below 75 nm due to increased radiation damping below 75 nm [52, 56]. This is recognizable at the bottom of Fig. 2.12 (e).

The reader may have observed oscillations in the contour lines of Figs. 2.15 (a), 2.15 (c) & 2.15 (e). They are caused by approximating the antennas within a discrete mesh as described in Sec. 2.3. This leads to an error in the diameter and gap size and subsequently to the oscillations observed.

[13] In Fig. 2.11 (b) this happens for a gap size larger than 200 nm as the cylindrical antennas have a diameter of 100 nm.

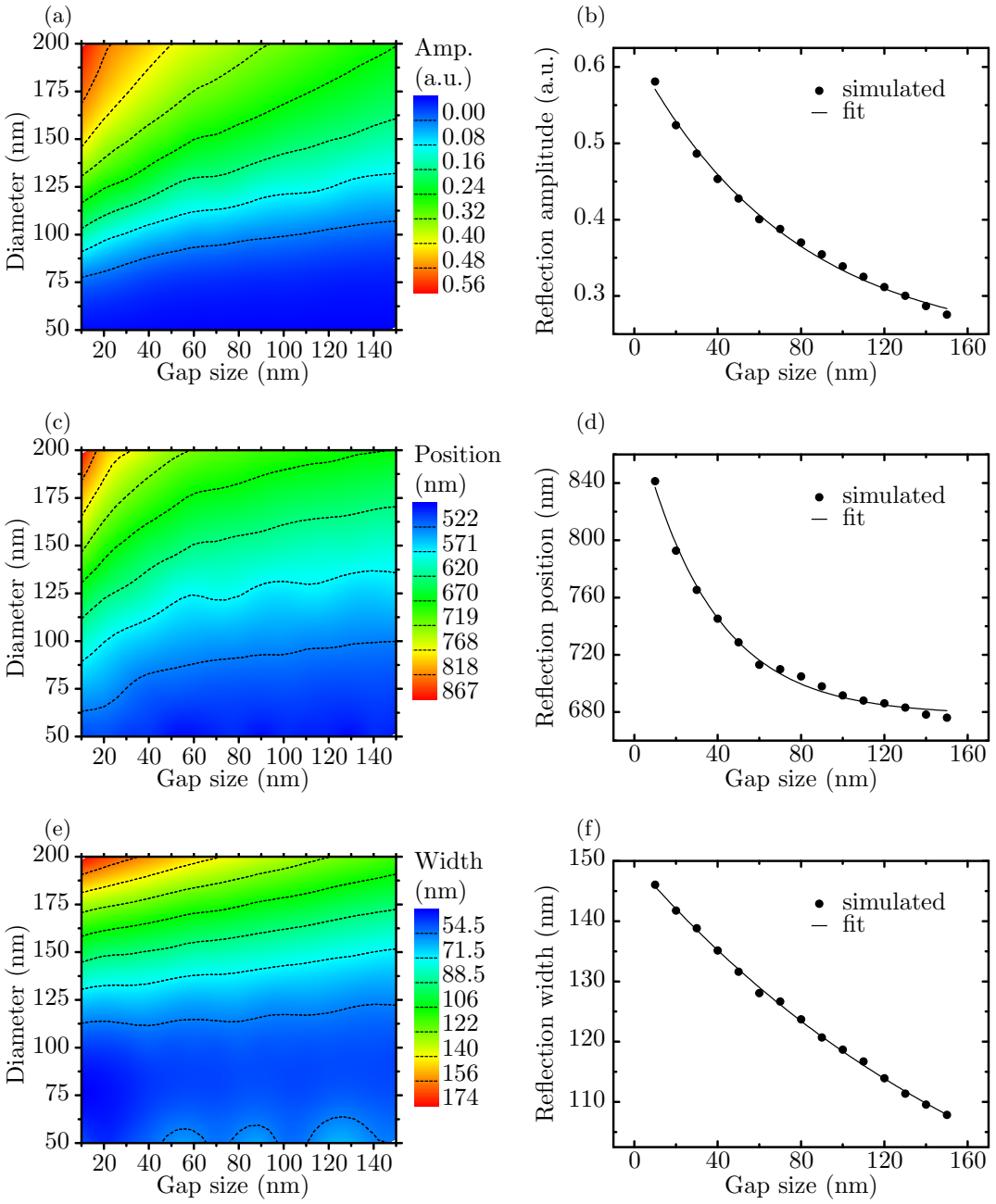

FIGURE 2.12: Far field scattering of dimer antennas. The 2D plots show the amplitude (a), position (b) and width (c) of the dipole mode. Plots (b), (c) and (d) show line cuts at a constant diameter of 175 nm from the 2D plot next to them. The line cuts were fitted using an exponential fitting function. The obtained values are given in Tab. 2.3.

2.3.2.2 Near field scattering behavior

In order to obtain a proper SERS enhancement, an analyte needs to be very close to the dimer antenna, still within the near field region [10]. Thus, the Raman signal is being excited by the near field of the dimer antenna. It is necessary to find correlations between the far field that is accessible by dark field spectroscopy and the near field which is only accessible using elaborate techniques, such as scanning near field optical microscopy (SNOM).

To numerically measure the near field spectrum, a fluxplane is placed inside the gap between the cylindrical antennas (cf. Fig. 2.13). It is kept at minimum two grid cells away from each cylindrical antenna to prevent numerical interference effects. The spectra only show a small dependence on the distance to each cylindrical antenna which is mainly caused by the field transformation from near to far field. These effects are negligible as the gap size is very small. Therefore, only one fluxregion was used throughout the calculations. Figure 2.13 shows the computational cell used.

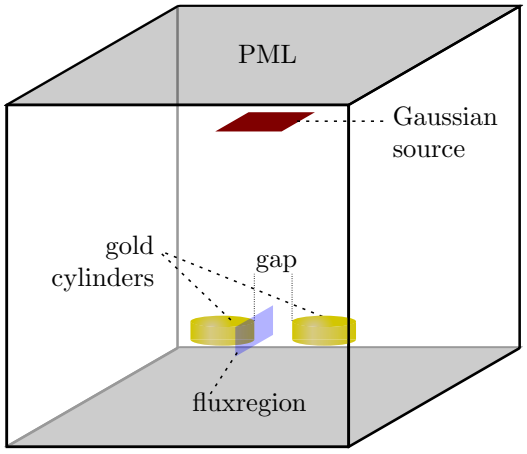

FIGURE 2.13: 3D numerical cell used to calculate the near field spectrum of a dimer antenna in the center of the numerical grid. The cell is terminated by a PML, shown only at the top and bottom plane.

In Fig. 2.14 (a) the influence of the diameter on the near field spectrum is shown. Again, we find that the peak of the dipole mode shifts to higher wavelengths as the size of the dimer antenna increases. Since the spectra are normalized to the total intensity of the source we find that light is focused in between the cylindrical antennas, explaining values higher than one in the normalized scattering efficiency. Additionally, we find that the amplitude of the near field scattering cross section reaches a maximum for a diameter of 150 nm and then starts to decrease again. This happens due to higher radiation damping. Additionally, the field strength is enhanced due to the high curvature of the cylindrical antennas [33]. When the diameter increases, the curvature effect decreases and the area of the cylindrical antennas increases. Therefore, the plasmon experiences more and more

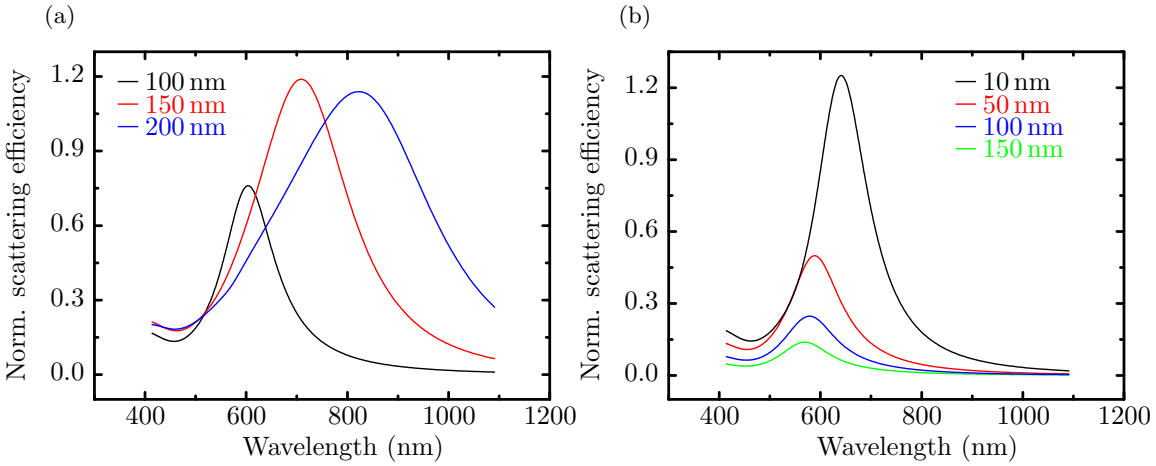

FIGURE 2.14: Near field scattering spectra for dimer antennas of constant gap size of 30 nm and different diameters (a) and of constant diameter of 100 nm and different gap sizes (b).

damping from interband transitions. Additionally, this causes broadening of the dipole mode which is well observable in Fig. 2.14 (a) (cf. Sec. 2.3.2.1). The quadrupole mode is not observable in the near field spectra since its field does not touch the fluxregion (cf. Fig. 2.20 (b)).

Figure 2.14 (b) shows the dependence of the spectra on the gap size. Again, we find that the dipole mode shifts to the blue for increasing gap size and is slightly broadened (cf. Sec. 2.3.2.1). However, the increase in amplitude is much higher by a factor of nine for the near field (cf. Fig. 2.14 (b)) compared to four in the far field (cf. Fig. 2.11 (b)), between the 10 nm and 150 nm gaps. This is expected as the dimer antenna channels the incoming radiation into the cavity formed inside of the gap.

It has to be emphasized that the normalized scattering efficiency, shown here does not relate to the field enhancement. It is a measure of how much power penetrates the fluxregion compared to the case when no antenna is present. Thus, the fluxspectrum is a good measure for the spectral distribution but the magnitude depends strongly on the area of the fluxregion. Nevertheless, the intensity scales approximately with the amplitude of the fields inside the cavity. Therefore, a rising amplitude implies a higher amplification. Absolute values will be discussed later in Sec. 2.3.4.

The line cuts for a constant diameter of 175 nm are shown in Figs. 2.12 and 2.15. The data was fitted using an exponential decay function

$$y = A \cdot \exp\left(-\frac{x}{t}\right) + y_0. \tag{2.64}$$

The obtained fitting values are shown in Tab. 2.3. Comparing the near and far field values we find that A of the amplitude increases by four times in the near field and the

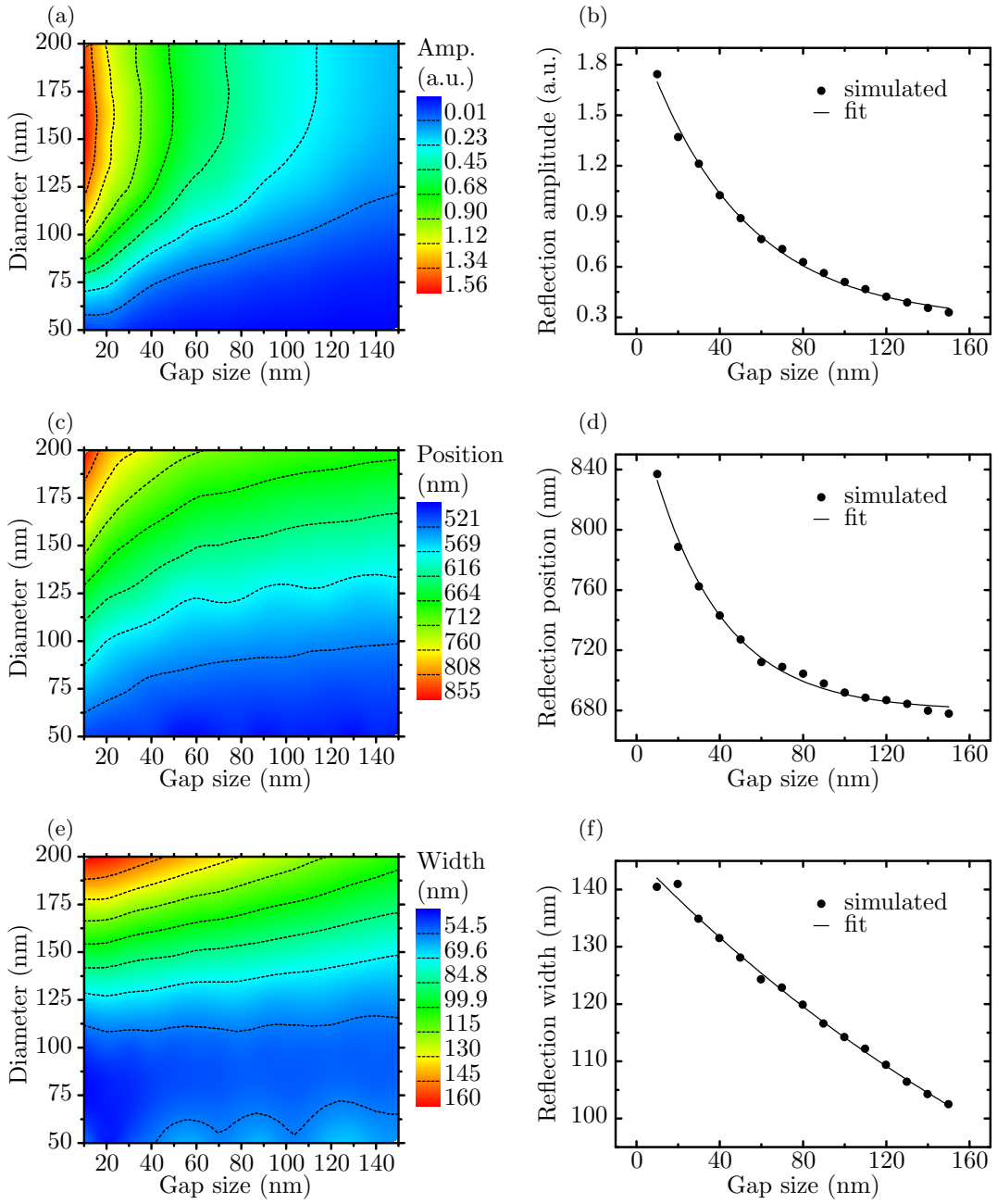

FIGURE 2.15: Near field scattering of dimer antennas. The 2D plots show the amplitude (a), position (b) and width (c) of the dipole mode. Plots (b), (c) and (d) show line cuts at a constant diameter of 175 nm from the 2D plot next to them. The line cuts were fitted using an exponential fitting function. The obtained values are given in Tab. 2.3.

	far field		
	A	t	y_0
Amplitude	0.39 ± 0.01	76 ± 6 nm	0.23 ± 0.01
Position	211 ± 5 nm	35 ± 2 nm	678 ± 2 nm
Width	77 ± 5 nm	190 ± 20 nm	72 ± 5 nm
	near field		
	A	t	y_0
Amplitude	1.75 ± 0.03	48 ± 3 nm	0.28 ± 0.02
Position	205 ± 5 nm	34 ± 2 nm	680 ± 2 nm
Width	100 ± 20 nm	270 ± 80 nm	40 ± 20 nm

TABLE 2.3: Comparison of the fitting values obtained in Figs. 2.12 & 2.15 plots (b), (d) and (f) using a single exponential decay function.

decay length t is about 30 nm shorter. The faster decay is attributed to the coupled plasmon mode in the gap. The fitting value A of the width of the dipole mode increases by 23 nm in the near field due to broadening caused by the coupled plasmon mode. The decay length t of the width is 80 nm higher compared to the far field also due to the coupled plasmon. The position of the dipole mode shows only a small difference in A of 6 nm and 1 nm in the decay length t.

To show more general differences between the near and far field scattering behavior, the corresponding contour plots were subtracted and are shown in Figs. 2.16. Thus, we also consider different diameters of the cylindrical antennas. The contour plots were obtained by subtracting the far field values from the near field values for amplitude, position and width using the data shown in Figs. 2.12 and 2.15. We find that for small gap sizes (below 50 nm) the field enhancement, loosely represented by the amplitude increases (cf. Fig. 2.16 (a)). This is caused as the coupling of the cylindrical antennas increases and therefore the coupled plasmon mode becomes more pronounced. The dipole mode is blue shifted in the near field. This is shown in Fig. 2.16 (b) where it is observable that the gap size has a stronger influence on the shift than the diameter. The same is observable in Fig. 2.16 (c) for the width of the dipole mode. In both images we find small features that are caused by the finite mesh size that alters the dimensions of the cylindrical antennas and the gap size when Meep discretizes them. This effect is more pronounced for small gap sizes and diameters as already stated in Sec. 2.3. The highest amplification is found at a gap size of 10 nm with a diameter of the cylindrical antennas of 150 nm. This configuration shows a resonance around 780 nm.

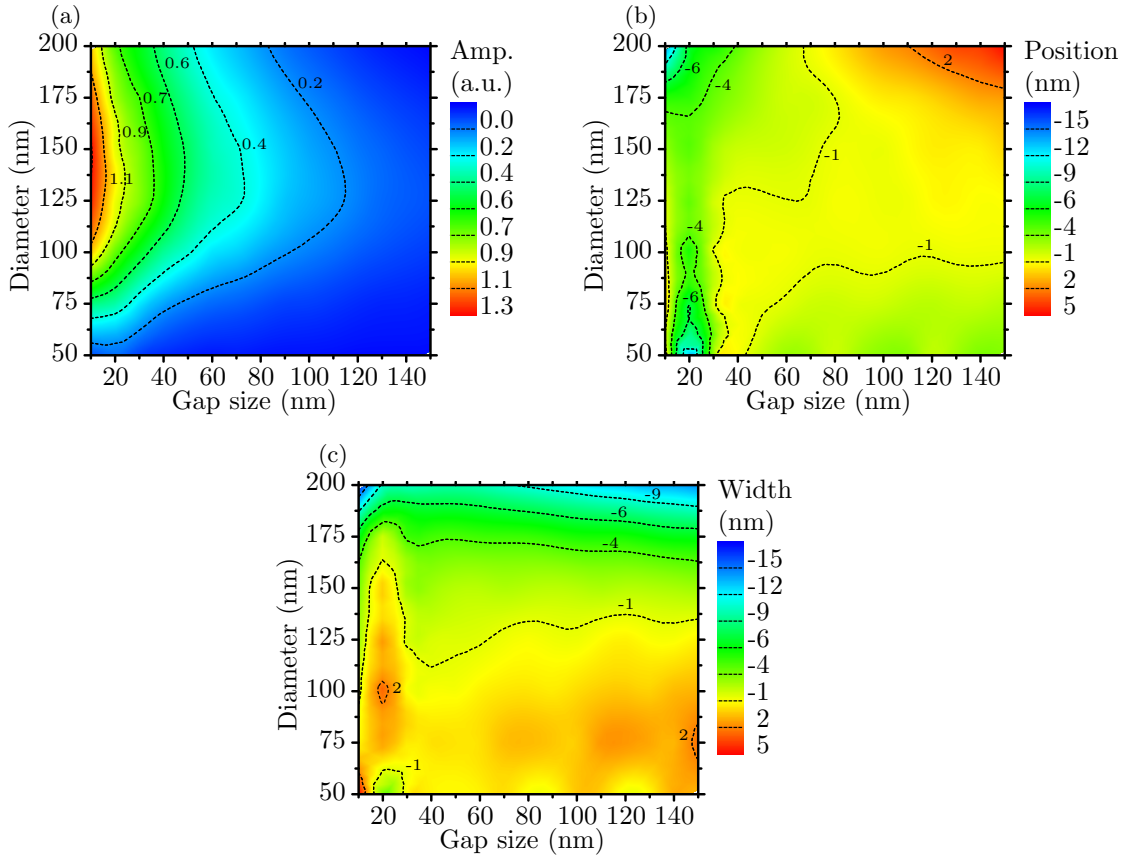

FIGURE 2.16: 2D contour plots showing the difference between near and far field scattering cross sections. All data was obtained by subtracting the near field values by the far field values for (a) amplitude, (b) position and (c) width of the respective 2D contour plots shown in Figs. 2.15 & 2.12.

2.3.3 Influence of a substrate

When the dimer antenna is placed on a SiO_2 substrate (n=1.46 [58]), the dipole mode shifts to the IR region. This happens for the near and far field. However, the near field experiences a stronger shift. The difference in the near field is shown in a 2D plot in Fig. 2.17 (b). The computational cell is shown in Fig. 2.17 (a). It is the same as in Fig. 2.13 but with SiO_2 underneath the dimer antenna. As the spectral features follow the same trends, no dedicated 2D plots are shown. The most prominent feature is the position of the dipole mode. Figure 2.17 (b) shows the difference of the dipole mode position in the near field for the simulation including a SiO_2 substrate and without any substrate. We find a minimal shift of 41 nm for a dimer antenna with a diameter of 75 nm and a gap size of 100 nm. The spectra are shown in Fig. 2.17 (c). We find a maximum shift of 132 nm for dimer antennas having a diameter of 175 nm and a gap size of 150 nm. The corresponding spectra are shown in Fig. 2.17 (d). The maximum is the result of different shift rates of the dipole mode for dimer antennas with and without a substrate underneath. We find the substrate to always redshift the dipole mode in the near field.

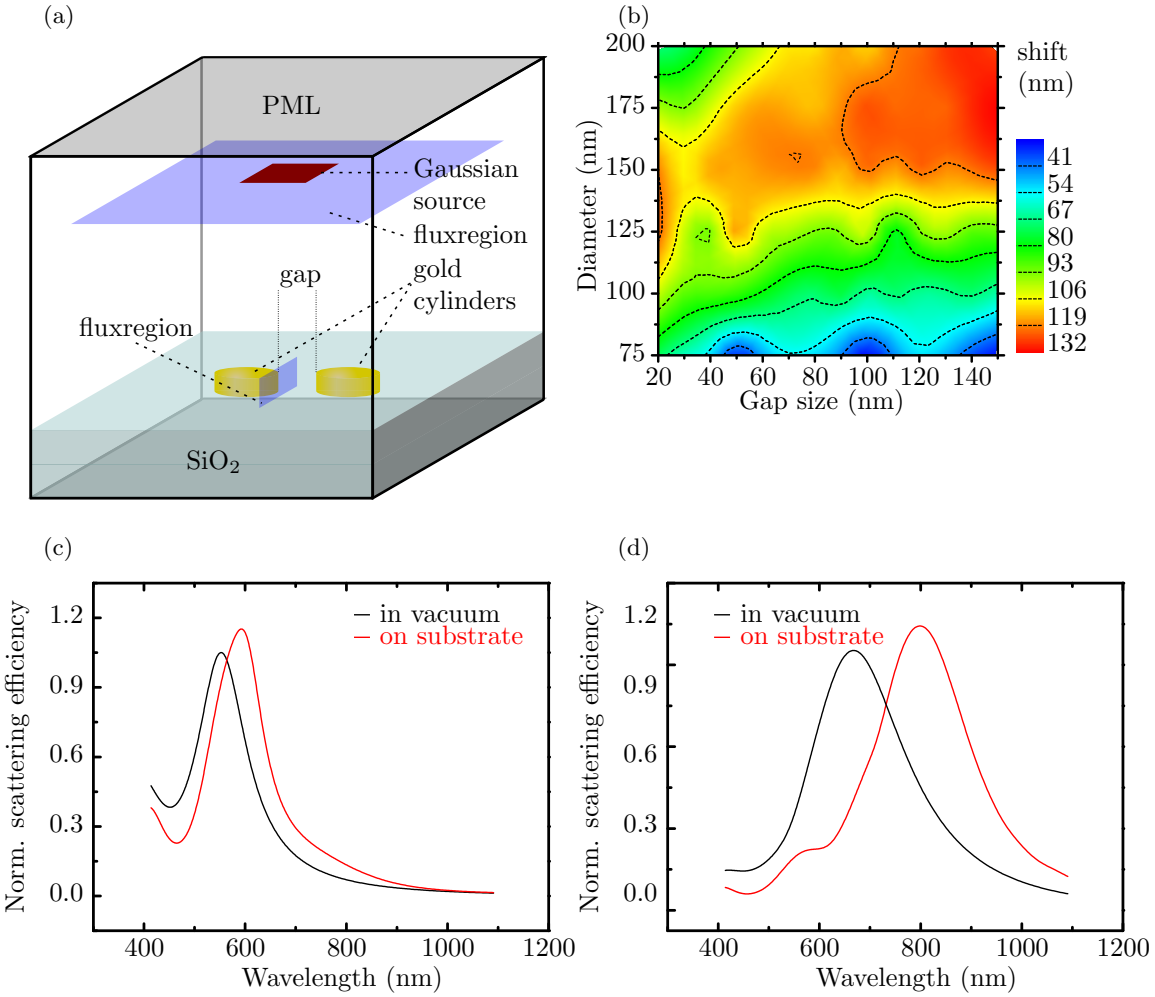

FIGURE 2.17: (a) Simulation environment for the simulation of the dimer antenna placed on a SiO_2 substrate. (b) 2D plot of the difference in position in the near field of the dipole mode between simulations with and without a SiO_2 substrate. (c) spectra for the lowest shift of the near field occurring at a gap size of 100 nm and an antenna diameter of 75 nm. (d) spectra of the highest shift of the near field occurring at a gap size of 175 nm and an antenna diameter of 150 nm.

2.3.4 Field distribution around gold dimer antennas

After investigating the spectral behavior of dimer antennas made of gold, the distribution of the electric field $|E|^2/|E_0|^2$ will be considered. For the calculations a gap size of 30 nm with cylindrical antennas of 100 nm in diameter was chosen. The substrate was SiO_2. This is the dimer antenna used later for the wavelength-scanned Raman measurements presented in Sec. 5.3. As the simulations required a significant amount of computation power and time, only one dimer antenna was investigated.

As described in Ref. [52], the field distribution around a dimer antenna is wavelength dependent. The subsequent computations were done using a plane wave source instead of the Gaussian source utilized beforehand. Thus, the field distribution at the frequency

of the plane wave was measured. Another approach would be to use a Gaussian source with subsequent Fourier transformation of the time-dependent fields. We decided to use the single-frequency plane-wave excitation to avoid numerical instabilities at the corner of the antennas that are likely to cause systematic errors in the Fourier transformation. The plane wave source was slowly switched on and off over four oscillations in order to keep its frequency width short and the computational time reasonable.

Additionally, the mesh size was lowered to 4 nm, resulting in a memory requirement of approximately 200 GiB with a computation time of about 10 h on 768 CPU's. The E-field at each grid point around the dimer antenna in a volume of 440 nm x 440 nm x 128 nm was recorded. This was done without the dimer antenna (for background correction) and with the dimer antenna (to obtain the scattered fields).

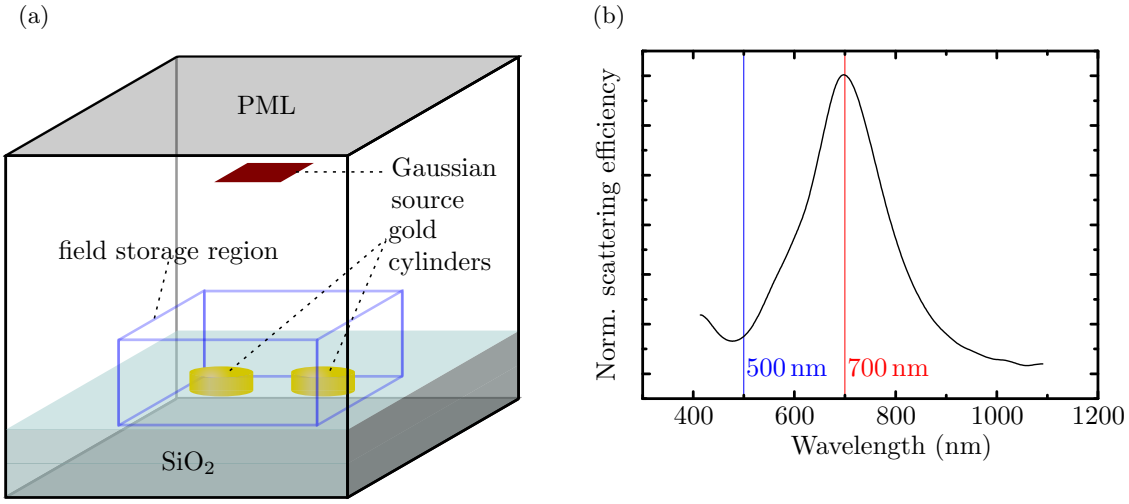

FIGURE 2.18: (a) computational cell used to calculate the field distribution around a gold dimer antenna. (b) near field scattering spectrum of the respective dimer antenna having a diameter of 100 nm and a gap size of 30 nm.

The computational cell is shown in Fig. 2.18 (a). Within the field storage region all directional components of the E-field are stored for every spatial and temporal point. The total intensity at each spatial point was obtained by calculating

$$|E|^2_{nlm} = \sum_i |E_x|^2_{nlmi} + |E_y|^2_{nlmi} + |E_z|^2_{nlmi}\,. \tag{2.65}$$

E_α represents the magnitude of the electric field in $\alpha = \{x, y, z\}$-direction. The index $nlmi$ indicates that this was done at every spatial point nlm over all time slices i. Thus, the total electric field was obtained. The total fields at every spatial point with and without antenna were divided yielding the $|E|^2/|E_0|^2$ enhancement for each spatial point.

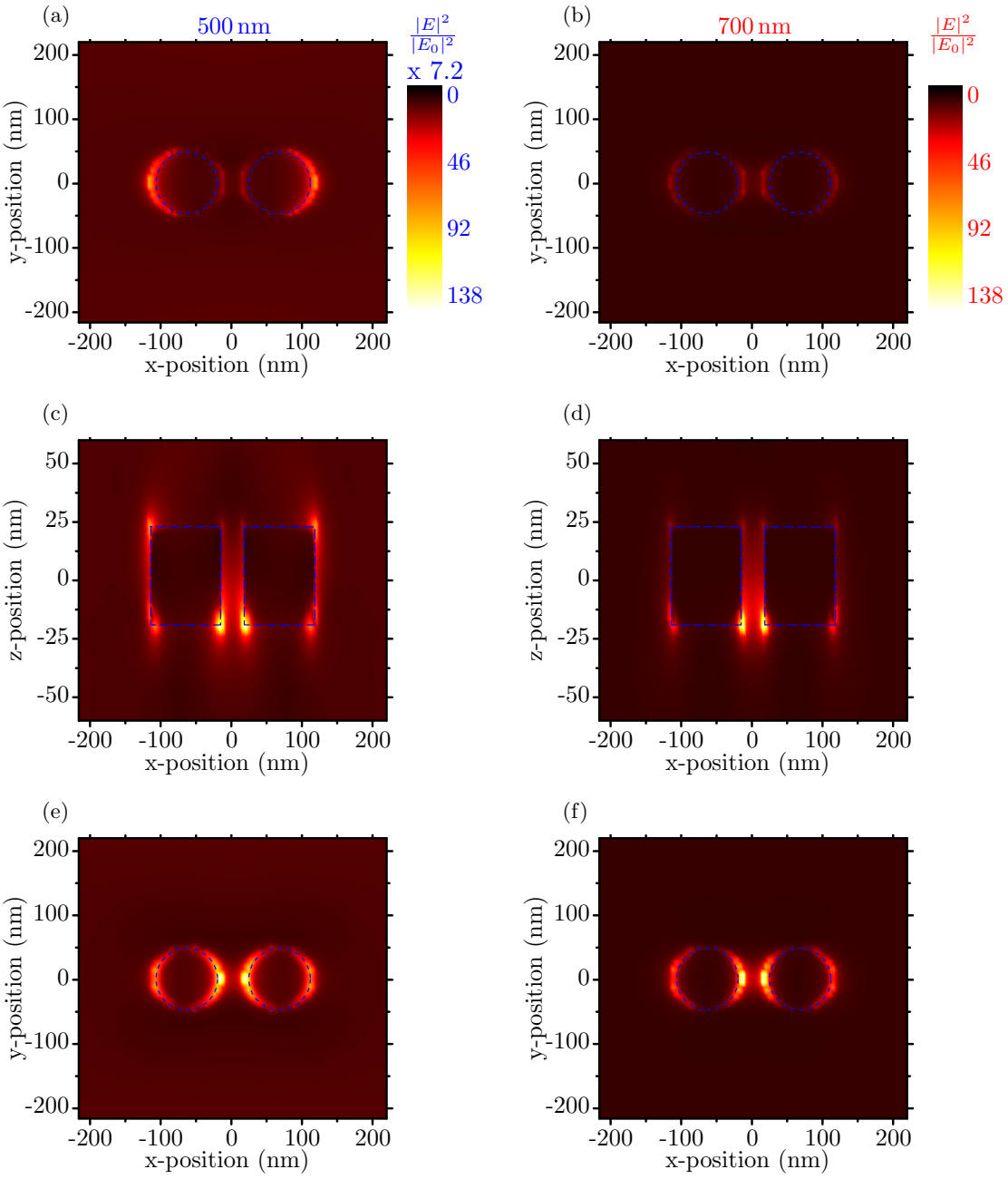

FIGURE 2.19: Field distribution around a dimer antenna with a diameter of 100 nm and a gap size of 30 nm in between. In the left column (plots (a), (c) & (e)) the field distribution for 500 nm excitation is shown. The field amplification was multiplied by 7.2 in order to account for the weaker amplification out of plasmonic resonance. In the right column (plots (b), (d) & (f)) the field distribution in plasmonic resonance for 700 nm is shown. The scales are equal for each column. Plots (a) and (b) show the fields on top of the dimer antenna. Plots (c) and (d) a cut through the center at $y = 0$. Plots (e) and (f) show the interface between the dimer antenna and the substrate.

Figure 2.18 (b) shows the near field spectrum of the simulated dimer antenna. We find the dipole resonance at 700 nm with a smaller quadrupole resonance around 570 nm. The field distribution was calculated for two wavelengths. Figure 2.19 shows $|E|^2/|E_0|^2$ around the dimer antenna out of resonance (500 nm excitation, left column) and in resonance (700 nm excitation, right column). Figures 2.19 (c) & 2.19 (d) show a cut through the center of the dimer antenna in x-direction. We observe that the fields show a different distribution on the top and bottom planes with higher enhancement at the interface to the substrate at the bottom. This was also observed in Refs. [17, 26]. As the field distributions around the dimer are different at each interface, they are given at the top (Figs. 2.19 (a) & 2.19 (b)) and bottom (Figs. 2.19 (e) & 2.19 (f)).

The maximum field intensity is found at the edges of the cylindrical antennas due to the lightning rod effect with the strongest enhancements occurring at the interface between the substrate and the cylindrical antennas (cf. Fig. 2.19). This is a consequence of the higher phase shift, the fields experience between the substrate and the cylindrical antennas.

Out of resonance (500 nm excitation) the maximum field intensity is 7.2 times weaker compared to resonant excitation (700 nm). Furthermore, the field distribution changes which is observable in Figs. 2.19. For 500 nm excitation the fields on top of the cylindrical antennas are 1.7 times weaker than at the bottom. For 700 nm excitation the fields on the top are 6.6 times weaker than at the bottom. The fields inside of the gap get pushed out as the coupled plasmon mode is not in resonance (cf. Fig. 2.19 (c) and 2.19 (d)). For 700 nm excitation we find that the fields are stronger inside of the gap as the coupled plasmon mode is in resonance. The ratio between maximum field intensity inside of the gap and the maximum field intensity outside of the dimer antenna is 0.3 for 500 nm excitation and 1.2 for 700 nm excitation.

It is instructive to analyze the field amplification and its distribution at the top of the dimer antenna because this is where the graphene will be situated. All components $|E_{x,y,z}|^2/|E_0|^2$ were plotted for an excitation wavelength of 700 nm in Fig. 2.20. The source was polarized along the dimer axis, i.e. only E_x-field components were exciting the dimer antenna. This is observable in Fig. 2.20 (a) having a paler background as the amplification around the dimer antenna is one due to Eq. (2.65). It is zero in Figs. 2.20 (b) & 2.20 (c) as the source does not emit any E_y- or E_z-field components.

The dimer antenna irradiates mainly E_x- and E_z-fields. This is expected as we excite a localized surface plasmon resonance (LSPR) created by free electrons confined within each single antenna. The excitation of additional E-field components is called depolarization and is explained by the high spatial localization of the LSPR that results in

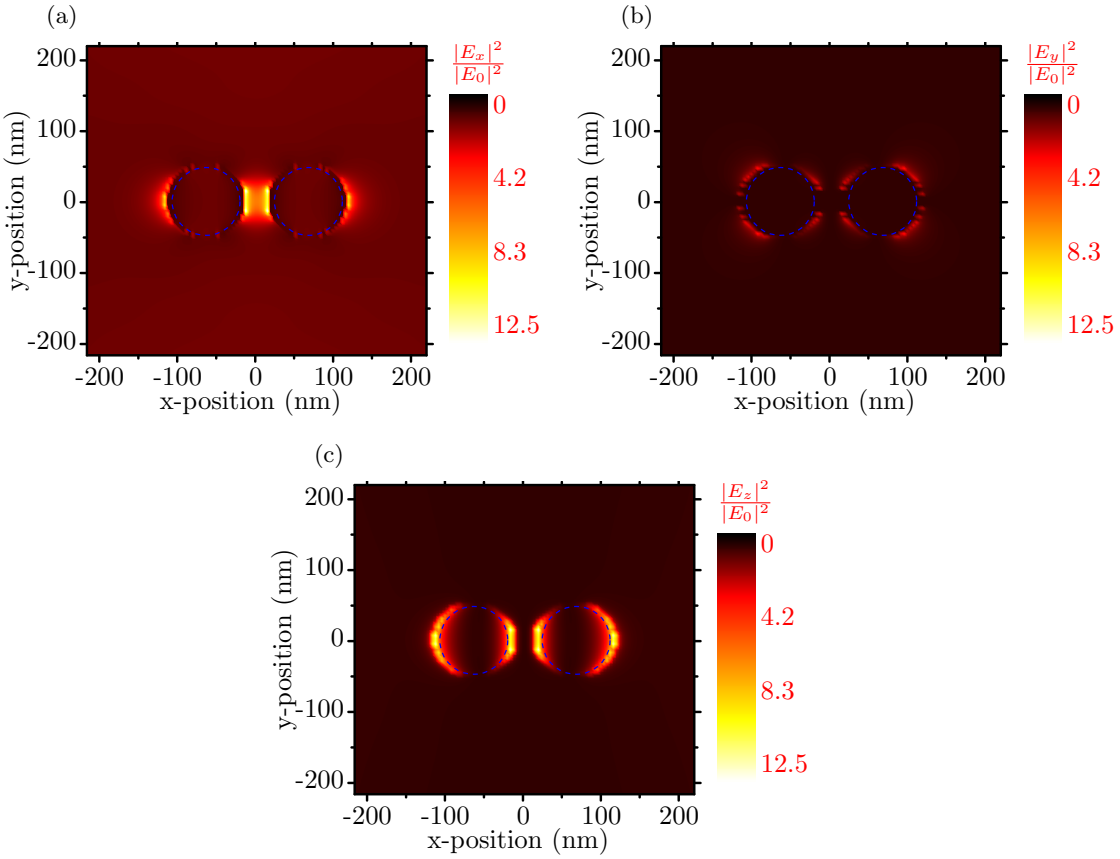

FIGURE 2.20: Field amplification at the top of a dimer antenna with a diameter of 100 nm and a gap size of 30 nm. The dimer antenna was excited at a wavelength of 700 nm in x-direction. The total amplification was separated into the single components (a) E_x, (b) E_y and (c) E_z.

the excitation of the additional components of the E-field [59–61]. The effect was experimentally demonstrated by Hubert et al. [62]. Surprisingly, the strength of the field intensity is similar for the E_x- and E_z-fields (cf. Figs. 2.20 (a) & 2.20 (a)). Additionally, a weak quadrupole field is being irradiated along the y-direction. The field enhancement of the quadrupole mode is only 26% of the x- and z-direction.

Figure 2.21 shows the amplification of the E-field components along the height of the gap. E_z is only enhanced at the top and bottom of the dimer antenna. E_x has a local maximum at the top of the dimer antenna and a more intense maximum at the bottom. Along the dimer height we find an increasing amplification of E_x in the direction of the substrate.

Maximum amplification occurs at the edges of the cylindrical antennas. The E_x-field has its absolute maximum at the boundary of the cylindrical antennas. The E_z-field extends about 4 nm into the vacuum. The field enhancement at the interface to the SiO_2 layer is about six times as high as the field enhancement at the interface to the vacuum. This ratio is the same for the amplification of the E_x- and E_z-components.

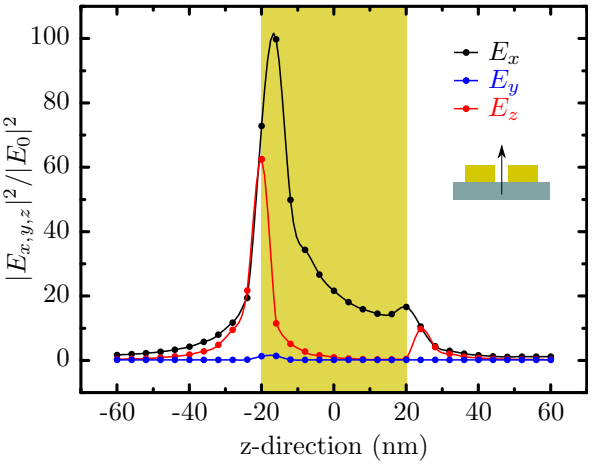

FIGURE 2.21: Amplification of the field components E_x, E_y and E_z inside the gap of a dimer antenna. The antenna is indicated by the light green region.

By exciting the dimer antenna along the y-direction instead of the x-direction we uncouple both cylindrical antennas. Thus, the field intensity in the gap vanishes which can be seen in the plots of Fig. 2.22 showing the enhancement of every field component for illumination in y-direction. We find that the maximum amplification is about 32% lower when the excitation is done in the y-direction. Again, we find a quadrupole mode irradiating perpendicular to the excitation direction and depolarization occurring for the E_z component. Comparing Figs. 2.20 & 2.22 we observe that the cavity creates more localized fields. This is well observable by comparing the field distribution in Figs. 2.20 (c) & 2.22 (c). Additionally, the depolarization ratio changes from $|\hat{E}_x|^2/|\hat{E}_z|^2 = 1.05$ for an excitation along the dimer axis to $|\hat{E}_y|^2/|\hat{E}_z|^2 = 0.80$ for an excitation perpendicular to it. This is attributed to the coupled plasmon mode in parallel illumination.

We found that the diameter and gap distance of a dimer antenna have a huge influence on its plasmonic resonance. The near field requires special attention as it interacts with a molecule and excites the Raman process. Thus, the design of a dimer antenna is crucial in order to obtain the desired resonance wavelength and field amplification. We showed that the field distribution around a dimer antenna is changed by the substrate and that the highest field amplifications occur at the interface to the substrate. However, the fields at the upper side of an antenna are also enhanced. An analyte will experience a high field strength when placed at the top of the gap. Yet, placing an analyte inside of the gap will expose it to even higher field strengths. It is important to note that depolarization takes place, exposing the analyte to field polarizations not emitted by the source.

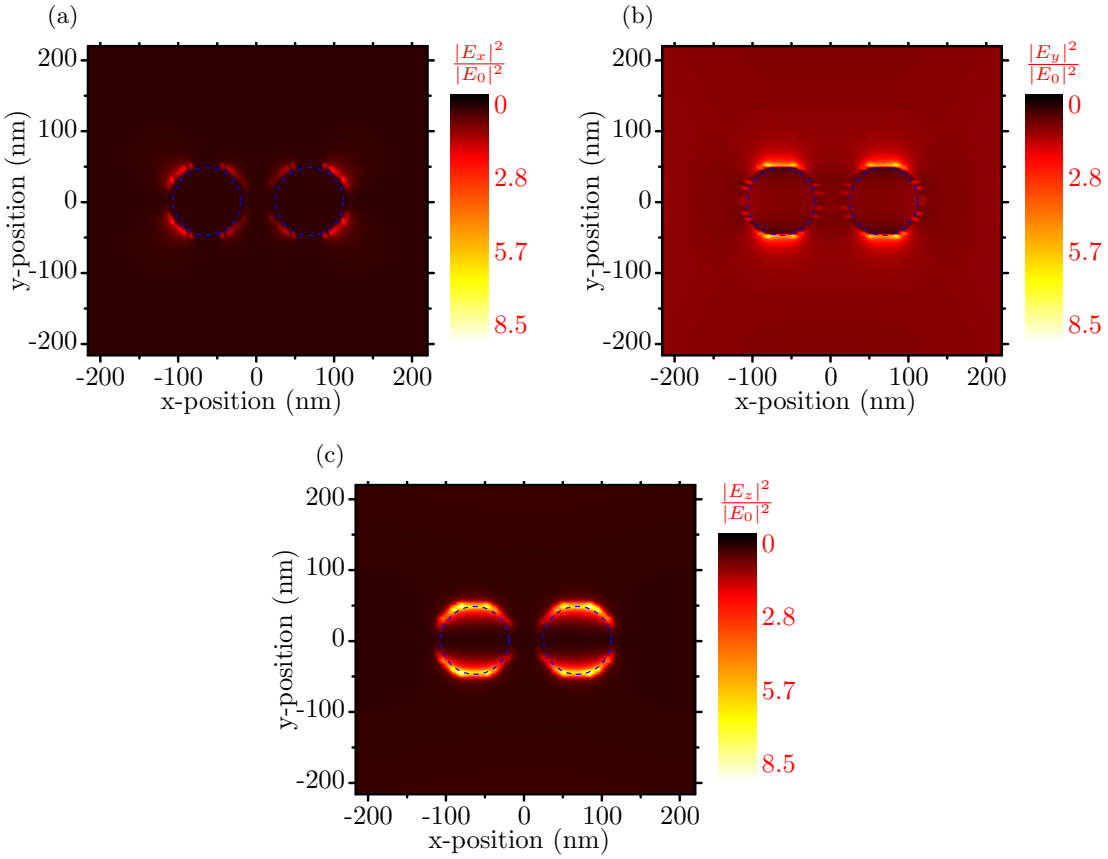

FIGURE 2.22: Field amplification at the top of a dimer antenna with a diameter of 100 nm and a gap size of 30 nm. The dimer antenna was excited at a wavelength of 700 nm in y-direction. The total amplification was separated into the single components (a) E_x, (b) E_y and (c) E_z.

2.3.5 Field enhancement by a dimer antenna

In the previous section we found that a dimer antenna creates a field amplification around it with the highest amplification in the cavity between the cylindrical antennas. In Sec. 4.3.2 the measured system is introduced. It consists of a graphene sheet being pulled into the cavity of the gap. According to Fig. 4.8 (a) the graphene sheet in being pulled into the cavity by about 4 nm. Thus, the following calculation was done using the field distribution found 4 nm beneath the top of the antenna.

As Raman scattering is proportional to the E-field intensity (cf. Eq. (3.12)) the majority of the Raman signal will be excited mainly in areas where we find a huge E-field amplification. These areas are indicated in Fig. 2.23 by the dotted lines. They include all points having an amplification of more than $|E|^2/|E_0|^2 = 46$ which is 33% of the maximum amplification. These areas include 93% of the total field intensity and cover an area of 0.0026 µm^2. It is reasonable to compare this area to the one illuminated by a laser incident on the dimer. The diameter of the laser spot is assumed to be 0.95 µm (cf.

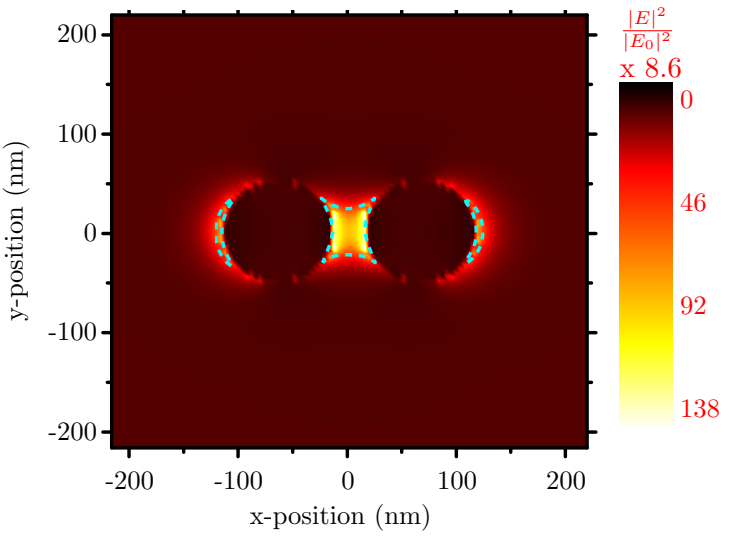

FIGURE 2.23: Area of field amplification 4 nm below the top of a dimer antenna. The areas having a field amplification above 46 are indicated by dashed lines.

Sec. 4.2) and therefore covers a total area of 0.71 µm^2. In Sec. 5.3 we will find that the measured Raman signal originates almost exclusively from the area shown in Fig. 2.23. Therefore, we will relate the area of the field amplification to the one illuminated by the laser to calculate the enhancement factor EF. This factor is a measure of how much the antenna amplifies the Raman signal intensity in comparison to the Raman signal intensity of the same analyte without amplification by a plasmonic antenna[14]. For the system investigated it is calculated according to

$$EF = \frac{A_{las}}{A_{ant}} \cdot \frac{I_{res}}{I_{out}} \tag{2.66}$$

with A_{las} being the area illuminated by the incident laser and A_{ant} being the area of the enhanced field by the antenna. This is multiplied by the ratio of the Raman intensities in resonance I_{res} and out of resonance I_{out}. The ratio of the spatial amplification calculates to $A_{las}/A_{ant} = 270$. In Chap. 5 we will use this finding to calculate the total enhancement factor EF of the system under investigation.

2.3.6 Scattering spectra of gold bowtie antennas

In this section we will briefly examine the scattering spectra of gold bowtie antennas. Far field scattering spectra were simulated to compare them to measured data, presented in Sec. 5.2.

Shadow nanosphere lithography (SNL) was used to produce bowtie antenna samples (cf. Sec. 4.3.1). This method produces unequally shaped bowtie antennas. Thus,

[14] An overview of different definitions of the enhancement factor EF was prepared by Le Ru et al. in Ref. [8].

we find a broad distribution of bowtie antenna and gap sizes. We also find varying curvatures of the tip apexes. This will be observed by looking at Fig. 4.6. Thus, the insight obtained by a detailed analysis of the scattering behavior of bowtie antennas is limited. Since the measurements shown in Sec. 5.2 average over many bowtie antennas the scattering spectrum will be broadened due to inhomogeneous shapes of the bowtie antennas. However, it is interesting to compare a simulation using the average size of the bowtie antennas and the average gap length with measured data obtained by dark field spectroscopy (cf. Sec. 4.1).

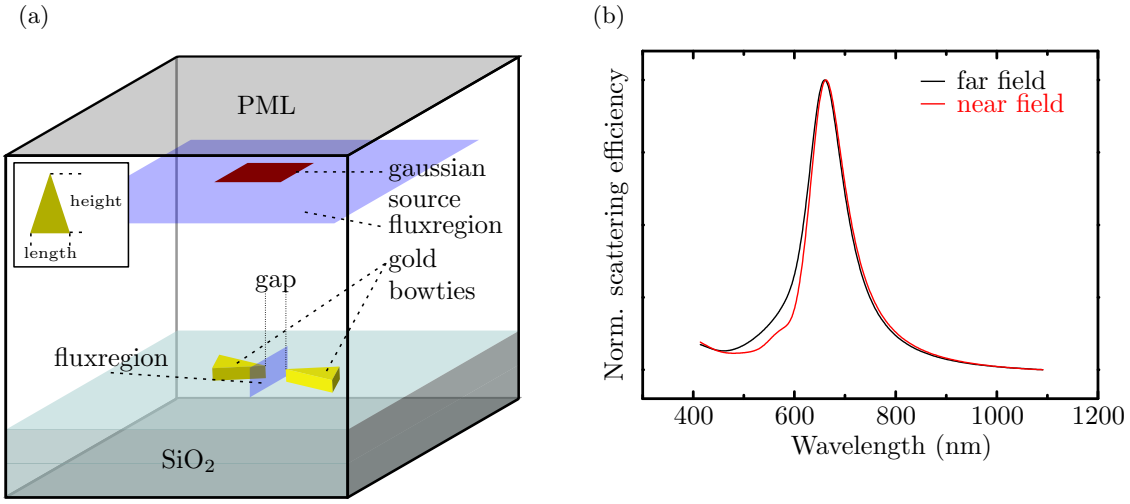

FIGURE 2.24: (a) 3D numerical cell used to calculate the field distribution of a bowtie dimer antenna, situated on a glass layer. The inset shows the naming convention for a triangle. (b) normalized near field and far field spectra of a bowtie antenna having a length of 106 nm, a height of 110 nm and a thickness of 20 nm.

The far field and near field spectrum for the bowtie antennas used in Sec. 5.2 was calculated using the average dimension of the bowtie antennas found in Fig. 4.6. They are on average 106 nm in length, 110 nm in height and have a thickness of 20 nm. The naming convention is shown in the inset of Fig. 2.24 (a).

Figure 2.24 (b) shows the near and far field spectra of bowtie antennas having the average dimensions given above. We find a resonance of 660 nm in the near field and far field scattering efficiency. The quadrupole mode is observable in the near field due to the high area of curvature of the tip apex. The high curvature increases the field strength due to the lightning rod effect [33]. Thus, the quadrupole mode reaches the fluxregion and is observable in the near field scattering cross section at a wavelength of 580 nm.

In order to calculate the enhancement factor of the bowtie antennas used in Chapter 5 we use the same ratio of $A_{las}/A_{ant} = 270$ as obtained in the previous section for a dimer

antenna. This is a reasonable assumption as bowtie antennas show a similar scattering behavior as dimer antennas with a comparable diameter and gap size. Additionally, it is not possible to calculate the exact field distribution for the bowtie antennas measured in Sec. 5.2 as their exact dimensions could not be measured due to the graphene deposited on top of them. The reason was that before deposition of the graphene it was not possible to measure the position of the plasmonic hotspots.

2.4 Electromagnetic SERS resonance theory

This section will be concluded by presenting the existing theory of SERS. The amplification of the Raman cross section according to this theory is caused by the near field of an antenna an analyte is being exposed to. Although the enhancement of the Raman signal is being described, no detailed knowledge of Raman scattering is required to understand the theory.

In Sec. 2.3.4 it was shown that plasmonic antennas channel light into small fractions of space. The first attempts to describe the electromagnetic contribution to the enhancement of the Raman signal were carried out in Refs. [12] and [13]. Both used Mie theory to describe the scattering behavior of a particle being much smaller than the wavelength of the electromagnetic field using a quasistatic approximation of the field inside the particle.

Contrary to the theory worked out in Sec. 3.5 they assume an enhancement purely resulting from the amplification of the electromagnetic fields in the vicinity of the particle. Thus, they predict a single resonance resembling the extinction spectrum of the antennas for an analyte with no intrinsic resonances as graphene. In Chapter 5 we will see that this is not the case and the theory described here is not applicable for the measurements presented later on.

According to Ref. [13] a small particle behaves like it is a polarized dipole and the enhancement factor EF is estimated using

$$EF = \left| \left(1 + 2\frac{n_s^2 - 1}{n_s^2 + 2}\right) \left(1 + 2\frac{n_0^2 - 1}{n_0^2 + 2}\right) \right|. \tag{2.67}$$

From this equation we learn that a part of the resonance is given by the refractive index of the particle. Mainly caused by the requirement that a plasmon has to be excitable within the particle. Based on this finding, several authors used a dipole approximation to calculate the enhancement of rough metal surfaces [63, 64]. Moskovits et al. (Ref. [9]) extended this theory by including shape effects.

Within the context of this theory, the field enhancement of a metal nanoantenna is calculated and used to obtain the SERS enhancement assuming a conventional Raman process with $I \propto |E_L|^2$ with E_L being the local near field the analyte is exposed to. This resulted in the formulation of the SERS enhancement factor G (cf. Ref. [9])

$$G = \left| \frac{\alpha_R}{\alpha_{R0}} \right| \left| gg' \right|^2 \tag{2.68}$$

with g being the field enhancement averaged over the surface of the particle for the excitation wavelength and g' being the same for the Raman scattered wavelength. α_{R0} is the Raman polarisability of the isolated molecule and α_R the Raman polarisability of the molecule near the metal particle.

Assuming a small Raman shift we find $g \approx g'$. We obtain $g \propto \vec{E}_L$ and thus $|g^2|^2 \propto |E_L|^4$ according to Ref. [9]. This is sometimes referred to as the fourth power law.

A different formulation is given in Ref. [4] by

$$EF_{SERS} = \frac{\left|E_p(\omega_L)^2\right| \left|E_p(\omega_L - \omega_{ph})^2\right|}{E_0^4}. \tag{2.69}$$

With E_p being the field strength at the surface of the particle for the laser frequency ω_L and the scattered frequency $\omega - \omega_{ph}$. E_0 is the strength of the incident electromagnetic field.

A quadratic enhancement of the Raman intensity for small Raman shifts is obtained. For higher Raman shifts the enhancement depends on the resonance properties of the metal particle.

Using the findings of Sec. 2.3.2.2 we conclude that no spectrally narrow resonances are to be expected for plasmonic enhancement. According to the theory described above, the amplification is mainly determined by the plasmonic near field resonance of the antenna. Specifically, the width of the resonance is equal to the width of the near field resonance from the antenna which was calculated in Sec. 2.3.2.2.

Wavelength-scanned SERS measurements have been carried out before but only to a very small extend due to the difficulty of the measurements. Some papers were published by the group of van Duyne on homogeneous lattices consisting of bowtie antennas [4, 29]. These measurements established the wavelength of highest amplification to be at $(\lambda_{LSPR} + \lambda_{phonon})/2$, averaging over an area of about 1.5 μm^2 [4]. Thus, the measured Raman signal was likely to contain the contribution of many antennas deviating in shape due to their manufacturing process[15]. However, in Sec. 2.3.2.2 we found that the shape

[15] Reference [4] used nanosphere lithography (NSL) to create a surface covered with a hexagonal bowtie structure. Section 4.3.1 describes NSL and the inhomogeneity in shape of the obtained bowtie antennas.

strongly influences the plasmonic near field maximum. Narrow spectral features are likely to be broadened due to averaging over many different antennas.

Chapter 3

Raman scattering

In this chapter the classical theory of Raman scattering will be introduced. It will be presented using quantum mechanics and perturbation theory.

A description of the resonant Raman process of the 2D mode in graphene will be given and expanded to include metallic antennas. This theory will allow very narrow Raman resonances originating from the plasmonic antenna that enhances the Raman signal of graphene. These narrow resonances were observed in wavelength-scanned Raman experiments presented in Sec. 5.3.

3.1 Physical properties of graphene

A brief introduction into the physical properties of graphene will be given in order to understand its Raman modes. Considering the real space alignment of the atoms, graphene has 2 atoms in its unit cell (Fig. 3.1). Ideally, it forms a perfect honeycomb structure and therefore has D_{6h} symmetry. When we have a look at the first Brillouin zone we find four high-symmetry points. According to Ref. [65], they are $\Gamma(D_{6h}), M(D_{2h}), K(D_{3h}), K'(D_{3h})$ with their equivalent point group given in parentheses.

Figure 3.2 (a) shows the electronic band structure of graphene. A nearest-neighbor tight-binding approach was used. It considers interactions between an atom A and its nearest neighbors B_1, B_2 and B_3 (Fig. 3.1). By using the tight-binding Hamiltonian H and considering the overlap of the wave functions S we need to solve the eigenvalue problem

$$\begin{vmatrix} H_{AA}(\vec{k}) - E(\vec{k})S_{AA}(\vec{k}) & H_{AB}(\vec{k}) - E(\vec{k})S_{AB}(\vec{k}) \\ H^*_{AB}(\vec{k}) - E(\vec{k})S^*_{AB}(\vec{k}) & H_{AA}(\vec{k}) - E(\vec{k})S_{AA}(\vec{k}) \end{vmatrix} = 0. \tag{3.1}$$

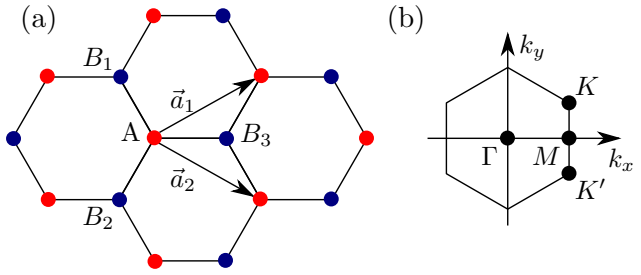

FIGURE 3.1: (a) real space unit cell of graphene with the unit vectors $\vec{a}_1$ and $\vec{a}_2$. The atomic basis consists of 2 atoms A (red) and B (blue). (b) 1st Brillouin zone of graphene with the high symmetry points Γ, M, K and K'. K and K' are inequivalent points.

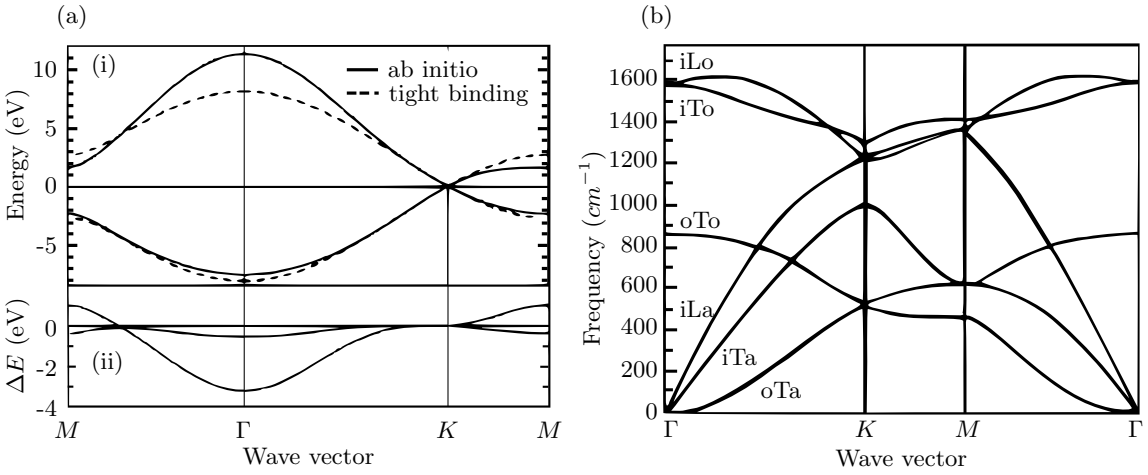

FIGURE 3.2: (a) electronic dispersion of graphene obtained by ab initio and nearest-neighbor tight-binding calculations. (i) shows the dispersion for both calculations. (ii) shows the difference between the dispersions. Taken from Ref. [66]. (b) calculated phonon dispersion of graphene showing the iLo, iTo, oTo, iLa, iTa and oTa phonon branches. Taken from Ref. [65], calculated by Ref. [67].

Reference [66] shows the full derivation. Here, the resulting nearest-neighbor tight-binding energy dispersion will directly be written

$$E^{\pm}(\vec{k}) = \frac{\epsilon_{2p} \mp \gamma_0 \sqrt{f(\vec{k})}}{1 \mp s_0 \sqrt{f(\vec{k})}} \tag{3.2}$$

with

$$f(\vec{k}) = 3 + 2\cos\vec{k}\cdot\vec{a}_1 + 2\cos\vec{k}\cdot\vec{a}_2 + 2\cos\vec{k}\cdot(\vec{a}_1 - \vec{a}_2). \tag{3.3}$$

The dispersion was plotted in Fig. 3.2 (a) using $\epsilon_{2p} = 0\,\text{eV}$, $s_0 = 0\,\text{eV}$ and $\gamma_0 = -2.7\,\text{eV}$. The parameters were found by fitting ab initio calculations. The differences between both approaches are shown in the lower part of Fig. 3.2 (a).

In Fig. 3.2 (a) we find that the dispersion around the K point is linear. This may also be found using Eq. 3.2 and inserting the Taylor expansion of Eq. 3.3 for $|\vec{k}| \ll 1$. Thus

it is a good approximation to use a linear band dispersion for small excitation energies of up to 2.7 eV [66]. In Sec. 3.4.2 this finding will be used. The linear approximation of the band structure of graphene around the K point is commonly referred to as Dirac cone.

A Kohn anomaly is an anomaly in the phonon dispersion of metals. It occurs for wave vectors where the screening of lattice vibrations by ions changes rapidly. The energy of a phonon is considerably lowered and a discontinuity in the derivative of the phonon dispersion occurs ($\nabla_{\vec{q}}\omega(\vec{q}) = \infty$) [68]. Kohn anomalies happen for all phonon vectors $\vec{q}$, where one can find two electronic states $\vec{k}_1$ and $\vec{k}_2 = \vec{k}_1 + \vec{q}$, that are located at the Fermi surface [68]. In graphene we find that the electronic band gap is zero at the equivalent K and K' high symmetry points (cf. Fig. 3.1 (b) and 3.2 (a)). These points are connected by the wavevector $\vec{K}$, resulting in two Kohn anomalies at the high symmetry points $\vec{k} = \Gamma$ and $\vec{k} = \mathrm{K}$ [69] of graphene, shown in Fig. 3.3. Reference [69] points out that the phonon dispersion is linear around the two Kohn anomalies for small wave vectors. This is the reason why we observe linear dispersions for the D and 2D modes which will be treated later in Sec. 3.4.1.

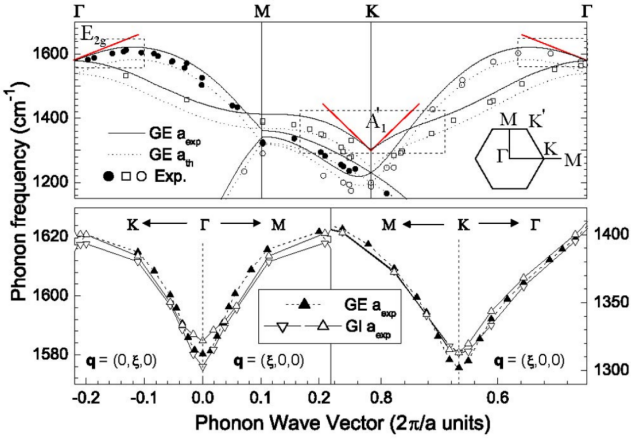

FIGURE 3.3: Phonon dispersion of graphene calculated by density functional theory (DFT). The Kohn anomalies are indicated by the red straight lines in the upper panel with experimental values (points and squares). The lower panel shows the dotted regions from the upper panel with calculated values indicated by triangles. From Ref. [69].

Figure 3.2 (b) shows the phonon dispersion of graphene, calculated using density functional theory (DFT), taken from Ref. [67]. Because of the twinatomic base we observe six bands having three acoustic and three optical branches. In Fig. 3.2 (b) we find in-plane (i) modes and out-of-plane (o) modes that refer to the movement of the carbon atoms with respect to the graphene lattice plane. The primary interest is in the iTo and iLo modes which are Raman active due to their E_{2g} symmetry at the Γ point [65]. As described above, we find a linear phonon dispersion at the Γ and K point [70]. This is

caused by a Kohn anomaly at these high symmetry points resulting in a renormalization of the phonon energy according to Refs. [68, 69]. An easier calculation, neglecting the Kohn Anomaly but having a reasonable agreement with measurements may be found in Ref. [66].

Trigonal warping refers to the triangular distortion of the equi-energy contours of the electronic band structure and phonon dispersion of graphene near the K point [71, 72]. It is found in materials with a threefold symmetry axis [71]. Figure 3.4 shows the influence of the trigonal warping effect to the phonon dispersion and electronic band structure of graphene. Figure 3.4 (b) depicts the equi-energy contours for 2.41 eV and 2.54 eV of the electronic band structure of graphene (dotted lines) and phonon equi-frequency contours (solid lines). The dots show experimental data measured using resonant Raman scattering. They are situated on the equi-energy contours since resonant Raman scattering is resonant in energy but not in phonon frequency. It is observable that the electronic equi-energy contours and the phonon equi-frequency contours have slightly different shapes. Albeit both are trigonally distorted. Additionally, Fig. 3.4 (b) shows that the distortion is less pronounced for small values of $|\vec{k}|$, allowing the assumption of circular equi-energy and equi-frequency contours called Dirac cone for small values of $|\vec{k}|$. This reasonable assumption will be used later on.

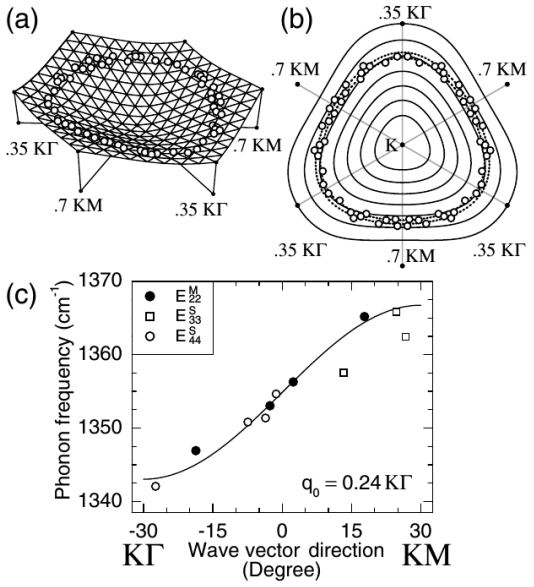

FIGURE 3.4: (a) phonon dispersion relations around the K point of the 2D BZ of graphite, including experimental points shown by dots. (b) Phonon equi-frequency contours (solid lines), experimental q points (dots) and electronic equi-energy contours (dotted lines). (c) dependence of the phonon dispersion on the direction of the q-vector. From Ref. [71]

3.2 Macroscopic theory of Raman scattering

A short introduction into the classical theory of Raman scattering following Refs. [73, 74] will be given.

When an electromagnetic (EM) wave encounters a solid it interacts by inducing a polarization in the solid. This is expressed by $\vec{P} = \chi\vec{E}$ [33]. χ is the dielectric susceptibility and accounts for the polarisability of a solid. $\vec{E}$ is the incident electromagnetic field and $\vec{P}$ the resulting polarization. This results in the absorption and transmission of an incident EM wave by the solid.

In 1928 C.V. Raman showed experimental evidence that light interacts inelastically with solids [75]. This interaction is called Raman scattering and has become a widely used method of the non-invasive analysis of molecules and solids [73]. It also has become a versatile tool for the investigation of graphene [65] and carbon nanotubes due to their informative Raman features [76].

Let us assume an incident planar EM wave $\vec{E}(\vec{r},t)$ with amplitude $\vec{E}_0(\vec{k}_i,\omega_i)$

$$\vec{E}(\vec{r},t) = \vec{E}_0(\vec{k}_i,\omega_i)\cos(\vec{k}_i\vec{r} - \omega_i t) \tag{3.4}$$

induces a polarization

$$\begin{aligned} \vec{P}(\vec{r},t) &= \vec{P}_0(\vec{k}_i,\omega_i)\cos(\vec{k}_i\vec{r} - \omega_i t) && (3.5)\\ &= \chi(\vec{k}_i,\omega_i)\vec{E}_0(\vec{k}_i,\omega_i)\cos(\vec{k}_i\vec{r} - \omega_i t), && (3.6) \end{aligned}$$

where the scalar constant $\chi(\vec{k}_i,\omega_i)$ represents the susceptibility of the solid. $\chi(\vec{k}_i,\omega_i)$ depends on the atomic displacement $\vec{Q}(\vec{r},t)$. As the amplitude of $\vec{Q}(\vec{r},t)$ is small compared to the lattice constant at room temperature, $\chi(\vec{k}_i,\omega_i)$ can be approximated using a Taylor series in $\vec{Q}(\vec{r},t)$

$$\chi(\vec{k}_i,\omega_i,\vec{Q}) \approx \chi_0(\vec{k}_i,\omega_i) + \left.\frac{\delta\chi}{\delta\vec{Q}}\right|_0 \vec{Q}(\vec{r},t) + \dots \tag{3.7}$$

Inserting Eq. (3.7) into Eq. (3.6) we get two terms

$$\vec{P}(\vec{r},t,\vec{Q}) \approx \vec{P}_0(\vec{r},t) + \vec{P}_{ind}(\vec{r},t,\vec{Q}) + \dots \ . \tag{3.8}$$

Thus, we obtain an induced polarization $P_{ind}(\vec{r},t,\vec{Q})$ and an intrinsic polarization $P_0(\vec{r},t)$ within the solid under illumination. A plane wave will be introduced to describe the

quantized atomic displacement $\vec{Q}(\vec{r},t)$, referred to as phonon [77, 78]

$$\vec{Q}(\vec{r},t) = \vec{Q}(\vec{q},\omega_0)\cos(\vec{q}\,\vec{r} - \omega_0 t). \tag{3.9}$$

Inserting Eq. (3.9) into $\vec{P}_{ind}(\vec{r},t,\vec{Q})$ from Eq. (3.8) and rearranging the cosine terms, results in

$$\begin{aligned}\vec{P}_{ind}(\vec{r},t,\vec{Q}) =& \frac{1}{2}\left.\frac{\partial\chi}{\partial\vec{Q}}\right|_0 \vec{Q}(\vec{q},\omega_0)\vec{E}_0(\vec{k}_i,\omega_i)\cdot \\ &\cdot\Big\{\underbrace{\cos\Big((\vec{k}_i+\vec{q})\vec{r}-(\omega_i+\omega_0)t\Big)}_{Anti\text{-}Stokes} + \underbrace{\cos\Big((\vec{k}_i-\vec{q})\vec{r}-(\omega_i-\omega_0)t\Big)}_{Stokes}\Big\}\end{aligned} \tag{3.10}$$

Thus, we get two waves shifted in wavevector and frequency, known as Stokes and anti-Stokes. In other words the incoming light of frequency ω_0 is inelastically scattered resulting in two emitted waves that appear next to the laser line. One is shifted to lower frequencies with $\vec{k}_i - \vec{q}$ and $\omega_i - \omega_0$ and is called Stokes. The other one is shifted to higher frequencies with $\vec{k}_i + \vec{q}$ and $\omega_i + \omega_0$ and is called anti-Stokes. An exemplary spectrum is shown in Fig. 3.5.

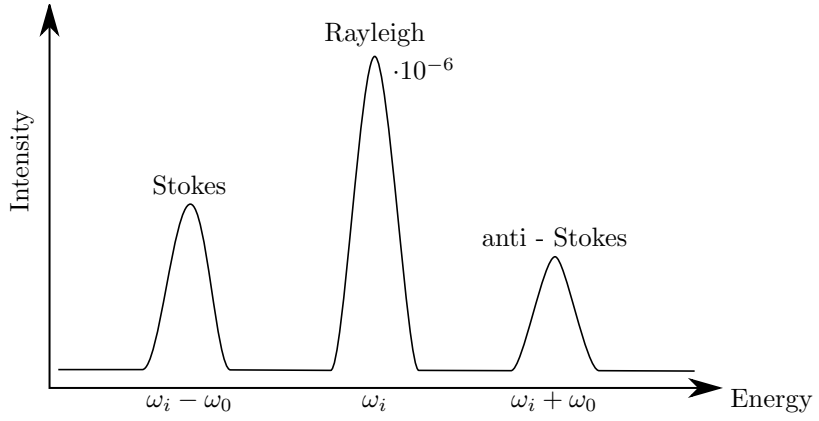

FIGURE 3.5: Spectrum of Rayleigh, Stokes and anti-Stokes Raman scattering. $\hbar\omega_0$ is the energy of the phonon and $\hbar\omega_i$ the energy of the laser.

We will use Eq. (3.10) to learn more about the properties of Raman scattering. Neglecting the cosine terms we find a vector product which may be zero under certain

conditions. Using Einsteins notation we rewrite $\vec{P}_{ind}(\vec{r}, t, \vec{Q})$

$$\begin{aligned} \vec{P}_{ind}(\vec{r}, t, \vec{Q}) &\propto \left(\frac{\partial \chi}{\partial \vec{Q}}\right) \vec{Q}(\vec{q}, \omega_0)\vec{E}_0(\vec{k}_i, \omega_i) \\ &= \left(\frac{\partial \chi_{ij}}{\partial Q_k}\right) Q_k(\vec{q}, \omega_0)\vec{E}_0(\vec{k}_i, \omega_i) \\ &= (\chi_{ij,k})Q_k \cdot (E_0)_j \\ &= R^k_{ij} \cdot E_{0j} \\ &= \Re \vec{E}_0. \end{aligned} \tag{3.11}$$

This relation indicates that a polarization is induced when the susceptibility does not vanish for displacements along the direction of the incident wave. Using the same argument, the scattered wave, $\vec{E}_s \cdot \vec{P}_{ind}$ also needs to have nonvanishing components. This way we obtain the intensity of the Raman scattered light

$$I_s \propto \left|\vec{E}_s \cdot \Re \cdot \vec{E}_0\right|^2 \equiv \left|\vec{E}_i \cdot \Re \cdot \vec{E}_s\right|^2. \tag{3.12}$$

$\Re$ is called the Raman tensor. From Eq. (3.12) we conclude that only certain polarizer/analyzer combinations $(\vec{E}_i, \vec{E}_s)$ contribute to the Raman intensity. Namely those resulting in a non-zero vector product in Eq. (3.12).

$\Re$ depends on the atomic structure of the solid under investigation (cf. Eq. (3.11)). The non-zero elements of the Raman tensor are obtained using group theory and the symmetry characteristics of the atomic lattice of the solid. We are able to decompose $\Re$ according to its irreducible representation and rewrite Eq. (3.12) as

$$I_s \propto \sum_n \left|\vec{E}_i \cdot \Re_n \cdot \vec{E}_s\right|^2. \tag{3.13}$$

Every phonon is represented by its irreducible representation $\Re_n$ and we get the total Raman intensity by summing over all phonons.

3.3 Microscopic theory of Raman scattering

Until now, Raman scattering was described without the consideration of microscopic processes taking place in the solid. In the description above any resonance effects, where the Raman intensity I_s is a function of ω_i are included in $\chi(\vec{k}_i, \omega_i)$. The following section will further elucidate this behavior. Again, we will follow Refs. [73, 74] for the presentation.

The Hamiltonian used is

$$\mathcal{H} = \mathcal{H}_0 + \mathcal{H}_{eR} + \mathcal{H}_{eL}. \tag{3.14}$$

$\mathcal{H}_0 = \mathcal{H}_e + \mathcal{H}_l$ is the contribution from the electron and lattice vibrations. $\mathcal{H}_{eR}$ is the contribution from electrons interacting with incoming radiation and $\mathcal{H}_{eL}$ describes the interaction involving the lattice of the solid (electron-phonon-interaction).

Basically, Raman scattering involving one phonon requires the following steps:

1. An incident photon excites the solid, creating an electron-hole pair into a virtual state $|a\rangle$ (described by $\mathcal{H}_{eR}$)
2. The electron-hole pair is scattered into another state $|b\rangle$ (by $\mathcal{H}_{eL}$)
3. The electron-hole pair recombines radiatively back to the ground state (by $\mathcal{H}_{eR}$)

A thorough description of this process requires us to use quantum electrodynamics (QED) which is beyond the scope of this work. Here, the semiclassical treatment from Ref. [73] will be given as it is sufficient to describe the observations made in Sec. 5.3.

In order to describe the microscopic processes involved, Feynman diagrams will be used. They follow some simple rules:

- Excitations like photons, phonons, etc. are drawn by lines. They are called **propagators**.
- Interactions between two excitations are represented by intersections of their propagators. They are called **vertices**.
- Propagators have an arrow indicating whether their excitations are created or annihilated. An arrow pointing towards a vertex means annihilation and an arrow pointing away from a vertex means creation.
- The sequence of the interactions taking place is from left to right.
- Once a process has been drawn, other equivalent processes can be derived by permutation of the time order of the initial process.

Figure 3.6 shows a representative Feynman diagram in the upper section (a) and an overview of the symbols used in the lower section (b).

In Fig. 3.7 all possible scattering paths for a one-phonon Stokes scattered photon are shown. These scattering paths will be translated into their respective contribution to the expansion of the scattering probability P_{ph}. The contribution from Fig. 3.7 (a) will

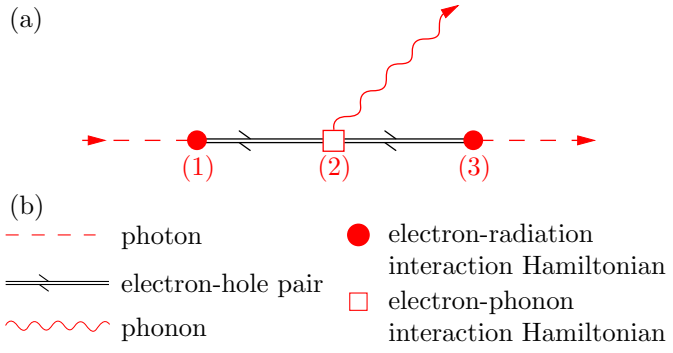

FIGURE 3.6: Explanation of the usage of Feynman diagrams. (a) a Feynman diagram for one-phonon stokes Raman scattering (described in this chapter). (b) explanation of the symbols used. From Ref. [73].

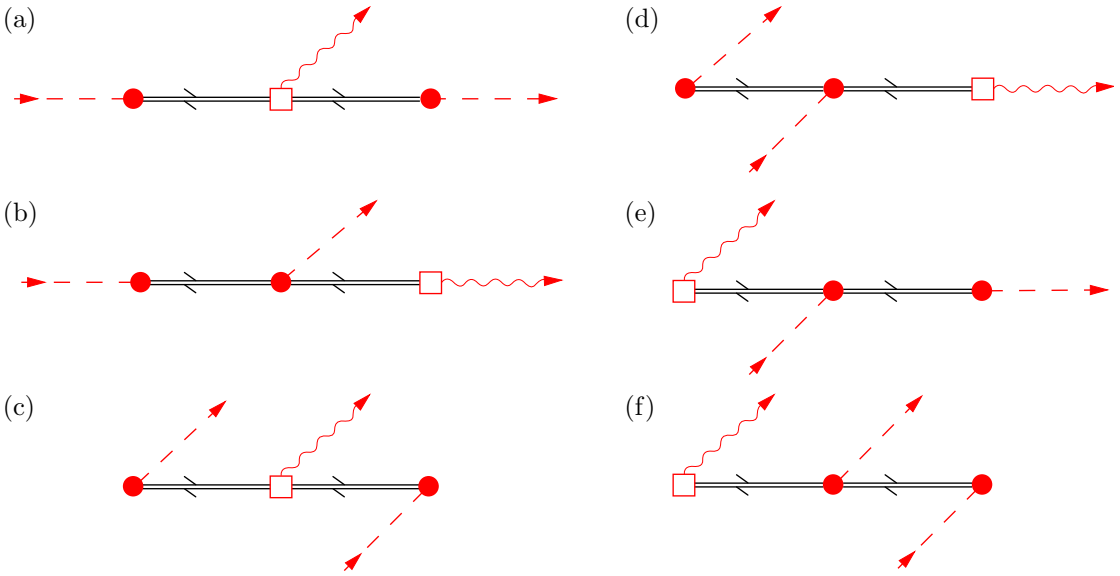

FIGURE 3.7: Feynman diagrams of the scattering processes contributing to a one-phonon stokes Raman process (a-f). (b-f) are permutations of (a). From Ref. [73]

be used as an example. The first vertex describes how the incident state $|i\rangle$ interacts with an incoming photon of energy $E_i = \hbar\omega_i$ and thus creates an electron-hole pair $|1\rangle$ via $\mathcal{H}_{eR}$. This electron-hole pair is scattered via $\mathcal{H}_{eL}$ and a phonon of energy $\hbar\omega_0$ is created. Thus, the system enters the state $|2\rangle$. Finally, a new photon is released by $\mathcal{H}_{eR}$ and the system returns to its initial state $|i\rangle$ by emitting the scattered photon of energy $\hbar\omega_s$.

A mathematical formulation will be derived using Fermi's golden rule that gives us the probability for a transition from the state $|k_2\rangle$ to $|k_1\rangle$

$$\begin{aligned} P(\vec{k}_1, \vec{k}_2) &= \frac{2\Pi}{\hbar} \left| \langle \vec{k}_1 | \, \mathcal{H}_{scatt} \, | \vec{k}_2 \rangle \right|^2 \rho_f \\ &= \frac{2\Pi}{\hbar} \left| \frac{\langle \vec{k}_1 | \, \mathcal{H}_{scatt} \, | \vec{k}_2 \rangle}{E(k_1) - E(k_2)} \right|^2 . \end{aligned} \tag{3.15}$$

The density of final states ρ_f was rewritten, assuming there is an infinite amount of final states when approaching a Van Hove singularity[1] for the transition between $|\vec{k}_1\rangle$ and $|\vec{k}_2\rangle$.

Using Eq. (3.15) we may write the contribution from Fig. 3.6 (a) to the scattering probability P_{ph} according to

$$P_{ph}(\omega_s) = \left(\frac{2\Pi}{\hbar}\right) \left| \sum_{1,2} \frac{\overbrace{\langle i|\,\mathcal{H}_{eR}(\omega_s)\,|2\rangle}^{(3)} \overbrace{\langle 2|\,\mathcal{H}_{eL}\,|1\rangle}^{(2)} \overbrace{\langle 1|\,\mathcal{H}_{eR}(\omega_i)\,|i\rangle}^{(1)}}{\underbrace{[\hbar\omega_i - (E_1 - E_i)]}_{(1)} \underbrace{[\hbar\omega_i - \hbar\omega_0 - (E_2 - E_i)]}_{(2)}} \right|^2 \cdot \underbrace{\delta\left[\hbar\omega_i - \hbar\omega_0 - \hbar\omega_s\right]}_{(3)}. \tag{3.16}$$

The states $|1\rangle$ and $|2\rangle$ with their corresponding energies E_1 and E_2 are virtual states. We have a continuum of possible states that needs to be summed over. The curly braces in Eq. (3.16) show the contributions from each vertex in Fig. 3.6 (a). The denominator from vertex (3) in Fig. 3.6 (a) leaves us with a term for the total change in energy, reformulated using a delta function. Therefore, Raman scattering obeys energy conservation as expected. However, it is important to state that energy is conserved in total but not for the individual scattering processes.

From Eq. (3.16) we find that every vertex has a resonance condition creating a singularity when the denominator becomes zero. This is a result of implicitly assuming an infinite lifetime for every state involved in Eq. (3.15). In order to avoid this detrimental situation we make the transition $E_x \to E_x + \mathrm{i}\Gamma_x$. Thus, a finite lifetime for each state $|x\rangle$ with the usual definition $\Gamma_x = \hbar/\tau_x$ is being introduced (cf. Ref. [73]).

For the sake of completeness this section will be concluded by writing down the scattering probability for all contributions in Fig. 3.7. For the classical derivation the reader is advised to refer to Ref. [73]. In the following formula a finite lifetime of the states $|1\rangle$

[1] A van Hove singularity is a singularity in the density of states of a solid (cf. Ref. [79]).

and $|2\rangle$ was considered and the ground state was set to zero, i.e. $E_i = 0$.

$$
\begin{aligned}
P_{ph}(\omega_s) = \left(\frac{2\Pi}{\hbar}\right) \Bigg| & \sum_{1,2} \frac{\langle i|\,\mathcal{H}_{eR}(\omega_i)\,|1\rangle\,\langle 1|\,\mathcal{H}_{eL}\,|2\rangle\,\langle 2|\,\mathcal{H}_{eR}(\omega_s)\,|i\rangle}{[\hbar\omega_i - (E_1 + \mathrm{i}\Gamma_1)]\,[\hbar\omega_i - \hbar\omega_0 - (E_2 + \mathrm{i}\Gamma_2)]} + \\
& \sum_{1,2} \frac{\langle i|\,\mathcal{H}_{eR}(\omega_i)\,|1\rangle\,\langle 1|\,\mathcal{H}_{eR}(\omega_s)\,|2\rangle\,\langle 2|\,\mathcal{H}_{eL}\,|i\rangle}{[\hbar\omega_i - (E_1 + \mathrm{i}\Gamma_1)]\,[\hbar\omega_i - \hbar\omega_s - (E_2 + \mathrm{i}\Gamma_2)]} + \\
& \sum_{1,2} \frac{\langle i|\,\mathcal{H}_{eR}(\omega_s)\,|1\rangle\,\langle 1|\,\mathcal{H}_{eL}\,|2\rangle\,\langle 2|\,\mathcal{H}_{eR}(\omega_s)\,|i\rangle}{[-\hbar\omega_s - (E_1 + \mathrm{i}\Gamma_1)]\,[-\hbar\omega_s - \hbar\omega_0 - (E_2 + \mathrm{i}\Gamma_2)]} + \\
& \sum_{1,2} \frac{\langle i|\,\mathcal{H}_{eR}(\omega_s)\,|1\rangle\,\langle 1|\,\mathcal{H}_{eR}(\omega_i)\,|2\rangle\,\langle 2|\,\mathcal{H}_{eL}\,|i\rangle}{[-\hbar\omega_s - (E_1 + \mathrm{i}\Gamma_1)]\,[-\hbar\omega_s + \hbar\omega_i - (E_2 + \mathrm{i}\Gamma_2)]} + \\
& \sum_{1,2} \frac{\langle i|\,\mathcal{H}_{eL}\,|1\rangle\,\langle 1|\,\mathcal{H}_{eR}(\omega_i)\,|2\rangle\,\langle 2|\,\mathcal{H}_{eR}(\omega_s)\,|i\rangle}{[-\hbar\omega_0 - (E_1 + \mathrm{i}\Gamma_1)]\,[-\hbar\omega_0 + \hbar\omega_i - (E_2 + \mathrm{i}\Gamma_2)]} + \\
& \sum_{1,2} \frac{\langle i|\,\mathcal{H}_{eL}\,|1\rangle\,\langle 1|\,\mathcal{H}_{eR}(\omega_s)\,|2\rangle\,\langle 2|\,\mathcal{H}_{eR}(\omega_i)\,|i\rangle}{[-\hbar\omega_0 - (E_1 + \mathrm{i}\Gamma_1)]\,[-\hbar\omega_0 + \hbar\omega_s - (E_2 + \mathrm{i}\Gamma_2)]} \Bigg|^2 \cdot \\
& \cdot \delta\left[\hbar\omega_i - \hbar\omega_0 - \hbar\omega_s\right]
\end{aligned}
\tag{3.17}
$$

For certain energies $\hbar\omega_i$ in Eq. (3.17), $P_{ph}(\omega_s)$ shows a maximum. However, these resonances are dominated by the first sum as both of its denominators become resonant at the same $\hbar\omega_i$. For an excitation energy $\hbar\omega_i$ when no resonance condition is met other sums may have a greater contribution but the overall scattering maximum is being determined by the first term.

3.4 Raman scattering in graphene

3.4.1 Raman modes of graphene

The Raman spectrum of graphene is shown in Fig. 3.8. The G mode, known from graphite at a Raman shift of $1570\,\mathrm{cm}^{-1}$ has E_{2g} symmetry and is polarization independent [80]. It is the result of a single phonon Raman scattering process as described in Sec. 3.2 and Sec. 3.3.

Additionally, we find the D and 2D modes. They show a dispersive behavior as their Raman shift depends on excitation energy. It is caused by the unique electronic band structure of graphene and other materials having sp^2 bonds [81]. The origin of these modes is double resonant Raman scattering [82] which will be described in Sec. 3.4.2. The 2D mode is the overtone of the D mode. Therefore, it shows a dispersion twice as high, $100\,\mathrm{cm}^{-1}/\mathrm{eV}$ instead of $50\,\mathrm{cm}^{-1}/\mathrm{eV}$.

Contrary to the 2D mode, the double resonance process of the D mode involves scattering by a defect. Consequently, the D mode does not appear in defect-free graphene and has

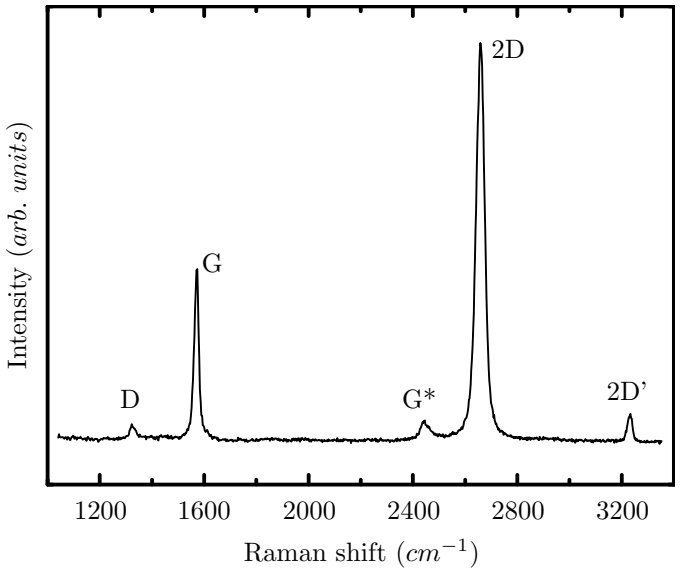

FIGURE 3.8: Raman spectrum of graphene for 532 nm excitation.

an increasing intensity with increasing defect density [82]. The 2D mode is always observable and does not depend on the defect density in the scattering region.

The G* mode originates from a double resonant scattering process involving a TO and a LA phonon. The 2D' mode is also created by double resonant Raman scattering according to Ref. [83] and is the overtone of the D' mode which is not shown in Fig. 3.8.

3.4.2 Double resonant Raman scattering

The easiest Raman mode of graphene to describe theoretically is the G mode, which originates from a conventional one-phonon Raman process as described in Sec. 3.3. The D and 2D modes are described by a double resonant Raman process (cf. Refs. [82, 84, 85]) involving the following steps

1. A photon gets absorbed and an electron-hole pair is being created.
2. The carriers are scattered twice by a phonon with wavevector $\vec{q}$.
3. Radiative recombination and emission of the scattered photon.

This process is the origin of the D, D', 2D and 2D' modes. In the case of the D and D' modes backscattering is caused by a defect. The difference between them is that scattering in case of the D mode happens across the Brillouin zone from K to K' and back (inter-valley scattering). However, scattering for the D' mode occurs at the same K point (intra-valley scattering).

The 2D mode is also caused by double resonant Raman scattering but the backscattering involves a second phonon which is the reason why this mode is always visible, even in totally defect-free graphene. The dispersion of $100\,\mathrm{cm}^{-1}/\mathrm{eV}$ is twice that of the D mode ($50\,\mathrm{cm}^{-1}/\mathrm{eV}$) indicating that it is caused involving the same phonon of the D mode, scattered twice.

Figure 3.9 shows the double resonant Raman process for the D and D' mode and their overtones 2D and 2D'. As mentioned in Sec. 3.1 we find a linear dispersion at the K point, indicated by the blue lines in Fig. 3.9. It is commonly known as Dirac cone and a good assumption for excitation energies in the visible light range and across the Fermi energy [84]. Subsequently, we find a resonant excitation (emission) for every mode described. Thus, graphene is an ideal marker solid as it does not involve intrinsic resonances[2]. In figure 3.9 only the process for a resonant excitation is shown. Resonant emission is also possible and will be treated later in Sec. 3.4.4.

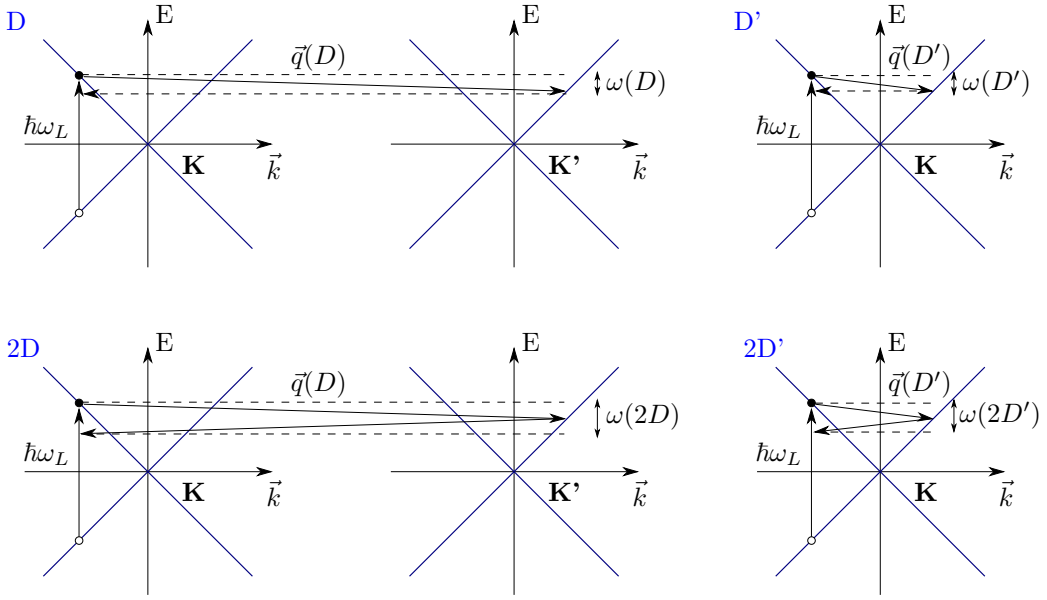

FIGURE 3.9: Double resonance processes occurring in graphene for electron scattering only. The **K** and **K'** points are not equivalent. The D and 2D modes are inter-valley modes meaning the electron-hole pair is scattered from **K** to **K'** and back. The D' and 2D' modes are intra-valley modes so the electron-hole pair does not leave the **K** point.

3.4.3 Effects of strain on the Raman modes of graphene

In the following section we need to abandon the simple assumption of a 1D Dirac cone as recent theoretical investigations show [86–89]. In Fig. 3.10 we find a thorough calculation of the transitions leading to the 2D mode of graphene. From the underlying contours we find that there are different phonon wave vectors possible. Not exclusively along the

[2] A detailed explanation will be given in Sec. 3.4.4

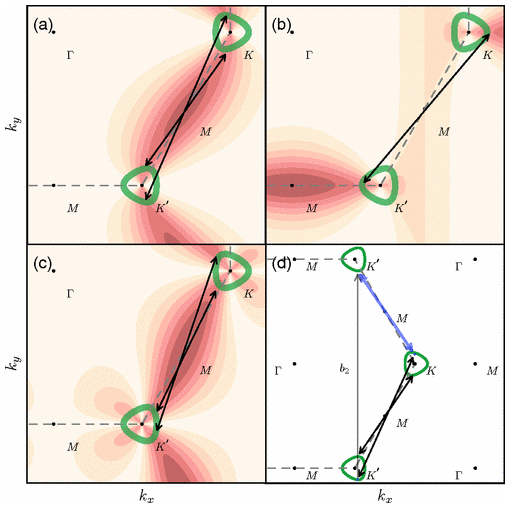

FIGURE 3.10: Phonon mediated electronic transitions in graphene. The black arrows are the transitions resulting in maximum intensity. The red-brown contours in (a)-(c) are the product of optical absorption and emission matrix elements for different orientations: (a) x:x, (b) y:y and (c) x:y. Where x is the zigzag and y is the armchair orientation of graphene. The green lines are the energy contours for fixed laser excitation. (d) shows that the addition of a reciprocal lattice vector $\vec{b}_2$ (gray) to $\vec{k}_i^*$ causes an outer transition (black arrows) to become an inner transition (blue arrows). Taken from Ref. [86].

high symmetry K-M direction. We also observe that the polarization has an influence on the scattering path (cf. Fig. 3.10 (a) and (b)).

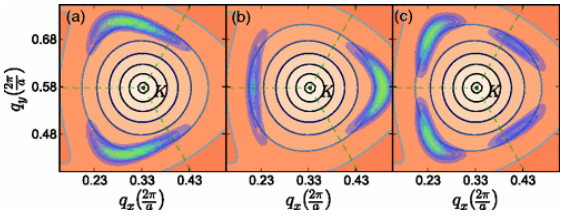

FIGURE 3.11: Dominant phonon wave vectors $\vec{k}_i^*$ for scattering of the 2D mode in unstrained graphene (blue-green regions). The underlying orange contours show the dispersion of the iTO phonon branch. As in Fig. 3.10 the scattering directions are: (a) x:x, (b) y:y and (c) x:y. Taken from Ref. [86].

Figure 3.11 shows the dominant phonon wave vectors for a fixed excitation energy. Depending on the direction of the polarizer and analyzer the angular location of the wavevector $\vec{k}_i^*$ changes (blue-green contours in Fig. 3.11). Initially it was believed that strain results mainly in the shift of the Dirac cones with respect to the strain direction [90–92]. In Ref. [86] it was found that strain also results in a distortion of the trigonal warping effect at the K point (cf. Sec. 3.1). Comparing Fig. 3.11 and Fig. 3.12 we find the effect of strain on the iTO phonon dispersion around the K point. This results in a shift and splitting of the 2D mode, observable in Fig. 3.12 (a-c). In this figure the left-hand mode is called $2D^-$ and the right-hand one $2D^+$. The shift is proportional to the strain as Refs. [86, 90, 93] report. In Ref. [90] the shift rate of a graphene

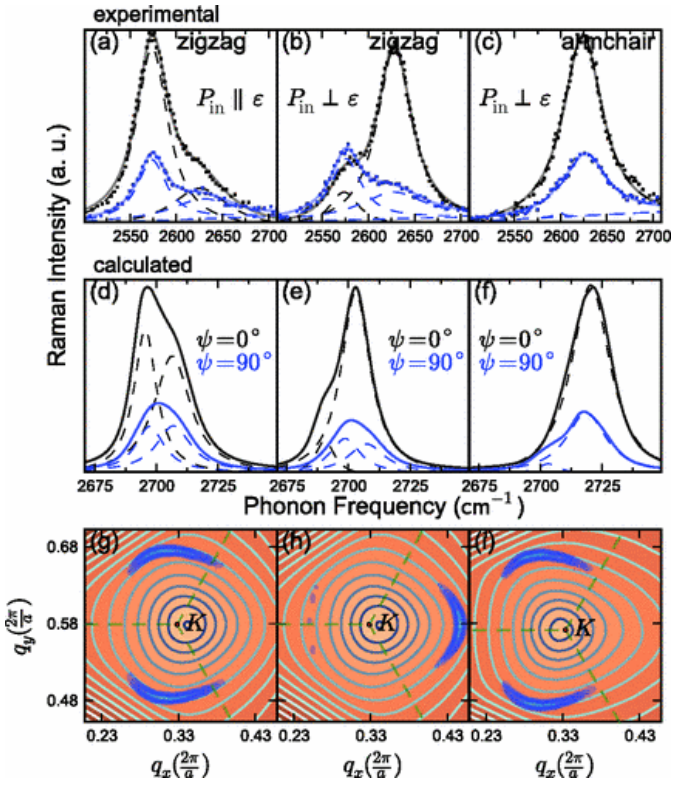

FIGURE 3.12: (a-c) Experimental Raman spectra of strained graphene from Ref. [90]. (d-f) calculated Raman spectra of strained graphene. (g-f) shows dominant phonon wavevectors (blue-green contours) with the iTO phonon dispersion (orange contours). The dominant phonon wavevectors along with the iTO phonon dispersion were calculated for 1.5% strain in the zigzag direction (g,h) and 1.0% in the armchair direction (i). (a,d,g) show spectra for parallel and (b,e,h) for perpendicular polarization with respect to the zigzag orientation of graphene. (c,f,i) show perpendicular polarization to the armchair orientation. Taken from Ref. [86].

sheet supported by Polydimethylsiloxan (PDMS) with 2.6% strain was shown to be 99 cm^{-1}/eV and 106 cm^{-1}/eV for the $2D^-$ and $2D^+$ mode, respectively.

Popov et al. (Ref. [88]) estimate a split into 3 modes, named $2D_1$, $2D_2$ and $2D_3$. They attribute this to the 3 possible scattering paths in the Brillouin zone to the nearest neighbor K points, depending on the strain direction (cf. Fig. 3.1).

The observed shift can be used to measure strain imposed on a graphene sheet. In Fig. 3.13 we find two parameters which are used to quantify strain. The parameter ϵ_{ll} quantifies strain applied along the longitudinal direction of a graphene sheet. The parameter ϵ_{tt} quantifies strain along the transverse direction perpendicular to the longitudinal one. The chiral angle of the graphene sheet is given by Θ.

The strain tensor will be written according to Ref. [94] as

$$\epsilon = \begin{pmatrix} \epsilon_{tt}\cos^2\Theta + \epsilon_{ll}\sin^2\Theta & \frac{1}{2}\sin(2\Theta)(\epsilon_{ll}-\epsilon_{tt}) \\ \frac{1}{2}\sin(2\Theta)(\epsilon_{ll}-\epsilon_{tt}) & \epsilon_{tt}\sin^2\Theta + \epsilon_{ll}\cos^2\Theta \end{pmatrix} \tag{3.18}$$

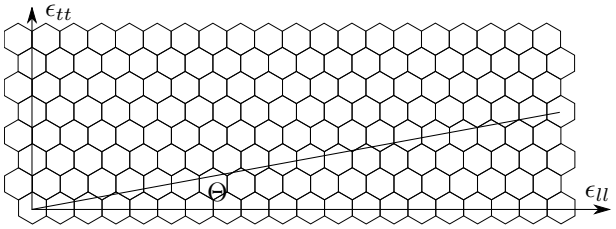

FIGURE 3.13: Parameters ϵ_{ll} and ϵ_{tt} used to quantify strain imposed on a graphene sheet with chiral angle Θ.

We may now write the dynamical equation for the phonon modes in the presence of strain

$$m\ddot{u}_i = -\Bigg(\underbrace{m\omega_0^2 u_i}_{\text{unstrained motion}} + \underbrace{\sum_{klm} K^{(1)}_{ikml}\epsilon_{lm}u_k}_{\text{change due to strain}} \Bigg) \tag{3.19}$$

with u being the displacement of the atoms, m being their mass and ω_0 being the unstrained phonon frequency.

The tensor $K^{(1)}$ has only three nonzero components (cf. Ref. [94]) due to the hexagonal symmetry of the graphene sheet (E_{2g} for Raman active phonons). Thus, we find (cf. Ref. [94])

$$K_{1111} = K_{2222} = m\bar{K}_{11} \tag{3.20a}$$

$$K_{1122} = m\bar{K}_{12} \tag{3.20b}$$

$$K_{1212} = \frac{1}{2}m(\bar{K}_{11} - \bar{K}_{12}). \tag{3.20c}$$

The solutions to Eq. (3.19) are found by inserting Eqns. (3.20) and solving for the eigenvalues. Subsequent insertion of Eq. (3.18) gives

$$\frac{\Delta\omega}{\omega_0} = \underbrace{\frac{\bar{K}_{11}+\bar{K}_{12}}{4\omega_0^2}}_{\gamma}\underbrace{(\epsilon_{ll}+\epsilon_{tt})}_{\epsilon_h} \pm \frac{1}{2}\underbrace{\frac{\bar{K}_{11}-\bar{K}_{12}}{2\omega_0^2}}_{\beta}\underbrace{(\epsilon_{ll}-\epsilon_{tt})}_{\epsilon_s}. \tag{3.21}$$

The Grüneisen parameter γ was introduced. It describes the frequency shift under hydrostatic strain $\epsilon_h = \epsilon_{ll} + \epsilon_{tt}$. Additionally, the shear strain deformation potential β was introduced. It gives rise to the splitting of phonon modes under shear strain $\epsilon_s = \epsilon_{ll} - \epsilon_{tt}$. Equation (3.21) is mostly written in a shorter form, i.e.

$$\Delta\omega = \gamma\omega_0\epsilon_h \pm \frac{1}{2}\beta\omega_0\epsilon_s \tag{3.22}$$

which is also found in Ref. [95].

3.4.4 Double resonance theory of the 2D mode in graphene

In this section we will use the Raman theory presented in Sec. 3.3 and apply it to double resonant Raman scattering of the 2D mode in graphene. The following calculations are based mainly on Refs. [82, 85, 96].

We will use the processes described in Sec. 3.4.2 to elaborate the details of double resonant Raman scattering in graphene. Figure 3.14 uses the same notation as Fig. 3.7 but considers individual scattering paths for the electron and hole involved.

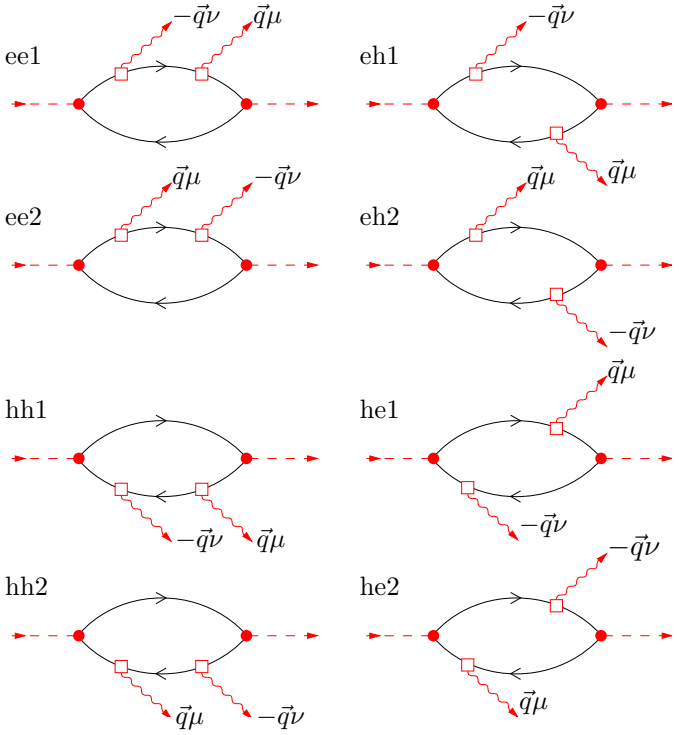

FIGURE 3.14: Feynman diagrams of the processes involved in double resonant Raman scattering of the 2D mode in graphene. It distinguishes scattering electrons (upper path) and holes (lower path) individually. The left-hand side shows scattering involving only one particle: ee1 & ee2 the electron and hh1 & hh2 the hole. On the right-hand side processes involving both particles are shown (eh1, eh2, he1 and he2). After Ref. [85].

The watchful reader might miss the permutation of the vertices as shown in Fig. 3.7. The reason is simple as will be explained by example: considering only electron scattering there are $4! = 12$ possible sequences. From these we will neglect all sequences that involve a time order having the emission of a phonon before (after) absorbing (emitting) a photon since these have a negligible contribution to the scattering probability $P_{ph}(\omega_s)$ due to their denominator (cf. Eq. (3.17)). So we end up having two sequences ee1 and ee2 contributing dominantly to $P_{ph}(\omega_s)$. Using the same argument for hole and combined electron hole scattering, only the sequences shown in Fig. 3.14 remain.

We are able to simplify even farther by considering interference effects. In Ref. [85] Venezuela et. al. found that processes involving only a single particle (ee1, ee2, hh1 and hh2) have a small contribution to $P_{ph}(\omega_s)$. To illustrate this a more general reformulation of Eq. (3.16) will be used. It is based on Ref. [85].

$$I_{\vec{q},\mu,\nu} \propto \left| \sum_{\vec{k},\alpha} K_\alpha(\vec{k},\vec{q},\mu,\nu) \right|^2 \tag{3.23}$$

Here $K_\alpha(\vec{k},\vec{q},\mu,\nu)$ is the contributing term of the respective scattering sequence given below. Before continuing we will complete the reformulation of Eq. (3.16) by giving not only the scattering probability but the intensity of the processes considered. Thus, we need to multiply the scattering probability $P_{ph}(\omega_s)$ with the respective Bose-Einstein statistics. This is done as we implicitly assume thermal equilibrium and the phonons to occupy discrete energy states.

$$I(\omega) \propto \underbrace{\sum_{\vec{q},\mu,\nu} I_{\vec{q},\mu,\nu}\delta(\omega_L - \omega_s - \omega^\nu_{-\vec{q}} - \omega^\mu_{\vec{q}})}_{P_{Ph}(\omega_s)} \cdot [n(\omega^\nu_{-\vec{q}})+1][n(\omega^\mu_{\vec{q}})+1] \tag{3.24}$$

With $n(\omega)$ being the Bose-Einstein statistics. In the formulation above $\hbar = 1$ was set for simplicity reasons. The 2D phonon has a shift of about $2650\,\mathrm{cm}^{-1}$ and therefore an energy of about $\hbar\omega_{\vec{q}} \approx 329\,\mathrm{meV}$, which is much higher than $k_BT \approx 26\,\mathrm{meV}$. So that $n(\omega^{\mu,\nu}_{\vec{q}}) \approx 0$.

Now we need to formulate the scattering terms in order to calculate the intensity. Beginning with the eh1 term from Fig. 3.14. Using the explicit and informative notation from Ref. [85]. $|\vec{k},\pi\rangle$ represents a state with the vector $\vec{k}$ in the Brillouin zone and the energy of the π band. π^* corresponds to the excited state in the Dirac cone (upper branch). The Hamiltonian $\mathcal{H}_{eL}^{-\vec{q},\mu}$ means scattering by a vector $-\vec{q}$ via the phonon of the branch μ.

$$K_{eh1} = \frac{\langle\vec{k}+\vec{q},\pi|\mathcal{H}_{eR}|\vec{k}+\vec{q},\pi^*\rangle\langle\vec{k},\pi|\mathcal{H}_{eL}^{-\vec{q},\mu}|\vec{k}+\vec{q},\pi\rangle\langle\vec{k}+\vec{q},\pi^*|\mathcal{H}_{eL}^{\vec{q},\nu}|\vec{k},\pi^*\rangle\langle\vec{k},\pi^*|\mathcal{H}_{eR}|\vec{k},\pi\rangle}{(E_L-E^{\pi^*}_{\vec{k}+\vec{q}}+E^{\pi}_{\vec{k}+\vec{q}}-\hbar\omega^\nu_{-\vec{q}}-\hbar\omega^\mu_{\vec{q}}-\mathrm{i}\Gamma_3)(E_L-E^{\pi^*}_{\vec{k}+\vec{q}}+E^{\pi}_{\vec{k}}-\hbar\omega^\nu_{-\vec{q}}-\mathrm{i}\Gamma_2)(E_L-E^{\pi^*}_{\vec{k}}+E^{\pi}_{\vec{k}}-\mathrm{i}\Gamma_1)} \tag{3.25}$$

This quite lengthy term will be simplified a lot. In principle we need to calculate each matrix element by using the irreducible representation of its elements and calculate the matrix product. Doing so we end up having the polarization dependence of the term under investigation. To simplify the derivation a fully symmetric scattering condition is being assumed and each matrix element was set to 1. Thus, we end up with the nominator being 1.

Now let us consider the denominator of Eq. (3.25). We find the lifetimes τ_i of the states

involved by $\Gamma_i = 1/\tau_i$. Energies are written as $E^{\pi}_{\vec{k}}$ where $\vec{k}$ gives the point in the Brillouin zone and π the respective band, the particle is scattered to (cf. Fig. 3.9). Considering a Dirac cone as a good approximation for the band structuce of graphene around the K point[3] (cf. Ref. [70] and Sec. 3.1). This is reasonable since Raman scattering takes place near the K point [82, 85]. Additionally, we switch from two dimensions to one dimension since the problem has rotational symmetry to a reasonable degree (cf. Sec. 3.1). Thus, we are now able to rewrite these energies using $E^{\pi^*,\pi}_{\vec{k}} = \pm\hbar v_F|\vec{k}|$ with v_F being the Fermi velocity of graphene. The values used for the calculations are $\hbar v_f = 6.49\,\mathrm{eV}$ and $\gamma = 84\,\mathrm{meV}$ (taken from Ref. [85]). The phonon energy $\hbar\omega^{\mu,\nu}_{\vec{q}}$ is assumed to be the same for every phonon scattered. Having a linear band structure we find the same dispersion for both phonons μ, ν with the same energy. Additionally, it is reasonable to assume that the lifetime of the transitions is equal and we find $\Gamma_1 = \Gamma_2 = \Gamma_3 = \Gamma$.

Inserting these simplifications we find that the scattering processes from Fig. 3.14 are identical for the ee1, ee2, hh1 and hh2 processes. Therefore, we call them K_{aa}. The same happens to the processes involving electrons and holes (eh1, eh2, he1 and he2). Thus, we call them K_{ab} respectively and find

$$\begin{aligned} K_{aa} &= \frac{1}{(E_L - 2\hbar v_F\vec{k} - 2\hbar\omega_{\vec{q}} - \mathrm{i}\Gamma)(E_L - \hbar v_F\vec{q} - \hbar\omega_{\vec{q}} - \mathrm{i}\Gamma)(E_L - 2\hbar v_F\vec{k} - \mathrm{i}\Gamma)} \\ K_{ab} &= \frac{1}{(E_L - 2\hbar v_F(\vec{k} - \vec{q}) - 2\hbar\omega_{\vec{q}} - \mathrm{i}\Gamma)(E_L - \hbar v_F\vec{q} - \hbar\omega_{\vec{q}} - \mathrm{i}\Gamma)(E_L - 2\hbar v_F\vec{k} - \mathrm{i}\Gamma)}. \end{aligned} \tag{3.26}$$

Using Eq. (3.23) we are able to transform the sum into an integral $\int_0^\infty K dk$ as we are dealing with a continuum of states. The intensity $I_{\vec{q}}$ in Eq. (3.23) will be derived using

$$I_{\vec{q}} \propto \left| \int_0^\infty \frac{\theta dk}{(k+\alpha)(k+\beta)} \right|^2 = \left| \theta \frac{\ln\beta - \ln\alpha}{\alpha - \beta} \right|^2. \tag{3.27}$$

Thus, we obtain a general solution applicable to both cases. By using the following convenient substitutions in K_{aa} and K_{ab}

$$\begin{aligned} \theta &= (2\hbar v_F)^{-2}(E_L - \hbar v_F q - \hbar\omega_{\vec{q}} - \mathrm{i}\Gamma)^{-1} \\ \alpha &= \frac{E_L - 2\hbar\omega_{\vec{q}} - \mathrm{i}\Gamma}{2\hbar v_F} \\ \beta &= -\frac{E_L - \mathrm{i}\Gamma}{2\hbar v_F} \end{aligned} \tag{3.28}$$

[3] A more general description may be found using equation (6) in Ref. [66].

we obtain

$$I_q(K_{aa}) = \left| \frac{\theta}{\alpha+\beta} \left[\ln\beta - \ln(-\alpha)\right] \right|^2 \tag{3.29}$$

$$I_q(K_{ab}) = \left| \frac{\theta}{\alpha-\beta-q} \left[\ln\beta - \ln(\alpha-q)\right] \right|^2 . \tag{3.30}$$

In $I_q(K_{aa})$ we see that only θ depends on q and has a resonance condition for

$$q = \frac{E_L - \hbar\omega_{\vec{q}} - \mathrm{i}\Gamma}{\hbar v_F}. \tag{3.31}$$

In $I_q(K_{ab})$ we find that there is a second resonance $\alpha - \beta - q = 0$ which adds up to the same resonance condition as in Eq. (3.31). So we find the same resonance for both K_{aa} and K_{ab} with the latter being the dominant contribution due to two terms becoming resonant at the same time. The logarithmic part in Eq. (3.30) is a slow varying function of q and therefore does not alter the resonance condition. The contribution from K_{aa} and K_{ab} to the intensity is shown in Fig. 3.15 using Eqns. (3.29) and (3.30). We find that K_{aa} has a negligible intensity compared to K_{ab}. Thus, K_{aa} will be neglected in further derivations.

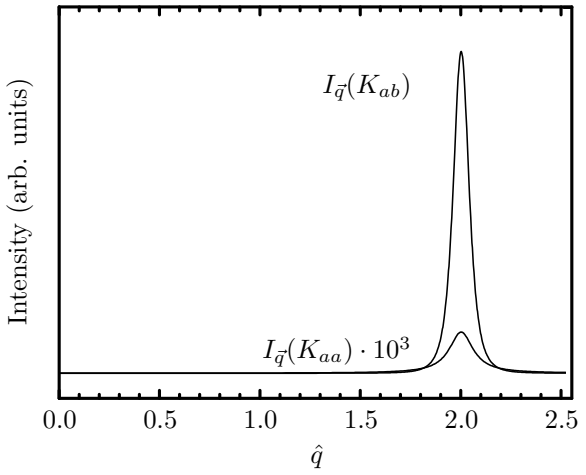

FIGURE 3.15: Numerical calculation of the contribution from Eqns. (3.29) and (3.30) to the intensity. $\hat{q} = 2q\hbar v_f/E_L$ is the normalized momentum $\vec{q}$. Therefore $\hat{q} = 2$ corresponds to a two phonon resonance.

The last but most important point to learn from the calculations above is the energy dependence of the intensity of the 2D mode. Figure 3.16 shows the calculated intensity using Eq. (3.24). The decline should not be mixed up with the normal ω^4 increase in intensity for Raman scattering (cf. Ref. [73]). It is caused by the broadening parameter γ which was kept constant in the calculations (cf. Ref. [85]). In Fig. 3.16 no resonance features are present. Thus, we should not see any enhancement effects originating from

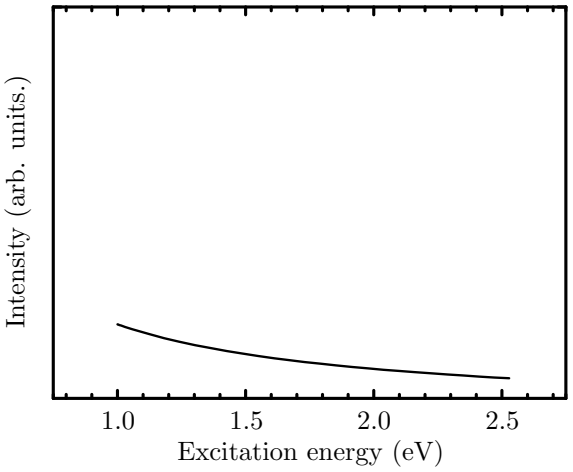

FIGURE 3.16: Calculated intensity of the 2D Mode of graphene using Eq. (3.24). The decline is not the expected ω^4 dependence of the intensity of an arbitrary Raman process on excitation energy. It is caused by a constant broadening parameter γ. No intrinsic resonance is observable.

the graphene itself. This is the reason why graphene was chosen as an analyte in the first place.

3.5 Plasmon-enhanced resonance Raman theory

After analyzing the properties of the standard double resonant Raman process in the preceding section, it is now time to extend our treatment and incorporate a plasmonic antenna into the system. Since we do not know the coupling mechanism between gold and graphene, a general approach will be used, not specifying the details of the microscopic coupling effect. In order to determine the details of the coupling, further experiments need to be conducted.

In Sec. 3.4.4 we deduced that only the scattering term K_{ab} of Eq. (3.26) has a major contribution to the total scattering intensity. Hence, only this Term will be used in the further treatment. Figure 3.17 shows the eh1 process of Fig. 3.14 as a representation for all scattering processes possible (indicated by the dashed frame). The scattering processes are once again shown using Feynman diagrams. We end up having four possible cases in which the gold antenna is either interacting with the incoming and outgoing photon, only the incoming photon, only the outgoing one or none.

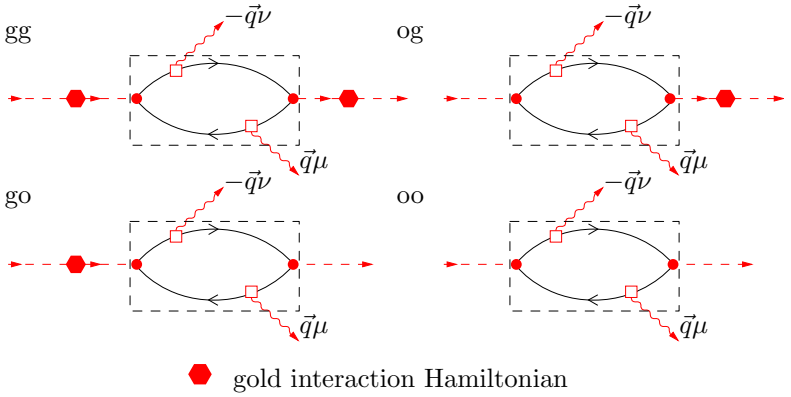

FIGURE 3.17: Feynman diagrams of the processes involved in surface-enhanced Raman scattering. The diagrams are named according to the interaction between gold and graphene. "gg" means interaction of the incoming and outgoing photons with gold, "go" only for incoming interaction, "og" only for outgoing and "oo" for no interaction resulting in the scattering term K_{ab} from Sec. 3.4.4. The dashed box means all the processes of Fig. 3.14 need to be inserted. Thus, every diagram represents four scattering events. The interaction Hamiltonian of gold and graphene is represented by a red hexagon.

Before writing down the scattering terms it is useful to define the incoming and outgoing contribution of the gold antenna using Eq. (3.15)

$$\Lambda_{in} = \frac{\langle \varphi_{in,2} | \mathcal{H}_{Au} | \varphi_{in,1} \rangle}{E_L - E_{Au} - \mathrm{i}\Gamma_{Au}} = \frac{\kappa}{E_L - E_{Au} - \mathrm{i}\Gamma_{Au}} \tag{3.32a}$$

$$\Lambda_{out} = \frac{\langle \varphi_{out,2} | \mathcal{H}_{Au} | \varphi_{out,1} \rangle}{E_L - E_{Au} - 2\hbar\omega_{\vec{q}} - \mathrm{i}\Gamma_{Au}} = \frac{\kappa}{E_L - E_{Au} - 2\hbar\omega_{\vec{q}} - \mathrm{i}\Gamma_{Au}}. \tag{3.32b}$$

A fully symmetric gold interaction Hamiltonian is being assumed as the precise mechanism of the gold interaction is not known. Thus, only a constant contribution κ from the matrix elements of the gold Hamiltonian is left. The overall scattering intensity is different for gold and graphene.

The scattering terms will now be rewritten as

$$K_{gg} = \Lambda_{in} \cdot K_{ab} \cdot \Lambda_{out} \tag{3.33a}$$

$$K_{og} = K_{ab} \cdot \Lambda_{out} \tag{3.33b}$$

$$K_{go} = \Lambda_{in} \cdot K_{ab} \tag{3.33c}$$

$$K_{oo} = K_{ab}. \tag{3.33d}$$

E_{Au} represents the extinction maximum of the plasmon and Γ_{Au} its width. Λ_{in} is the amplification term for the incoming radiation and Λ_{out} the term for the emitted radiation. Using Eqns. (3.23) and (3.33) we are now able to calculate the resonance behavior of the system graphene on gold.

In Fig. 3.18 the scattering intensity obtained using Eqns. (3.33) is shown for different

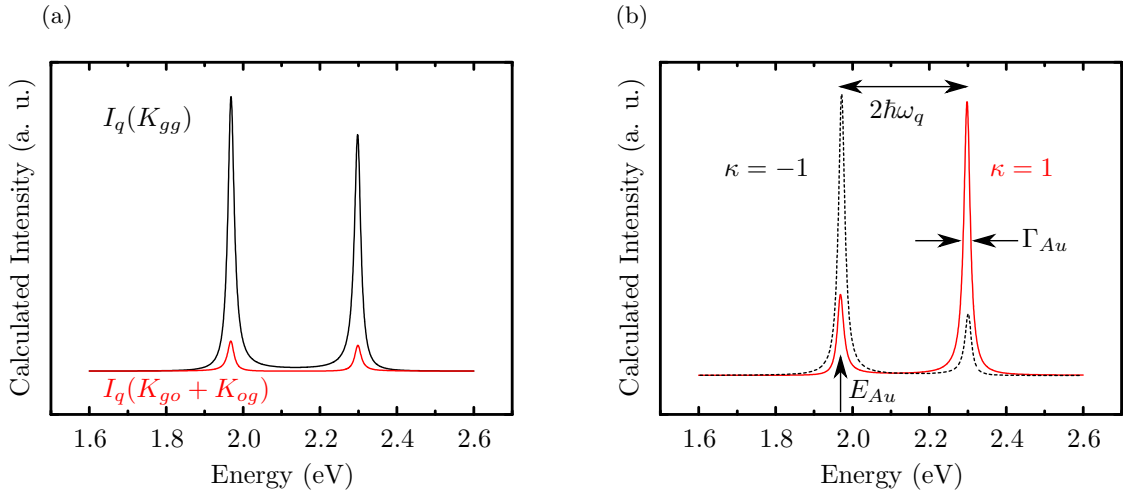

FIGURE 3.18: Calculated intensity using Eq. (3.33) for E_{Au}= 1.97 eV, Γ_{Au}= 0.01 eV and $\hbar\omega_q$= 165 meV for different scattering contributions. (a) shows the intensity considering only the K_{gg} and $K_{go}+K_{og}$ terms. (b) shows the intensity considering all terms and shows the influence of the variables E_{Au}, Γ_{Au}, $2\hbar\omega_q$ and κ. The intensity scale is equal in (a) and (b).

cases. Figure 3.18 (a) shows the enhancement considering ingoing and outgoing gold antenna interaction during one scattering event in the black curve (K_{gg}). The ingoing and outgoing gold antenna interaction was considered separately within one scattering event in the red curve ($K_{go}+K_{og}$). For all scattering events $\kappa = 1$ was assumed. We find the amplification of the combined term (K_{gg}) being one order of magnitude larger.

Considering all terms (Fig. 3.18 (b)) we observe that the amplitude of the ingoing and outgoing resonance depends on κ. For $\kappa > 0$ the outgoing resonance at $E_{Au}+2\hbar\omega_q$ becomes dominant. For $\kappa < 0$ the ingoing resonance at E_{Au} becomes dominant.

The intensity of the SERS amplification does not depend on K_{ab} in the end. It is a slowly varying function in excitation energy and does not show any resonances (cf. Fig. 3.16). Therefore, it does not alter the shape of the scattering intensity. Thus, we are able to obtain an analytic expression for the intensity of the SERS process.

$$\begin{aligned} I_{SERS} &= \int_0^\infty \int_0^\infty |K_{gg}+K_{go}+K_{og}+K_{oo}|^2 dk\ dq \\ &= |\Lambda_{in}\Lambda_{out}+\Lambda_{in}+\Lambda_{out}+1|^2 \int_0^\infty \int_0^\infty |K_{ab}|^2 dk\ dq \end{aligned} \tag{3.34}$$

Simplifying $\int\int |K_{ab}|^2 dkdq \approx C$ is possible since K_{ab} is a slowly varying function in k and q. Thus, we obtain a simple analytical solution

$$I_{SERS} \approx C \cdot |\Lambda_{in}\Lambda_{out}+\Lambda_{in}+\Lambda_{out}+1|^2. \tag{3.35}$$

Inserting Eqns. (3.32) we find

$$I_{SERS} \approx C \cdot \frac{[(E_L - E_{Au} + \kappa)^2 + \Gamma_{Au}^2)][(E_L - E_{Au} - 2\hbar\omega_q + \kappa)^2 + \Gamma_{Au}^2]}{[(E_L - E_{Au})^2 + \Gamma_{Au}^2][(E_L - E_{Au} - 2\hbar\omega_q)^2 + \Gamma_{Au}^2]}. \tag{3.36}$$

This gives us insight into the properties of the SERS amplification. As already shown in Fig. 3.18 (b), we find two resonances, one at E_{Au} and one at $E_{Au} + 2\hbar\omega_q$, both having the width Γ_{Au}. The amplitude of these resonances is determined by interference of the term $(E_L - E_{Au} + \kappa)$ and $(E_L - E_{Au} - 2\hbar\omega_q + \kappa)$ in the nominator. Thus, we get a quadratic increase in the difference of the amplitudes of the resonances over the excitation energy. For higher phonon energies $\hbar\omega_q$ the overall intensity decreases, caused by the denominator. The ratio between the incoming resonance I_{in} and the outgoing resonance I_{out} for constant κ increases according to $I_{in}/I_{out} \propto (2\hbar\omega_q)^2$.

Summing up the previous findings we discovered that the gold antennas create two resonance conditions, amplifying the 2D mode of graphene. These resonances are purely caused by the gold antennas and do not originate from the graphene but from the interplay of the graphene with the gold antennas. We have four parameters that determine the resonance properties of the graphene gold system: E_{Au}, which is assumed to correspond to the near field scattering maximum of the gold antennas, $\hbar\omega_q$ which is the energy of the phonon involved, $\Gamma_{Au} = 1/\tau_{Au}$ is the lifetime of the plasmonic state created and κ is the strength of the coupling of the Raman process to the plasmonic antenna. Thus, κ determines the strength of the amplification and the intensity ratio between ingoing and outgoing resonance.

It needs to be emphasized that the overall amplification $I_{out} + I_{in}$ and the intensity ratio I_{out}/I_{in} depend strongly on the phonon energy $\hbar\omega_q$ and on κ. Additionally, we find that the full width at half maximum (FWHM) of the resonances is solely defined by Γ_{AU}.

In retrospective, choosing graphene as an analyte was a very good choice as it has no intrinsic resonances. Assuming we had chosen an analyte having intrinsic resonances Eq. (3.34) would result in a complicated resonance behavior making it difficult to separate the contributions from the antenna and the analyte. By choosing graphene we end up having only the contribution from the antenna, enabling us to probe only the antenna.

Chapter 4

Experimental methods

4.1 Dark field spectroscopy

In order to measure the plasmonic properties of the dimer antennas involved a dark field spectrometer was built. In dark field spectroscopy a sample area is illuminated at an oblique angle so that only scattered light will be collected by the objective.

The beam path is illustrated in Fig. 4.1. A commercially available dark field microscope

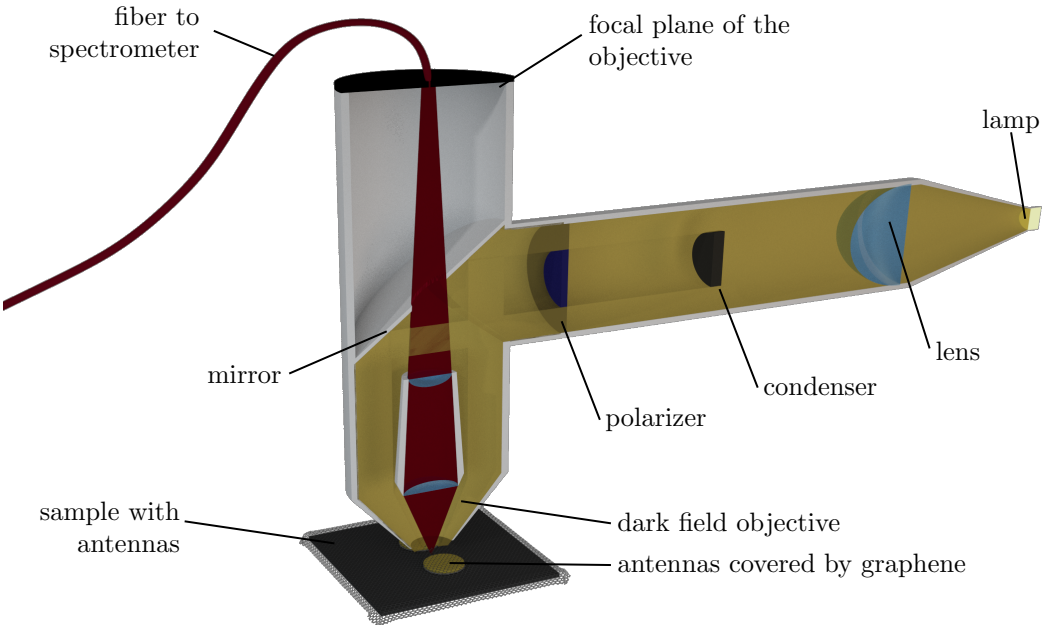

FIGURE 4.1: Design of a dark field spectrometer. Unpolarized light from a standard microscopy lamp illuminates the sample surface. Only the scattered light (dark-red) is collected by the dark field objective. In the focal plane of the objective a small fraction of the area is collected by a fiber and analyzed by the spectrometer.

(Nikon LV100ND) was extended using a Horiba iHr 320 monochromator with a back-thinned silicon CCD detector. The microscope was already equipped with a dark field condenser (as shown in Fig. 4.1) that only allowed an outer ring of the illuminating light to pass the objective. Additionally, the incident light was polarized using a polarizer in the illumination beam path.

As backscattering illumination was used, special dark field objectives were required. These objectives have an outer shell guiding the illuminating light at an oblique angle to the surface. Thus, it will not be collected by the objective under normal reflection. Figure 4.2 shows the scattering path in higher detail. A scatterer situated under the

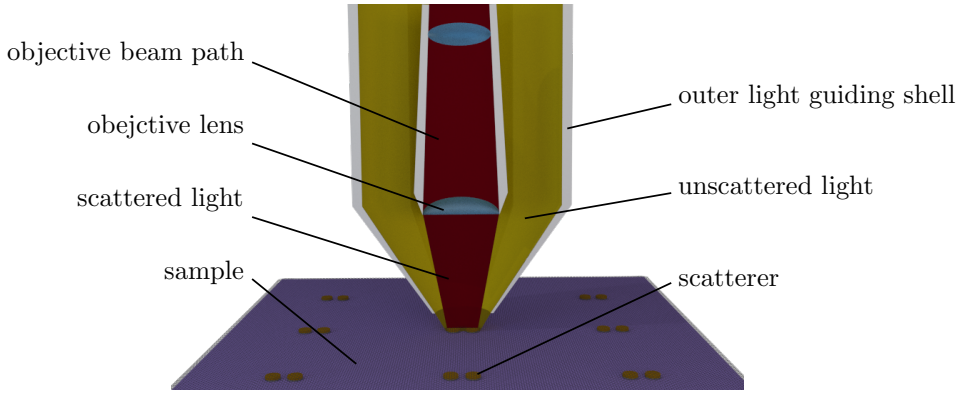

FIGURE 4.2: Principle of dark field microscopy in backscattering geometry. The yellow beam represents light incident by a standard microscope lamp. The red beam represents the scattered light coming from the scatterers on the surface.

objective will scatter the light uniformly to all solid angles. Thus, only scattered light enters the objective and will be imaged to the focal plane of the objective shown in Fig. 4.1. In this plane a small surface area is being collected by a fiber. The collected light is transmitted to a Horiba iHr 320 spectro monochromator equipped with a back thinned CCD. The intensity of the scattered light is extremely weak, requiring a very sensitive detector, a strong light source, or ideally both.

4.2 Raman spectroscopy

A Horiba Scientific XploRA Raman system was used for Raman mapping measurements where the laser was scanned over the surface, recording a spectrum for each point. The XploRA is a single grating notch filter system equipped with 514 nm, 638 nm and 785 nm laser lines. The notch filter rejects Rayleigh scattered light while transmitting Raman scattered light. Due to the usage of only one grating and the adaptation of all optical coatings to the wavelengths used, the XploRA has an about 130 times higher sensitivity than the T64000 system described below. Thus, this system was used to record the

spectra of the antenna samples before doing wavelength-scanned measurements and to conduct Raman mappings.

In order to carry out the wavelength-scanned Raman measurements a Horiba Scientific T64000 Raman system was used. The system is designed as a triple monochromator system having two gratings to spatially split up the incoming light and block the Rayleigh scattered light. It was used in subtractive mode for higher signal intensities.

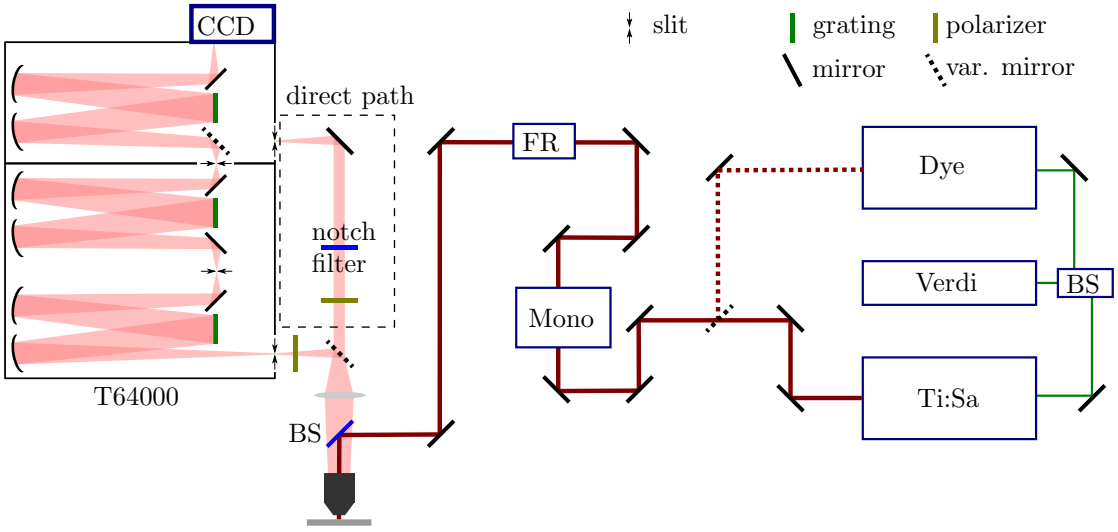

FIGURE 4.3: Experimental setup of the T64000 triple monochromator Raman spectrometer. The major optical elements are shown, including beamsplitters (BS), Fresnel rhomb (FR) and the premonochromator (Mono).

The Raman setup had two lasers available, a Coherent MBR-110 actively stabilized Ti:Al_2O_3 ring cavity laser with an available wavelength range of 690 nm - 1050 nm and an output power of up to 4 W CW[1]. The second laser was a Radiant Dyes passively stabilized dye ring cavity laser with DCM and R6G dyes available. Thus, it covered the wavelength range of 570 nm - 690 nm CW. Both lasers were pumped by a Verdi-V18 532 nm CW laser individually switchable by a polarizing beamsplitter as shown in Fig. 4.3.

The laser beams pass a premonochromator, filtering weak luminescence exiting the laser cavity of the systems. Afterwards, the laser beam polarization was adjusted using a Fresnel rhomb. The polarization component of the Raman scattered light was selected via the polarizers before entering the spectrometer.

The original setup of the T64000 was as triple monochromator in subtractive mode. However, due to weak signal intensity the direct path option was utilized. Bypassing the two monochromator gratings shown in the lower half of the T64000 sketch (Fig. 4.3), the sensitivity was increased by roughly an order of magnitude. Thus, Rayleigh

[1]CW - continuous wave operation

scattered light was suppressed using long pass edge filters (Semrock Razor edge) with an optical density (OD) of 7 in the rejection region. The Raman scattered light was spectrally decomposed using a 900 l/mm grating and detected by a peltier cooled back thinned silicon CCD (Horiba Synapse).

Due to the high spatial confinement of the SERS hotspot a PI P-562.3CD piezoelectric scanning stage with a repeatability of 1 nm in x-, y- and z-direction was used for all measurements. The spectra were acquired using an Olympus 100x objective with a numerical aperture (NA) of 0.9. Thus, an area with a diameter of about 950 nm (at 700 nm)[2] was illuminated.

As plasmonic antennas expose the analyte to very high EM fields, the power of the laser, incident onto the surface of the sample was kept below 300 µW and the sample was held under constant N_2 flow to prevent surface oxidation.

In order to calibrate the sensitivity of the spectrometer usually the samples are put onto a CaF_2 substrate to measure the wavelength-independent 322 cm^{-1} mode simultaneously as a gauge standard. This could not be done as the deposition of a graphene flake required the usage of a SiO_2 covered Si substrate for adhesion and to be able to see the graphene flake[3]. Thus, the calibration curve was recorded in a separate measurement using the 1330 cm^{-1} Raman mode of diamond. This Raman mode is independent of excitation energy and polarization. Fig. 4.4 shows the sensitivity of the T64000 for s- and p-polarizations, respectively. The calibration curve in Fig. 4.4 was used to measure antenna 290 nm-2[4] with the T64000 in triple monochromator mode. All other antennas were measured using the direct path option and filters. The filters produced spectrally sharp absorption features, requiring the usage of a standard spectral calibration lamp (Thorlabs SLS201 stabilized Tungsten-Halogen light source). Thus, the calibration curve could be acquired with high spectral density. Additionally, it was necessary to acquire a calibration curve for each filter used as they had different transmission values and absorption peaks at various wavelengths. Figure 4.5 shows exemplary calibration curves for the 633 nm and the 715 nm filter. They were obtained by dividing the acquired spectrum through the lamp spectrum and division by ω^3 to account for the excitation energy dependence of Raman scattering. The absorption peaks are observable as small bumps in the curve.

All wavelength-scanned Raman measurements were corrected by a calibration curve to eliminate the wavelength dependence of the spectrometer and optical elements used. The Raman shift of all spectra (including the laser line) was calibrated using the lines

[2] Calculated using the diameter of the Airy disc $d = 1.22\lambda/NA$ (cf. Ref. [97])

[3] Due to its weak absorption graphene is only observable by constructive interference occurring at a 300 nm thick SiO_2 layer with a back reflector like Si (cf. Ref. [98]).

[4] Please refer to Sec. 5.3 for the naming convention of the dimer antennas used.

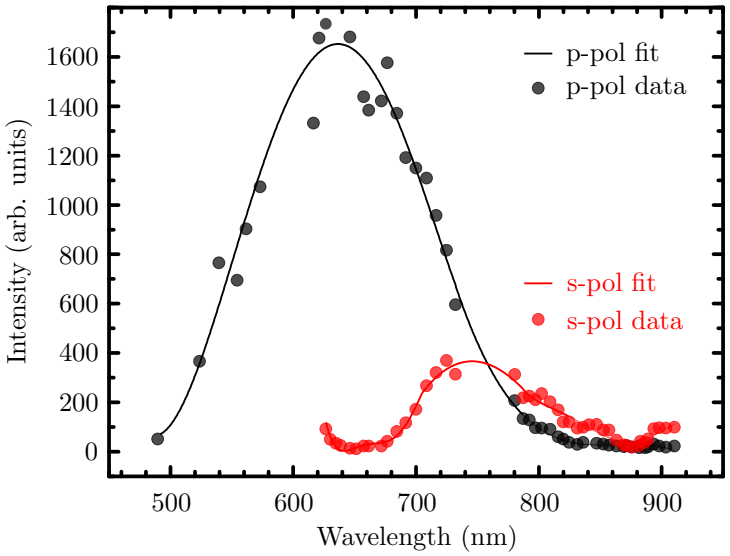

FIGURE 4.4: Calibration curve measured using the 1330 cm^{-1} Raman mode of diamond for s- and p-polarization including fits. Experimental data around 750 nm could not be acquired due to the measurement setup.

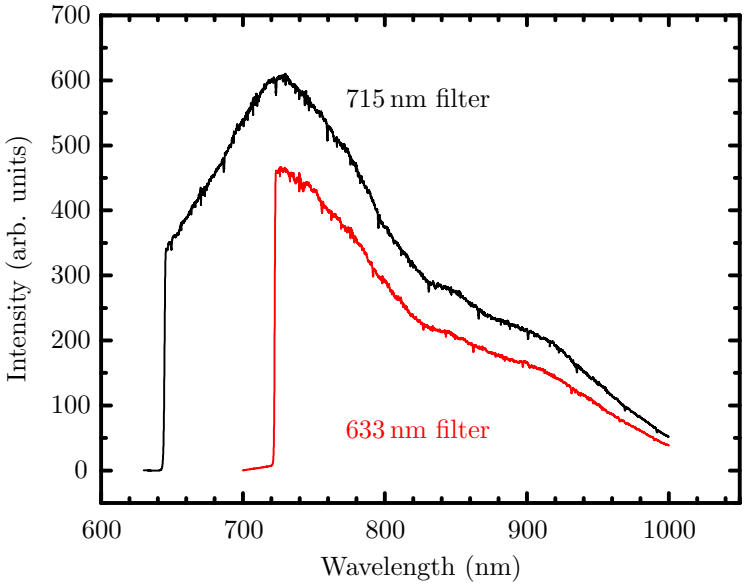

FIGURE 4.5: Calibration curves measured for the 715 nm and 633 nm filters using a Tungsten-Halogen light source for p-polarization.

of a Ne lamp. To obtain comparable intensities the spectra were divided by the respective calibration curve and laser power. Finally, they were fitted using a model with three Lorentzian peaks and a linear background. For wavelength-scanned Raman measurements, the areas of the Lorentzian peaks were added together when necessary. Additionally, the position of each peak was extracted from the fitting parameters and used to calculate the dispersion.

4.3 Sample design

4.3.1 Nanosphere lithography samples

Nanosphere lithography (NSL) is a well established technique to create plasmonic surfaces. A self-assembled layer of hexagonally close packed nanospheres was deposited on top of a substrate. Subsequent metal evaporation created a triangular structure as the spheres did not cover small triangular areas. Finally, the spheres were removed by decomposing them in a solvent. The resulting antennas are shown in Fig. 4.6. The remaining round shape of the nanospheres is still observable. A detailed description of the technique may be found in Ref. [99]. The plasmonic properties are described in Ref. [25] and Sec. 2.3.6. Comparing the triangular antennas in Fig. 4.6 we find a high

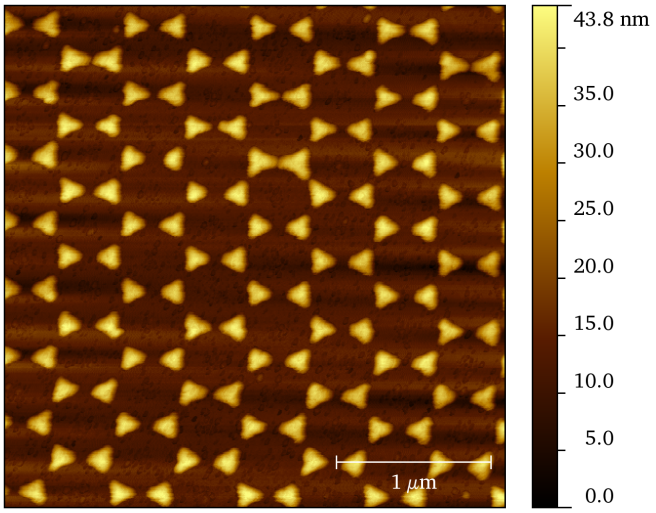

FIGURE 4.6: AFM topography of the antennas obtained by nanosphere lithography.

variation of the triangular shape of the single antennas, resulting in a broad plasmonic resonance, shown in Fig. 5.2. The average length of the triangles is 106 nm and the average height is 110 nm with a thickness of 20 nm[5].

Graphene was prepared by mechanical cleavage and transferred to the structure. Additionally, the antennas were removed from a small area. Thus, it was possible to compare the signal intensities for graphene lying on areas with and without antennas.

4.3.2 Dimer antenna samples

The samples under investigation consist of a silicon wafer covered by 290 nm of SiO_2 grown using plasma enhanced chemical vapor deposition (PECVD). Plasmonic antennas

[5]See Fig. 2.24 (a) for the definition of the triangle length and height.

made of gold were deposited using electron beam lithography. They are cylindrical dimer antennas with a diameter of ≈ 100 nm, a gap spacing of ≈ 30 nm and a height of ≈ 30 nm (cf. Figs. 4.7 (b) & 4.8 (a)). Each antenna is slightly different due to deposition inhomogeneities inherent to the electron beam lithography process. After antenna deposition, graphene was prepared by mechanical cleavage and transferred onto the structure. Due to adhesion, graphene was pulled to the SiO_2 surface, resulting in strained graphene in the vicinity of the antennas and inside of the gap between them.

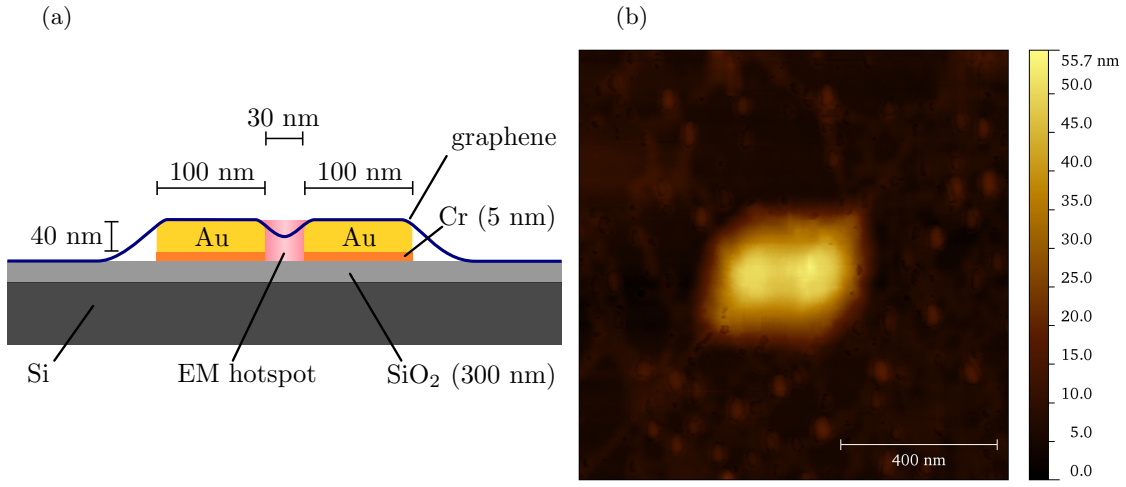

FIGURE 4.7: Structure of the dimer antennas with graphene lying on top of them. Scattering cross section (a) and AFM topography image showing the top of the dimer antenna (b).

Reference [26] estimated the strain acting on the graphene being pulled inside of the cavity. They found the hydrostatic strain component to be ≈ 0.8% and the shear strain to be < 0.4%[6]. Figure 4.7 (a) depicts a cross section of the system under investigation. Figure 4.8 (a) shows a trace across the center of a dimer antenna in horizontal direction. The trace shows that the graphene sheet is being pulled into the gap in between the antennas.

According to Fig. 4.7 (b) it seems to be obvious to use height traces of the antenna to estimate the strain from AFM topography images. This approach has been tried in Ref. [26] but resulted in a systematic overestimation of the strain, explainable by the deposition process. When a graphene flake is transferred to the substrate supported by polymethyl methacrylate (PMMA), it is able to bend and relax during deposition. Additionally, graphene forms ripples and wrinkles when suspended and when being deposited on a surface [100]. Thus, graphene has an intrinsic mechanism of strain relaxation making this approach of strain measurement not feasible.

[6]Please refer to Sec. 3.4.3 for definitions.

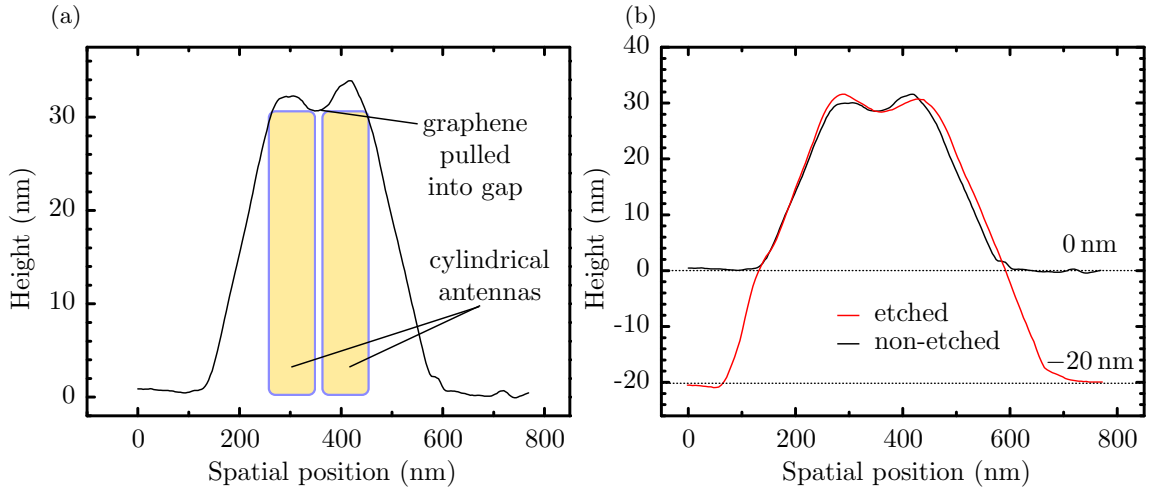

FIGURE 4.8: AFM traces across the center of dimer antennas covered by graphene. (a) AFM trace including the dimer antennas (yellow rectangles) spanning the graphene sheet. (b) AFM trace of antennas covered by graphene showing the height difference between an etched and a non-etched SiO_2 layer.

Two samples with identical antennas were produced. However, one of them was etched to reduce the SiO_2 layer thickness before graphene deposition. This was done in order to change the plasmonic resonance of the dimer antennas on this sample. The height difference is observable in Fig. 4.8 (b) and yields to 20 nm. As the antennas did not react to the etchant only the SiO_2 layer was etched. Therefore, the height of the antennas remained constant with the height difference to the surrounding SiO_2 surface becoming larger.

Chapter 5

Raman measurements

This chapter presents the findings from Raman measurements of a NSL substrate and dimer antennas, both covered with graphene. Dark field spectroscopy was used to determine the plasmonic properties of the structure under investigation. It will be used to show that NSL samples and dimer antennas have a signal enhancement coinciding roughly with the spectral region of the active plasmon measured in the far field. It will also be shown that dark field spectroscopy is capable of measuring the coupled plasmon mode probed later in wavelength-scanned Raman measurements.

The consecutive sections will introduce findings of plasmonic enhancement of the Raman signal caused by NSL surfaces and dimer antennas. These measurements will be analyzed using the theory elaborated in Sec. 2.4 and Sec. 3.5.

5.1 Dark field spectroscopy

Experimental details of a dark field spectrometer were described in Sec. 4.1. This section will give details on how to calculate dark field spectra and correct them for the spectrum of the illuminating lamp.

As described above, plasmonic antennas emit light uniformly into all spatial directions. As the antennas are situated on a substrate the acquired spectra include contributions from several origins:

1. The lamp spectrum reflected by surface corrugations.
2. Scattering from the surface by roughnesses or scatterers (dirt, etc.).
3. Scattering from the scatterers under investigation.

4. Stray light from the environment.

5. The transfer function of the optical elements used.

Point 4 will be eliminated by the subtraction of a dark spectrum (i.e. a spectrum without illumination). The other points need to be removed by taking reference spectra. In order to see this the different contributions to the intensity are expressed in the following way

$$\begin{aligned} I_{surf}(\lambda) &= S_{surf}(\lambda) I_0(\lambda) && \text{intensity from the surface} \\ I_{ant}(\lambda) &= S_{ant}(\lambda) I_0(\lambda) && \text{intensity from the antennas} \\ I_{0,R}(\lambda) &= R(\lambda) I_0(\lambda) && \text{reference of the lamp spectrum.} \end{aligned}$$

$S_{surf,ant}(\lambda) \in [0,1]$ is the wavelength-dependent scattering amplitude of the respective scatterer. It represents the amount of light being scattered at all angles collected by the objective. $I_0(\lambda)$ is the spectrum of the light source being used for illumination. $I_{0,R}(\lambda)$ is the lamp spectrum collected by the objective obtained using an ideal scatterer, thus $R(\lambda) = 1$ for an ideal scattering reference. For a non-ideal scattering reference $R(\lambda) \in [0,1]$ it is similar to the scattering amplitude $S_{surf,ant}(\lambda)$.

When a signal I_R on an area with plasmonic antennas and a signal I_R^0 on an area without plasmonic antennas are collected by the dark field objective they contain the following contributions

$$\begin{aligned} I_R &= I_{surf} + I_{ant} = (S_{surf} + S_{ant}) I_0 \\ I_R^0 &= I_{surf}^0 = S_{surf}^0 I_0. \end{aligned}$$

In order to obtain only the scattering amplitude $S_{ant}(\lambda)$ we use the following formula. By which we are removing all influences on the spectrum except the ones from the scatterer of interest. Assuming $S_{surf} \approx S_{surf}^0$ we obtain

$$\frac{I_R - I_R^0}{I_{0,R}} = \frac{(S_{surf} - S_{surf}^0 + S_{ant}) I_0}{R I_0} \approx \frac{S_{ant}(\lambda)}{R(\lambda)} \tag{5.1}$$

Using Eq. (5.1) we are able to calculate the scattering amplitude of the antenna(s) under investigation. In order to do so the assumption $S_{surf} \approx S_{surf}^0$ needs to be valid. This will be ensured, using a reference spectrum I_R^0 from the surface next to the antennas. In practice this is tricky as surface corrugations or other scatterers might not be visible but contribute significantly to S_{surf}^0. Therefore, it is advisable to take and compare several reference spectra from different areas. Additionally, a polished Polytetrafluorethylen

(PTFE)[1] sample was used as an ideal reference for $I_{0,R}$ because of its uniform reflectivity in the visible, thus $R(\lambda) = 1$ is justifiable to a reasonable extend.

Let us consider having two antennas at a distance where they form a coupled plasmon mode when being illuminated by light along their axis. Using linear polarized light we are able to measure the contribution of the coupled plasmon (cf. Sec. 2.3.2.2). As there is no excitation of the coupled plasmon mode I_{cp} for perpendicular illumination (cf. Refs. [5, 9] and sec. 2.3.4) we will write the contributions for each polarization as

$$I_R^{\parallel} = 2I_{ant} + I_{cp} + I_{surf}$$
$$I_R^{\perp} = 2I_{ant} + I_{surf}.$$

Using Eq. (5.1) we will calculate the scattering efficiency of the coupled plasmon S_{cp}

$$\frac{I_R^{\parallel} - I_R^{\perp}}{I_{0,R}} = \frac{S_{cp}(\lambda)}{R(\lambda)}. \tag{5.2}$$

The antennas described in Sec. 4.3.1 and Sec. 4.3.2 were investigated. The spectra were analyzed using Eqns. (5.1) and (5.2). Figure 5.1 shows the resulting spectra. The perpendicular case equals twice the extinction spectrum of the cylindrical antennas

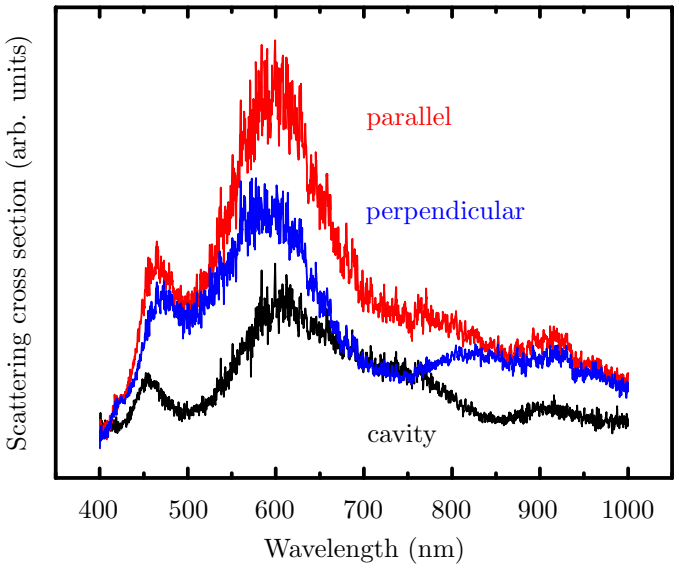

FIGURE 5.1: Dark field spectra of a dimer antenna acquired using the setup described in Sec. 4.1

(cf. Sec. 2.3.4). The parallel case additionally includes the contribution from the coupled plasmon. We see the dipole resonance around 600 nm. The peak around 460 nm originates from the scattering reference and is not a plasmonic mode. Reference [101] investigated a similar case calculating the extinction spectra for spherical particles using

[1] also known as Teflon

FEM in 2D. The results are comparable, considering the smaller diameter and smaller gap used in Ref. [101]. Reference [26] calculated the polarization dependence for the dipole mode and obtained similar results including broadening of the dipole mode in parallel polarization.

5.2 Raman measurements on a hexagonal antenna array

A NSL substrate with graphene deposited on its surface (cf. Sec. 4.3.1) was used for the measurements in this section. Figure 5.2 shows dark field scattering spectra of the NSL

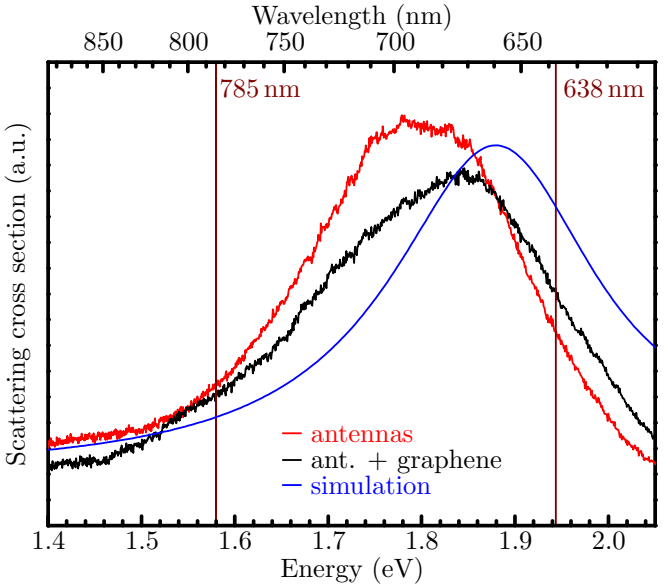

FIGURE 5.2: Comparison of a dark field scattering spectrum of the NSL surface (red curve) and the NSL surface covered with graphene (black curve). A simulated spectrum of the uncovered NSL surface is shown in the blue curve. The available laser wavelengths for excitation are indicated by brown bars. 532 nm is not visible as it is outside of the region plotted.

surface with and without graphene on top. A simulation of the dark field response of the antennas is shown by the blue curve. Without graphene the scattering maximum is at 1.80 eV (690 nm). With graphene on top, the maximum is shifted to 1.85 eV (670 nm). This is a result of the graphene changing the dielectric environment of the antennas (cf. Sec. 2.3.3). The simulation is blue shifted by 30 nm and is therefore still in good agreement with the dark field measurement shown in the red curve. Deviations are likely caused by uncertainties in the dimensions of the antennas and the chromium layer that was not included in the simulation.

Figure 5.3 (a) shows the surface area investigated using Raman mapping by three laser lines (532 nm, 638 nm and 785 nm). The entire area is covered by a graphene sheet. Several different areas are observable in the optical image. On the green surface in

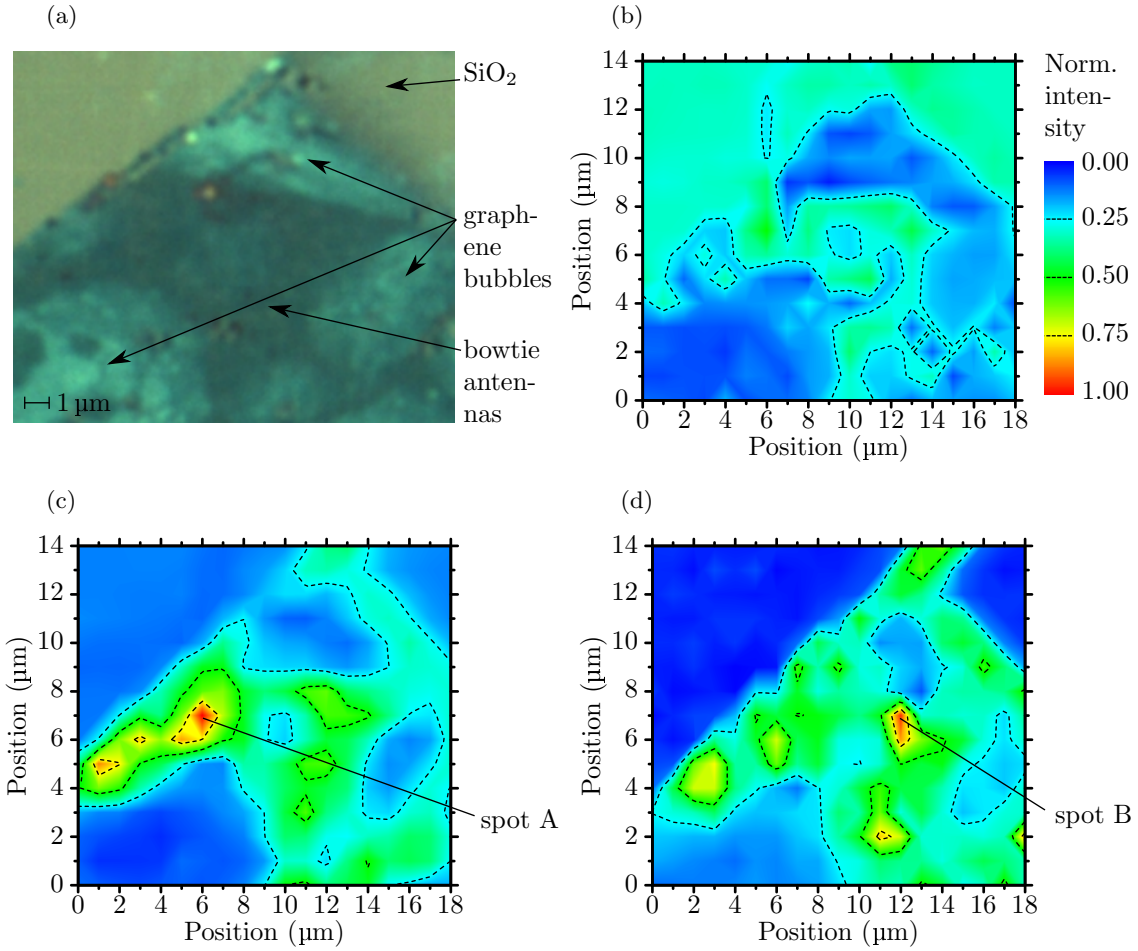

FIGURE 5.3: 2D mode intensity maps for (b) 532 nm, (c) 638 nm and (d) 785 nm excitation wavelengths, all taken on the same area shown in (a) with a resolution of 1 µm. The intensities were normalized for better comparison (cf. (b) for scale). Spot A and B were measured using wavelength-scanned Raman spectroscopy.

the upper half, the graphene sheet is directly lying on top of 290 nm SiO_2. The dark green area is totally covered with a hexagonal lattice of bowtie antennas as described in Sec. 4.3.1. In the light green areas, the graphene sheet was bent upwards, likely by gas accumulation. The graphene is not touching the surface in these areas as will be shown below.

Each map in Fig. 5.3 shows the intensity of the 2D mode of graphene fitted by a single Lorentzian peak as a function of position. All maps were normalized to the maximum intensity.

Figure 5.2 indicates that the resonance condition of the structure is expected to be around 670 nm. Therefore, the occurrence of plasmonic hotspots[2] is expected to be observable at an excitation wavelength of 638 nm. This is close to the scattering maximum

[2] Areas having a much higher Raman scattering cross section as the surrounding areas due to plasmonic enhancement.

($\Delta E = 96\,meV$, cf. the brown line in Fig. 5.2). An area without plasmonic antennas was included, providing a reference Raman signal of graphene not influenced by antennas.

Comparing Figs. 5.3 (b) - 5.3 (d) we find that no amplification occurs for 532 nm excitation. There are only small variations of the 2D mode intensity on areas where graphene touches the surface. The antennas show only a small influence on the signal intensity as the color is nearly identical for areas with and without antennas (cf. Fig. 5.3 (b)). We also find that the intensity is lower on graphene bubbles. This is expected as the focal depth of the 100x objective used was small (1 µm). This is less than the expected height of the observed graphene bubbles which is assumed to be in the order of a few µm.

In Figs. 5.3 (c) and 5.3 (d) the signal intensity for graphene on SiO_2 is minimal compared to areas covered with antennas. We observe various hotspots, whose distribution depends on the excitation wavelength. Furthermore, we find that amplification occurs all over the areas covered with antennas, excluding the regions of the graphene bubbles.

All these findings indicate that plasmonic amplification is sensitive to the excitation wavelength, showing no amplification for wavelengths outside of the plasmonic resonance. We find hotspots having a different resonance wavelength. This is mainly caused by shape inhomogeneities of the bowtie antennas (cf. Fig. 4.6 and Sec. 2.3.6). Thus, the resonance wavelength is expected to vary. We also find that amplification requires the graphene sheet to be close to the plasmonic antennas as we do not observe any enhancement at the areas without antennas or at the areas with graphene bubbles.

Two hotspots were selected for wavelength-scanned Raman spectroscopy. They are marked spot A (Fig. 5.4 (a)) and spot B (Fig. 5.4 (b)). Plotting the intensity of the 2D mode over excitation energy we find a resonance at 1.68 eV (739 nm) for spot A and 1.65 eV (750 nm) for spot B. Equation (3.36) was used to fit the experimental data. The measurement shown in Fig. 5.4 (a) was acquired using the entire range of available excitation wavelengths. Spot A shows a maximum enhancement of 1.4×10^3 and spot B 4.3×10^4. Equation (3.36) predicts an outgoing resonance. However, due to a high variance in the measured data, the existence of the outgoing resonance is only weakly observable and may be argued upon. Thus, the value of κ is unreliable due to the lack of measured data for the outgoing resonance. The obtained fitting parameters are listed in Tab. 5.1 with the uncertainty of κ indicated by a question mark. The resonance energy E_{Au} obtained from the Raman measurements is shifted by about 0.2 eV in comparison to the maximum of the scattering cross section (cf. Fig. 5.2). The spectral width Γ_{Au}

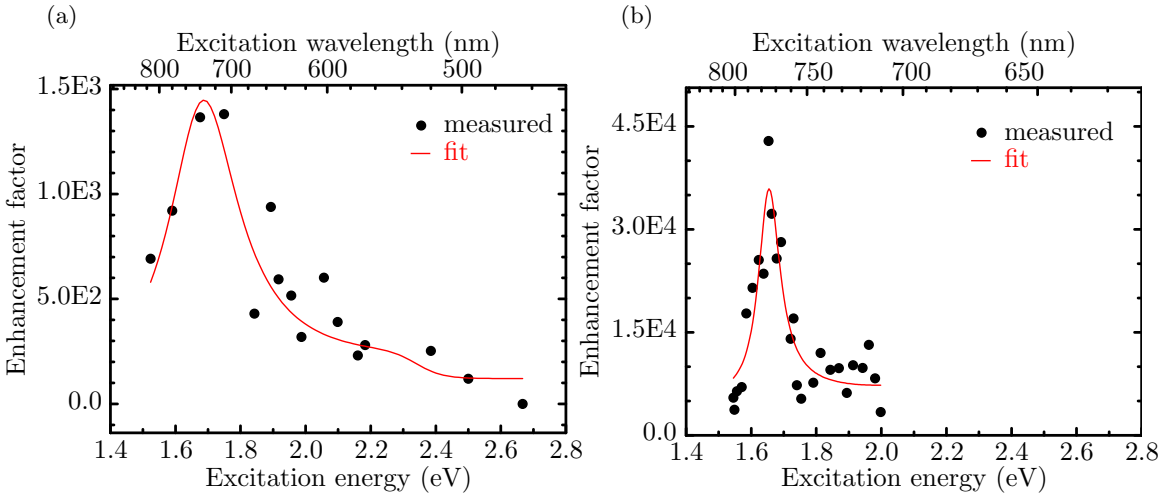

FIGURE 5.4: Wavelength-scanned Raman measurements of (a) spot A (found in Fig. 5.3 (c)) and (b) spot B (found in Fig. 5.3 (d)). The fits were obtained by fitting the measured data to Eq. (3.36).

Hotspot	E_{Au}	Γ_{Au}	κ	EF	ΔE
A	1.68 eV (739 nm)	130 meV	−0.1 ?	1.4×10^3	0.17
B	1.65 eV (750 nm)	40 meV	−1.0 ?	4.3×10^4	0.20

TABLE 5.1: Fitting parameters for spot A and B. The fits are shown in Figs. 5.4 (a) and 5.4 (b). The values of κ, extracted from the fits, are uncertain and therefore questionable which is indicated by the question mark. The enhancement factor EF and the energetic shift $\Delta E = E_{DF} - E_{Au}$ to the measured dark field maximum E_{DF} is also given.

is found to be smaller than the spectral width of the plasmon being 261 meV[3]. This is in contradiction to the conventional EM SERS theory presented in Sec. 2.4.

The position of the 2D mode and the enhanced 2D mode as a function of excitation energy is shown in Fig. 5.5 for graphene on SiO_2 and graphene located on antennas. Besides a slight upshift in the position of the enhanced 2D mode for graphene on antennas the shift rates are very similar. They are $116 \pm 3\,\mathrm{cm}^{-1}$ for graphene on top of SiO_2 and $109 \pm 6\,\mathrm{cm}^{-1}$ for graphene on top of the antennas. The small difference in their position may be attributed to doping of the graphene, induced by the environment (cf. Ref. [87, 102]).

We find that the enhancement properties of a plasmonic NSL surface vary strongly in terms of resonance wavelength and broadness of the resonance due to inhomogeneities of the antennas. We also find that the ingoing resonance is shifted to lower energies compared to the scattering maximum of the antennas, shown in Fig. 5.2. The values

[3]This value was obtained from the simulation shown in Fig. 5.2 using the full width at half maximum value.

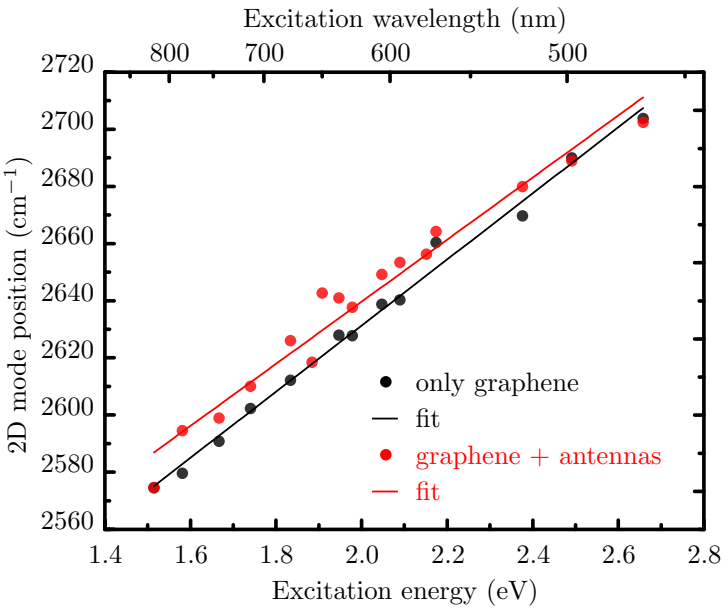

FIGURE 5.5: Position of the 2D mode as a function of excitation energy for graphene lying on SiO_2 and graphene lying on antennas.

are given in Tab. 5.1. This indicates that the Raman signal is enhanced by the near field of the antennas as the near field is shifted to lower energies (cf. Sec. 2.3.2.2). The amplification of the graphene 2D mode intensity due to plasmonic enhancement could be observed. The enhancement factor of the Raman signal is 5 for spot A and 13 for spot B. As described in Sec. 2.3.5 we find an area enhancement factor of 270, resulting in the enhancements given in Figs. 5.4 (a) & 5.4 (b). As the given area enhancement factor was calculated for a cylindrical dimer antenna the value is just an estimate. However, as bowtie dimer antennas and cylindrical dimer antennas show similar plasmonic behavior their area enhancement factor is expected to be similar (cf. Sec. 2.3.6). Additionally, the shift rates of the position of the 2D mode and the plasmon-enhanced 2D mode were measured. Besides the amplification of the 2D mode intensity and a spectrally small resonance no further influence of the antennas was observed.

5.3 Raman measurements on dimer antennas

Dimer antenna samples were produced as described in Sec. 4.3.2. Two sample designs were investigated. One having a SiO_2 thickness of 290 nm and one having a SiO_2 thickness of 270 nm. The intention of a reduced SiO_2 layer thickness was to shift the plasmonic resonance to lower wavelengths by changing the dielectric environment (cf. Sec. 2.3.3).

This section will start by introducing the plasmonic properties of the cylindrical dimer antennas measured by dark field spectroscopy. The influence of the SiO_2 layer thickness

will be shown and the measurements will be compared to simulated spectra. Subsequently, wavelength-scanned Raman measurements of dimer antennas covered with graphene will be shown and analyzed using the theory of plasmon-enhanced Raman scattering presented in Sec. 3.5.

5.3.1 Dark field spectra

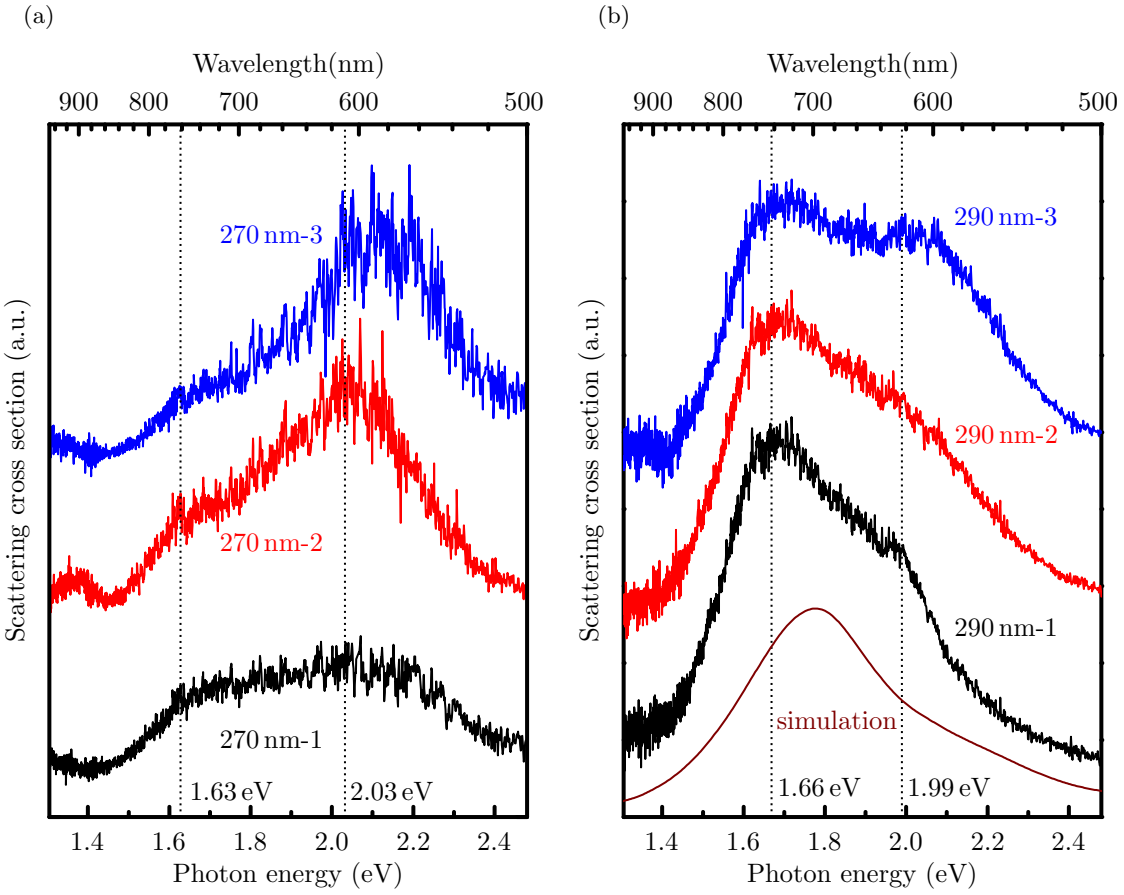

FIGURE 5.6: Dark field spectra of two dimer antenna samples with different SiO_2 layer thicknesses. (a) plots the spectra obtained on a sample with 270 nm SiO_2 layer. (b) plots the spectra of the sample having a 290 nm SiO_2 layer. The name of each dimer antenna is given in the respective color of the spectrum. As a guide to the eye, the ingoing and outgoing resonances and their respective photon energy are indicated using dotted lines.

Figure 5.6 shows dark field scattering spectra of the cavity mode (cf. Sec. 5.1) obtained on three dimer antennas for each SiO_2 thickness. The scattering spectra were calculated using Eq. (5.2). Figure 5.6 (a) shows the cavity modes from the sample having a 270 nm SiO_2 layer and Fig. 5.6 (b) shows the cavity modes of the sample with a 290 nm SiO_2 layer. The naming convention presented in the figures will also be used throughout the text below. Figure 5.6 (b) includes a simulated far field spectrum of the dimer antenna

under investigation. As all dimer antennas measured have a diameter of 100 nm and a gap spacing of 30 nm (cf. Sec. 4.3.2) only one simulation was included. The thickness of the SiO_2 layer could not be varied in the simulations.

The most intense resonance for the sample having a 270 nm thick SiO_2 layer is 2.03 eV (610 nm) (cf. Fig. 5.6 (a)). Thus, a plasmonic resonance around 2.03 eV is expected. The sample having a 290 nm SiO_2 layer thickness (cf. Fig. 5.6 (b)) has its most intense resonance at 1.66 eV (750 nm). Hence, it was possible to tune the intensity of the dominant resonance of the dimer antennas by changing the SiO_2 layer thickness. However, the resonances below 1.7 eV were are not within the measurable range of our laser systems.

5.3.2 Raman spectra

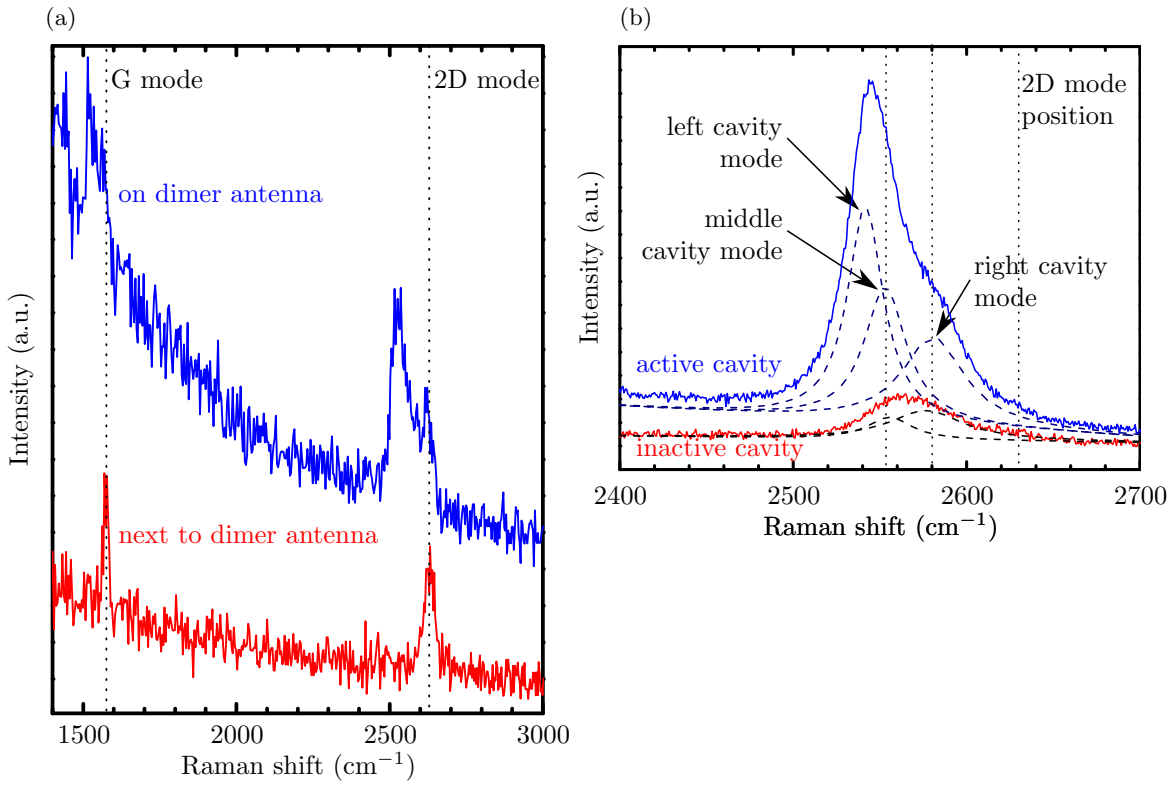

FIGURE 5.7: Influence of the dimer antennas on the Raman signal. (a) amplification and additional Raman modes appear when measuring on top of the dimer antenna in parallel polarization. (b) different Raman modes observed when changing the polarization from parallel (active cavity) to perpendicular (inactive cavity) while measuring on top of the dimer antenna. The 2D mode is not observable hence its position is being indicated by the rightmost dotted line.

A typical Raman spectrum obtained when measuring on a dimer antenna contains Raman modes softened[4] in comparison to the 2D mode. Figures 5.7 (a) and 5.7 (b) show the influence of the dimer antenna on the Raman signal.

Figure 5.7 (a) compares spectra measured directly on top of the dimer antenna and spectra measured next to it. In the latter case we observe the G and 2D modes of graphene. When measuring on top of the dimer antenna with a polarization parallel to the dimer antenna axis we observe the G and 2D modes but also additional modes at lower Raman shifts next to them. On top of the dimer antenna we also observe hot luminescence[5] originating from the dimer antenna.

Figure 5.7 (b) compares Raman modes obtained for parallel (active cavity) and perpendicular (inactive cavity) polarizations with respect to the dimer antenna axis at 1.99 eV (624 nm). For the cavity being active we observe three Raman modes, called left, middle and right cavity modes (cf. Fig. 5.7 (b)). They have a higher intensity compared to the 2D mode which is not observable in the spectrum as the cavity modes outshine the 2D mode.

In the case of an inactive cavity, the signal contains only contributions from the uncoupled EM fields of the cylindrical antennas (cf. Sec. 2.3.4). In the resulting Raman spectrum we observe that the overall intensity of the spectrum is strongly reduced. Additionally, we find the left cavity mode to disappear and the middle and right cavity modes to become significantly weaker. It is obvious to attribute the enhancement of the cavity modes to the EM field in the cavity. As the graphene inside the cavity is strained, the strain is likely to cause mode softening and splitting (cf. Refs. [26, 87, 104, 105]). The middle and right cavity modes are still observable for an inactive cavity. So we conclude that they are originating from the strained regions next to the dimer antenna. This conclusion has also been drawn in Ref. [26].

In Fig. 5.7 (a) we find three Raman modes for an active cavity. As the graphene is being pulled into the gap between the cylindrical antennas we find that the graphene is strained (cf. Sec. 4.3.2) at the region of the highest field amplification (cf. Sec. 2.3.4). Hence, we may attribute the appearance of the three modes to strain in graphene. Ref. [88] does predict the appearance of three Raman modes in strained graphene for some scattering configurations (cf. Fig. 5 in [88]). However, it is not possible to conclusively determine if the observation of three Raman modes for an active cavity originates from plasmonic enhancement or strain (or both). There are two possible explanations.

[4] Mode softening in Raman scattering means that a Raman mode is being shifted to lower energies (Raman shifts) as a result of a lowered phonon energy.

[5] Inelastic light scattering by excited state relaxation in heavily doped semiconductors or metals (cf. Refs. [73, 103]).

1. The Raman signal of the strained graphene inside of the gap outshines all other Raman contributions due to the high field intensity inside of the gap.

2. Due to the high strength and localization of the fields inside of the gap, the Raman process is being altered, leading to the excitation of additional Raman modes.

Yet, three Raman modes were not observed for every dimer antenna investigated. Some dimer antennas showed only two Raman modes. However, no parameter showing a systematic influence on the appearance of two or three Raman modes was found.

To account for the possibility of different processes leading to the standard Raman spectra of graphene and the plasmon-enhanced Raman spectra shown here the enhanced Raman modes were named cavity modes. The non-amplified 2D mode will be called 2D mode as usual. In the amplified spectra we find the three cavity modes to outshine the 2D mode.

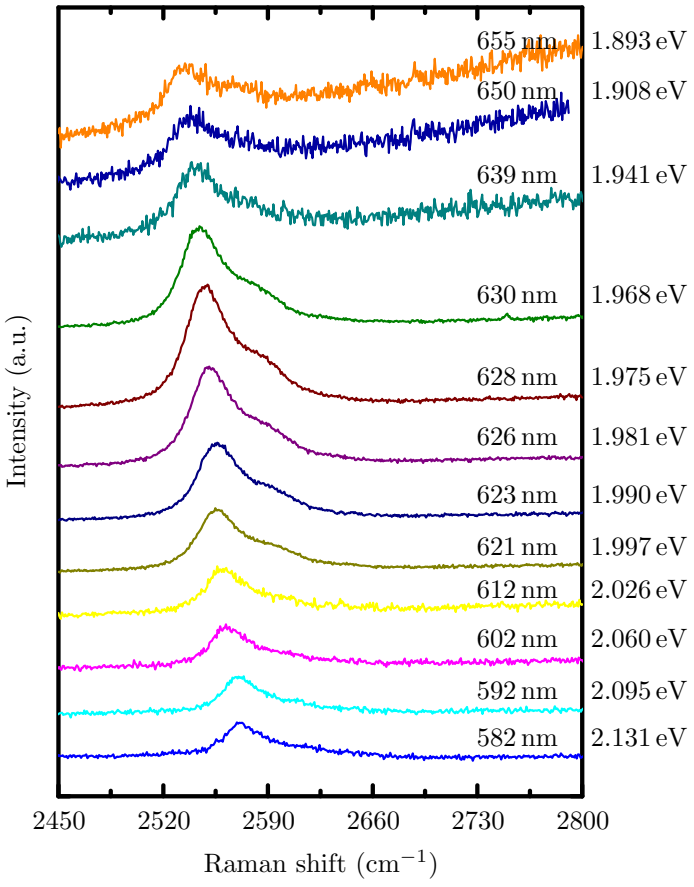

FIGURE 5.8: Raman spectra recorded on dimer antenna 290 nm-2 with the laser polarized parallel to the dimer antenna axis for different excitation wavelengths.

Figure 5.8 shows spectra obtained on dimer antenna 290 nm-2 for the laser polarization being parallel to the dimer antenna axis. Different excitation energies are shown, close to the resonance energy of 630 nm. The resonance is clearly seen and the cavity modes

become more intense around the resonance energy. All Raman modes become more and more softened for decreasing excitation energies. Thus, we observe a dispersive behavior anticipated for the 2D mode and the cavity modes as they originate from the 2D mode. The dispersion will be investigated further below.

5.3.3 Raman mapping of a dimer antenna

This section will investigate the spatial Raman properties of dimer antenna 290 nm-3. The corresponding scattering cross section is shown in Fig. 5.6 (a).

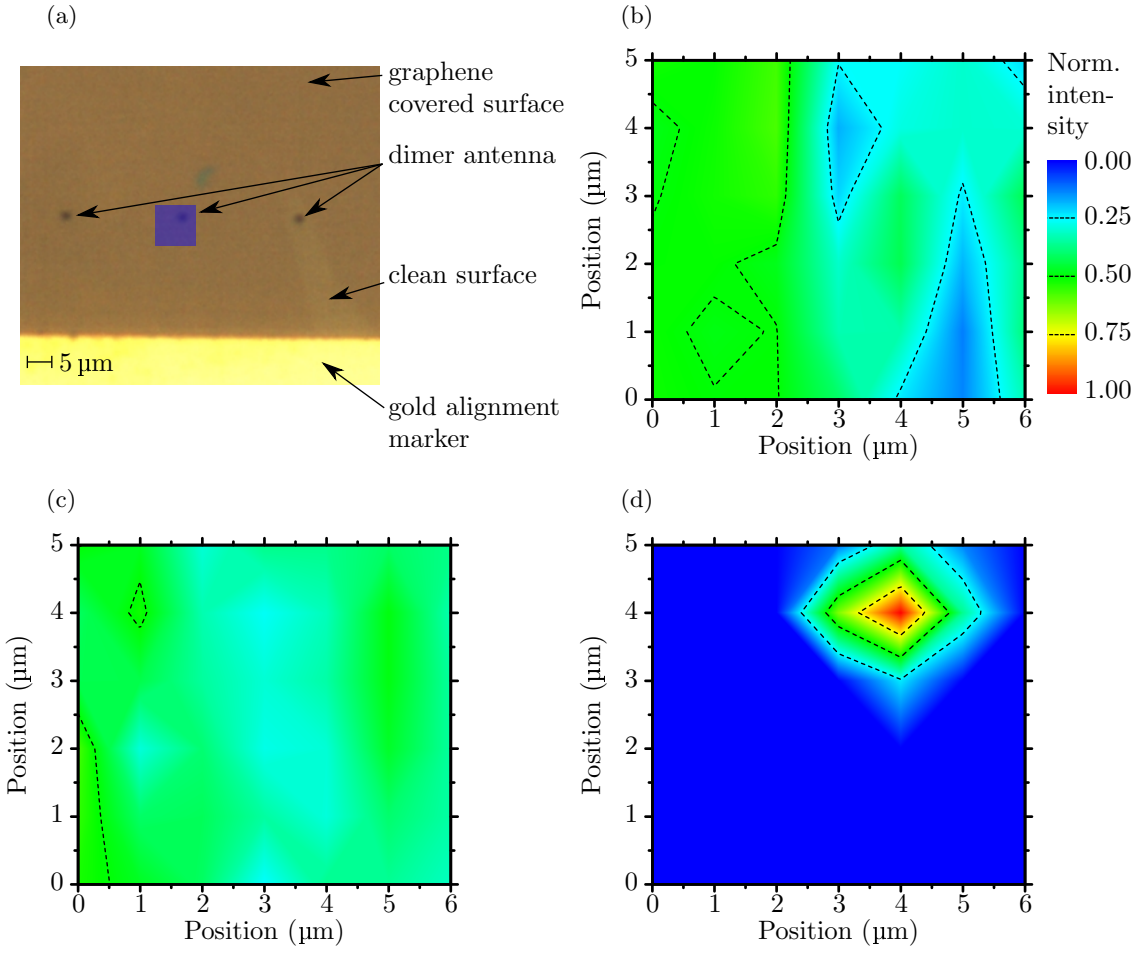

FIGURE 5.9: 2D mode intensity maps of a dimer antenna sample for 532 nm and 638 nm excitation wavelengths. Raman mapping was done on the blue area shown in (a) with a resolution of 0.5 µm. (b) shows the intensity of the non-amplified 2D mode of graphene for 532 nm excitation. (c) shows the intensity of the 2D mode for 638 nm excitation. (d) shows the intensity of the 2D cavity modes for 638 nm excitation. All maps use the same scale as (b).

The dark field scattering cross section implies that we will observe a maximum amplification around 2.03 eV (610 nm). Thus, Raman maps were recorded for 638 nm (resonant) and 532 nm (non-resonant) excitation.

Figure 5.9 (a) shows an optical microscope image of the surface of a dimer antenna sample. The size of the dimer antennas is below the diffraction limit. Thus, they are only observable as small black dots. Graphene is covering the entire surface except of an area at the bottom right edge. The space between the dimer antennas is 5 µm. Thus, each dimer antenna was measured individually using a 100x objective. The Raman maps were acquired for dimer antenna 290 nm-3, indicated by the blue area.

Figure 5.9 (b) shows the intensity of the 2D mode for 532 nm excitation. No amplification is observed. The intensity varies only slightly by a total amount of 28%. This may be attributed to height differences of the graphene as it is lying like a blanket over the dimer antenna and the surface. Because of this the focal point was chosen by maximizing the intensity on the dimer antenna. On the left hand side we observe a small graphene bubble, increasing the intensity. We also find the intensity of the 2D mode being lower around the dimer antenna. This is a result of the dimer antenna not having any significant field intensity inside of the cavity (cf. Fig. 2.19 (a)). As an excitation wavelength of 532 nm is out of resonance, the fields get scattered around the dimer and are not focused into the cavity (cf. Sec. 2.3.4).

In Fig. 5.9 (c) we observe an intensity variation of 32% for the 2D mode. The strained region is observable to the right hand side of the map. It is elongated as graphene shows ripples, reaching as far as 2 µm away from the dimer antenna. The strain mode intensity is shown in Fig. 5.9 (d). Comparing Maps 5.9 (b), 5.9 (c) and 5.9 (d) we find that the dimer antenna amplifies the 2D mode of graphene by $\approx 67\%$ and causes the appearance of strain modes having an intensity of $\approx 340\%$ of the intensity of the 2D mode next to the dimer antenna. Thus, we obtain an enhancement factor of 9×10^2.

As already pointed out in Ref. [26] we also find a very high spatial confinement of the hotspot, making the wavelength-scanned measurements very demanding.

In conclusion, we find that the dimer antenna is causing the appearance of additional Raman modes and the concurrent amplification of all Raman modes originating from the vicinity of the dimer antenna. Polarization measurements indicate that the Raman strain modes emanate from the cavity in between the dimer antenna (cf. Sec. 5.3.2). Amplification occurs as already observed for the NSL sample (cf. Sec. 5.2) as a function of excitation wavelength.

5.3.4 Wavelength-scanned Raman spectroscopy

Figure 5.10 shows wavelength-scanned Raman measurements for four dimer antennas. The enhancement factor was calculated as described in Sec. 2.3.5 and the data was

fitted using Eq. (3.36).

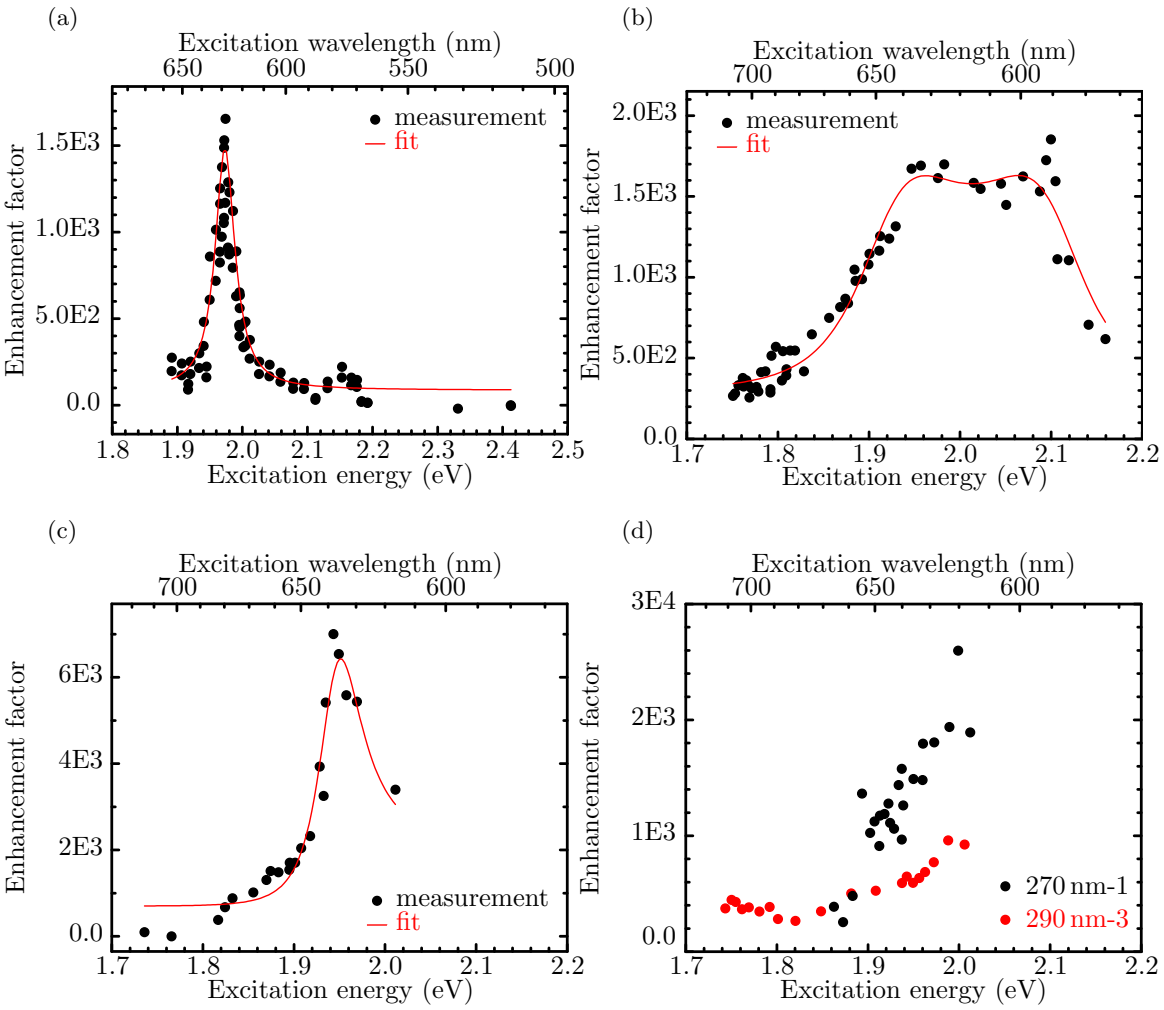

FIGURE 5.10: Wavelength-scanned Raman spectra of different dimer antennas. The plots show the following dimer antennas: (a) 290 nm-2, (b) 290 nm-1, (c) 270 nm-2 and (d) 270 nm-1 & 290 nm-3. The fitting values are given in Tab. 5.2. The data shown in (d) was not completed as the dimer antennas were damaged during the measurements.

The plots in Figs. 5.10 (a), 5.10 (b) and 5.10 (c) show spectrally sharp peaks at the ingoing resonance around 1.99 eV (620 nm). The resonance curves of dimer antennas 270 nm-1 and 290 nm-3 in Fig. 5.10 (d) could not be completed as they were damaged when the excitation energy approached the resonance energy. However, the data indicates that these dimer antennas had a resonance energy in the same region as the other dimer antennas.

Table 5.2 shows the fitting values from Eq. (3.36) for the dimer antennas in Fig. 5.10. Additionally, the difference ΔE to the respective dark field resonance (cf. Fig. 5.6) is given. As in Sec. 5.2, we find that the Raman resonance is redshifted compared to the dark field resonance with a maximum shift of 90 meV. Additionally, Fig. 5.6 indicates

Antenna	270 nm-2	290 nm-1	290 nm-2
EF	5.0×10^3	1.9×10^3	1.7×10^3
E_{Au}	1.94 eV (638 nm)	1.92 eV (644 nm)	1.97 eV (630 nm)
$\hbar\omega$	0.17 eV	0.09 eV	0.17 eV
Γ_{Au}	0.03 eV	0.07 eV	0.02 eV
κ	1 ?	400 ?	0 ?
ΔE	0.09 eV ?	0.07 eV	0.02 eV

TABLE 5.2: Fitting parameters for the resonance curves shown in Fig. 5.10. $\Delta E = E_{DF} - E_{Au}$ is the shift between the dark field resonance and the Raman resonance. The questionmark behind a value indicates that this parameter could not be fitted reliably.

a second resonance peak around 1.65 eV which could not be measured as the sensitivity of the Raman spectrometer was not sufficient for measurements below 1.7 eV.

By changing the thickness of the SiO_2 layer we changed the dielectric environment of the dimer antenna. This resulted in different scattering cross sections that are shown in Figs. 5.6 (a) & 5.6 (b). The idea was to shift the resonance energy of the plasmonic amplification by changing the dielectric environment of the dimer antenna. Comparing the values given in Tab. 5.2 we find that the thickness of the SiO_2 does not influence E_{Au}. However, we found that the SiO_2 layer thickness has an influence on the enhancement factor EF which is higher for the 270 nm dimer antenna. This is well observable in Fig. 5.10 (d). Figure 5.6 also suggests this finding as the scattering cross section around 2.0 eV is higher for the 270 nm dimer antenna. The reason of this increase in the enhancement factor is attributed to the change in the local dielectric environment of the dimer antenna (cf. Sec. 2.3.3). Additionally, higher strain of the graphene created by the etched SiO_2 layer could contribute to the larger enhancement. The strain is expected to increase for the 270 nm sample as the height difference between the dimer antenna and the surface is 20 nm larger compared to the 290 nm sample (cf. Sec. 4.3.2). Due to higher strain the graphene may be pulled in further into the gap and is therefore exposed to higher field amplitudes (cf. Fig. 2.21) resulting in a larger enhancement of the Raman signal.

Simulations (cf. Sec. 2.3.2.2 and Fig. 5.6 (b)) show a spectral width of the plasmonic dimer antenna mode of 460 meV[6] for the dimer antenna used. Comparing this to the values obtained for Γ_{Au} in Tab. 5.2 we find that the measured Raman resonance is not explainable by the established EM SERS theory (cf. Sec. 2.4) as it predicts a resonance as broad as the width of the plasmonic dimer antenna mode in the near field.

Antenna 290 nm-1 shows a resonance width of $\Gamma_{Au} = 0.07$ eV. Additionally, the separation of ingoing and outgoing resonance peaks was reduced to 0.09 eV for this spectrum only. The reason is unknown and we find no correlation to the scattering cross section.

[6] Obtained using the FWHM of the simulation shown in Fig. 5.6.

Antenna	290 nm-1		290 nm-2	
	A (nm)	B (nm/eV)	A (nm)	B (nm/eV)
l. cav. mode	2251 ± 5	127 ± 3	2296 ± 14	131 ± 7
m. cav. mode	2291 ± 8	127 ± 4	2250 ± 39	162 ± 19
r. cav. mode	2391 ± 8	113 ± 4	2272 ± 31	162 ± 15
Antenna	270 nm-1		270 nm-2	
	A (nm)	B (nm/eV)	A (nm)	B (nm/eV)
l. cav. mode	2106 ± 18	169 ± 9	2223 ± 9	119 ± 5
m. cav. mode	2149 ± 46	156 ± 24	2286 ± 12	116 ± 6
r. cav. mode	2158 ± 25	175 ± 13		

TABLE 5.3: Fitting parameters obtained by linear regression of the fits shown in Fig. 5.11. A linear model $\omega = A + B \cdot E_L$ was used. A and B are fitting values and E_L is the excitation energy of the laser.

The value of κ was not evaluated as the available wavelength range did not cover ingoing and outgoing resonances due to their large separation of 330 meV and the lack of laser lines below 2.25 eV (550 nm) and a lack of sensitivity of the detector for wavelengths above 1.70 eV (730 nm). Therefore, the values found in Tab. 5.2 are not reliable, which is indicated by a question mark.

In conclusion, we found that the Raman resonance is spectrally much smaller than the plasmon resonance contradicting conventional EM SERS theory. We also found the Raman resonance redshifted to the resonance of the scattering cross section indicating that the Raman amplification originates from the near field around the dimer antenna (cf. Sec. 2.3.2.2). It was also shown that the thickness of the SiO_2 layer influences the enhancement factor observed in wavelength-scanned Raman measurements.

5.3.5 Dispersion of the graphene Raman modes

Figure 5.11 show the positions of Raman modes measured over excitation energy for various dimer antennas. In each diagram we find the positions of the three different modes introduced in Fig. 5.7 (b). In Fig. 5.11, the left cavity mode is always marked in black, the middle cavity mode in blue and the right cavity mode in red. We find a linear dispersion for all modes. Antenna 290 nm-3 is not shown as the calibration failed for this measurement.

Table 5.3 shows the obtained fitting values for a linear dispersion model $\omega = A + B \cdot E_L$ with A and B being fitting values and E_L being the excitation energy of the laser. We find that all Raman modes have a significantly higher dispersion than the unstrained 2D mode of graphene, which shifts by 100 cm^{-1}/eV. The maximum shift rate observed

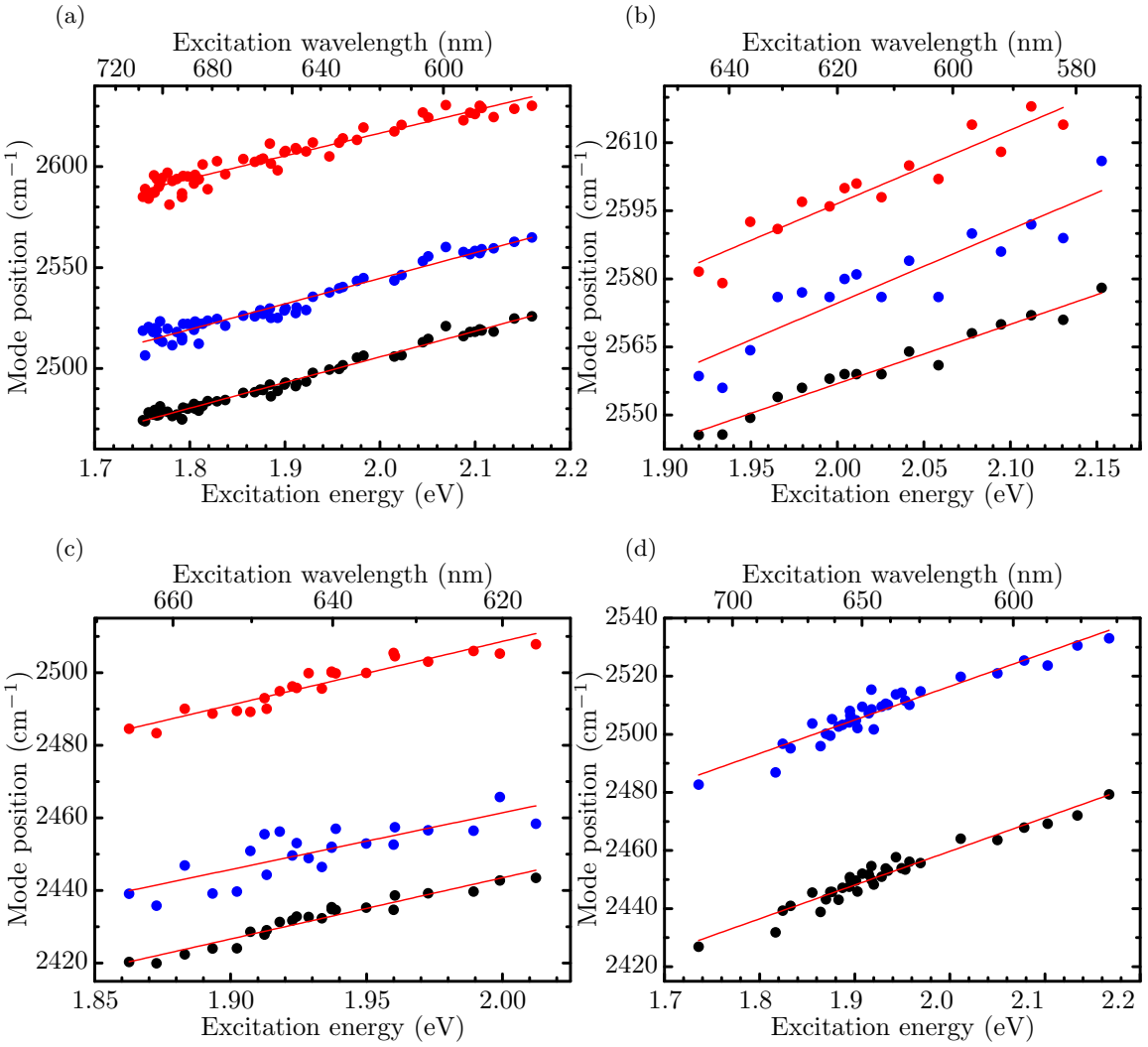

FIGURE 5.11: Position of the Raman modes observed for different dimer antennas. The following dimer antennas are shown (a) 290 nm-1, (b) 290 nm-2, (c) 270 nm-1 and (d) 270 nm-2. The left cavity mode is marked in black, the middle cavity mode is marked in blue and the right cavity mode is marked in red. All modes were fitted using a linear fit. The obtained fitting values are shown in Tab. 5.3.

is 175 cm^{-1}/eV. This is an increase of 75% and cannot be explained by measurement inaccuracies.

Reference [81] recently investigated the behavior of the 2D mode of graphene as a function of excitation energy E_L theoretically, using various screening conditions in graphene. As described in Sec. 3.1, screening influences the energy of a phonon via the Kohn anomaly and therefore the gradient of the phonon dispersion. They assume freestanding graphene with no additional screening by a supporting surface and find a linear dispersion $\partial\omega_{2D}/\partial E_L$ of the 2D mode depending on the gradient of the electronic band

structure and phonon dispersion of the graphene investigated

$$\frac{\partial \omega_{2D}}{\partial E_L} = 2\frac{|\vec{\nabla}\omega_{2TO}(E_L)|}{|\vec{\nabla}E_g(E_L)|}. \tag{5.3}$$

With $\vec{\nabla}\omega_{2TO}(E_L)$ being the gradient of the phonon dispersion and $\vec{\nabla}E_g(E_L)$ being the gradient of the electronic band structure. $\partial\omega_{2D}/\partial E_L$ corresponds to the fitting parameter B in Tab. 5.3. From Eq. (5.3) we find that the dispersion of the 2D mode is proportional to the slope of the phonon dispersion and has inverse proportionality to the slope of the electronic dispersion.

Reference [90] measured dispersion values from graphene exposed to an uniaxial strain of $\epsilon = 2.3\%$ to $106\,\mathrm{cm}^{-1}/\mathrm{eV}$ for the left 2D mode and to $99\,\mathrm{cm}^{-1}/\mathrm{eV}$ for the right 2D mode (cf. Sec. 3.4.3). Reference [104] calculated dispersion values of graphene exposed to various uniaxial strains. Their calculated dispersions are ranging from $79\,\mathrm{cm}^{-1}/\mathrm{eV}$ for $\epsilon = -1\%$ and $113\,\mathrm{cm}^{-1}/\mathrm{eV}$ for $\epsilon = 3\%$.

Comparing the shifts found in the literature to the ones obtained in Tab. 5.3, the dispersion of the cavity modes is significantly increased. This is especially interesting as Ref. [26] estimates the strain imposed on a very similar system to 0.8% hydrostatic and $< 0.4\%$ shear strain. Thus, the shift rate is expected to be in the oder of $100\,\mathrm{cm}^{-1}/\mathrm{eV}$. It is known from theory (cf. Eq. (3.21)) and experiment[7] that hydrostatic strain predominantly changes the shift rate of the 2D mode. Thus, shear strain only has a minor influence on $\partial\omega/\partial E_L$.

It has to be emphasized that the graphene within the cavity is not uniaxially strained and therefore the values given in Ref. [104] may not be used for a rigorous comparison. However, they may be used to assess the order of the shift rate as uniaxial strain is always smaller than the corresponding hydrostatic strain (cf. Sec. 3.4.3). Therefore, the difference between the values found in Refs. [90, 104] and Tab. 5.3 is not explainable by strain alone.

The shift rate of the 2D mode follows the phonon dispersion as described in Sec. 3.4.3 and Eq. (5.3). It is reasonable to assume an increase in $\partial\omega/\partial E_L$ for higher strains imposed on graphene, as found in Ref. [104]. The shift found on uniaxial strain may be used as an upper bound for the change in the phonon dispersion. The values found in Table III of Ref. [104] indicate a saturation of the shift rate at $120\,\mathrm{cm}^{-1}/\mathrm{eV}$ for increasing strain. Additionally, strain values higher than 3% are very unlikely as they would result in damaging the graphene sheet as pointed out in Ref. [26].

[7] Unpublished results from private communication with S. Heeg

The reasoning above seems to exclude strain as the only origin of the high shift rate of the cavity modes in comparison to measurements of graphene exposed to higher strains but without plasmonic amplification.

We may assume that the dimer antenna distorts the electronic band structure of graphene lying on top of it due to the high field amplification. Thus, we would also obtain a distortion of the phonon dispersion as the Kohn anomalies in graphene couple the electronic band structure and the phonon dispersion. Considering Eq. (5.3) we would find an influence on the Raman shift of the 2D mode. This could explain the higher shift rates found in Tab. 5.3.

Additionally, the shift rates show a high variation among each dimer antenna which is unlikely if strain was the sole cause for the shift rates observed. It is therefore likely that the plasmonic interaction between the dimer antenna and the graphene induces a distortion of the phonon dispersion and electronic band structure. This may explain the different Raman shift rates observed. However, the exact origin of the increased shift rate needs to be investigated further.

Chapter 6

Conclusions

The aim of this thesis was to deepen the knowledge of the fundamental physics involved in the plasmonic enhancement of the Raman signal of graphene. Our approach was to use wavelength-scanned Raman scattering which was never done on a single dimer antenna covered by graphene. We found spectrally sharp resonances that could not be explained by the conventional theory of SERS. Therefore, we developed with the help of my supervisor Stephanie Reich a new theory of plasmon-enhanced Raman scattering that considers the enhancement as a quantum mechanical process. It is in contradiction to the conventional theory that considers the enhancement a result of the strong fields found near a plasmonic antenna. Our theory predicts two resonances that could not be observed in this thesis. However, successive work[1] found both resonances while investigating the G mode of graphene, providing proof for the theory. Furthermore, we observed an increased shift rate of the plasmon-enhanced Raman modes. This finding suggests that the dimer antenna is influencing the electronic band structure and phonon dispersion of graphene. However, this needs further investigation in future measurements. The findings of spectrally small resonances and an increased shift rate are new to the community investigating surface-enhanced Raman scattering and led to a better understanding of the physics behind SERS. The theory proposed in this thesis is a first step to the explanation of plasmon-enhanced Raman scattering.

We used FDTD simulations and dark field spectroscopy to investigate the scattering behavior of dimer antennas that consisted of two cylindrical antennas with various diameters and gap sizes. We found that the diameter, gap size and dielectric environment strongly influence the near field scattering cross section and field distribution of a dimer antenna. Via the simulations we observed that the field amplification in the gap of the dimer antenna is highest at the bottom. Additionally, the incoming fields are strongly

[1] Publication under review. A preprint will be found at http://arxiv.org/abs/1503.03835

depolarized and highly localized by the antenna. This has to be considered when investigating the appearance of Raman modes not allowed under the incident laser polarization.

We found that the enhanced signal is generated exclusively in the cavity of the dimer antennas. Additionally, we observed three Raman modes where, according to measurements on strained graphene, only two modes were expected. This observation may be caused by the strain configuration of the graphene inside of the cavity. However, we also observe a dispersion rate that is significantly higher than the dispersion rate expected for strained graphene. These interesting findings need to be investigated in future measurements to clarify their origin. The realization of additional measurements is important as they may give more insight into the physical origins of the enhanced Raman signal.

Our observations show that a careful design of the plasmonic antenna is required. This means that it is advisable to simulate the scattering behavior and field distribution of the antennas used. The comparison of such simulations with dark field measurements gives a better understanding of the scattering behavior of the manufactured antennas. We observed that the Raman scattering maximum is always redshifted to the far field scattering maximum obtained by dark field measurements. As the shift varied from antenna to antenna this is another observation that needs clarification as it contradicts the findings of van Duyne et. al. in Ref. [29] who predict a higher redshift.

The new findings described above indicate that the effect of surface-enhanced Raman scattering needs more clarification. Wavelength-scanned Raman scattering is a versatile tool for this purpose. Our observations may be extended by more exact simulations. For example, the Cr bonding layer situated between the antenna and the SiO_2 may be incorporated into the simulations. Additionally, the graphene lying on top of the antenna may be incorporated. Both change the dielectric environment of the antenna and therefore its scattering cross section and field distribution.

Investigating other antenna designs will show the influence of the near field localization and field distribution around the antenna. For example it would be interesting to measure the effect of different gap sizes on the wavelength-scanned Raman profile. Additionally, it would be interesting to use different analytes such as carbon nanotubes as a one dimensional probe or two dimensional materials having an intrinsic Raman resonance energetically close to the plasmonic resonance of the antenna used. Such measurements will make it possible to determine the coupling mechanism between the antenna and the analyte and therefore allow a much more complete picture of the enhancement process.

This thesis showed that the effect of plasmon enhancement is a quantum effect not fully understood yet. The findings presented here are a first step to a complete understanding of the physics involved in plasmon-enhanced Raman scattering. This understanding

will make it possible to use the enhancement effect for reliable and repeatable detection of various analytes up to the single molecule level. Plasmonic antennas can be manufactured using the production techniques of the semiconductor industry enabling cheap production and making them available to a wide amount of sensing applications.

Acknowledgements

This work would not have been possible without the help of so many people which accompanied me during the years of work involved in this thesis.

Stephanie Reich I thank her for all the endless hours of discussions and explaining me things over and over again. She was a very kind and helpful advisor, especially when she had time to be in the lab. She kept me going when I thought all the work was for the bin. It was great to have so much support, especially being able to buy the lab equipment needed to make the measurements work and financing the long research stays abroad. I am very grateful in having all these opportunities and being able to follow the stony path I pursued during the time in her group. Thank you very much!

Patryk Kusch I thank him for all the endless discussions we had, not only about physics and for all the fun we had in the lab adjusting the lasers and tinkering with the Raman setups. I want to especially thank him for the practical advise on adjusting the Ti:Sa and the T64000 when something seemed to be wrong. Last but not least it was always fun having a smoke and coffee outside on the terrace. It was always a joyful experience.

Sebastian Heeg I thank him for introducing me to Raman scattering using the triple monochromators and the many fruitful discussions.

Antonio Setaro I thank him for being such a friendly guy, the nice discussions and the often so helpful advice. Especially for solving some of the many problems I had doing fancy stuff using Mathematica.

Heiko Dumlich I thank him for the many interesting discussions about theory and especially DFT. He is a really nice and cheerful guy. It was a pleasure to share the same home district with him and knowing what it means to live in the district of "Spandau".

Pascal Blümmel We shared an office together which was really fun. I thank him for showing me all the cool stuff on the web. It was really nice having him around and laughing so much about virtually everything.

Yvonne Demkiw Thanks for helping me out with all the chemical stuff I needed to do during my time in the group. It was really nice to share an office with her and being so cool and such a quick repartee.

Katayoun Gharagozloo-Hubmann I thank her for being always so helpful and caring so much about everyone. She helped me a lot with chemistry.

Mareen Gläske I thank her for being so nice and the good soul of our group. She helped me a lot by showing me how to make good nanotube solutions.

Gudrun May-Nasseri I thank her for doing all the administrative work and making things just work. She was a great help.

Jens Dreger, Philipp Neuser, Adrian Glaubitz, Andreas Ziehm They supported me very much when I was the IT guy of the group. I thank them for giving me all these many insights into big scale IT systems and their support by giving me access to the high-performance workstations to test my simulations. I learned a lot from them.

Roberto Fernandez-Garcia He helped me a lot in understanding the FDTD method and all these little things one simply does not think about then doing simulations. It was always nice meeting him and having a chat. Thanks a lot!

Kirsten Strain She was a great help in Scotland when doing measurements there. I thank her very much for the nice time in Edinburgh.

Aaron and Chaya Lewis, Andrey, Gabriel, Talia, Franziska, Celli I thank you very much for showing me Israel and the Jewish culture. You helped me to fit in this enlightening but difficult part of the world. I want to express my deepest gratitude for your help during the time of war and keeping me going and focused when fear was the only thing in my mind. Without you I would have never finished the research stay. You are the best examples that among all this hate and violence there is love and kindness. I will always remember you!

Cindy, Karoline I thank you for all the love and support during the endless weeks of measurements and the time of writing this thesis.

Isabell, Steve I thank you for helping me with the layout and the nice 3D pictures. They are true professionals.

My parents I thank you for making it possible for me to be the man I am. They supported me all my life. I will never forget that.

I would like to further thank all the people involved in writing the computer programs and tools I used in creating this thesis. Especially everyone who spent time to contribute to one of the numerous Open Source programs I used:

- Gnu/Linux
- Libreoffice
- KDE
- Kile
- Thunderbird and Firefox
- Meep
- JabRef
- LaTeX
- Mathematica
- Peak-o-Mat
- Origin
- Inkscape
- Gimp
- Bash
- Open-MPI
- SSH

Bibliography

[1] S. A. Maier. *Plasmonics: Fundamentals And Applications*. Springer, May 2007.

[2] G. Mie. Beiträge zur Optik trüber Medien, speziell kolloidaler Metallösungen. *Annalen der Physik*, 330(3):377–445, 1908. ISSN 1521-3889. doi: 10.1002/andp.19083300302.

[3] M. Fleischmann, P. J. Hendra, and Mcquilla A. J. Raman-spectra of pyridine adsorbed at a silver electrode. *Chemical Physics Letters*, 26(2):163–166, 1974. ISSN 0009-2614. doi: 10.1016/0009-2614(74)85388-1.

[4] K. A. Willets and R. P. Van Duyne. Localized surface plasmon resonance spectroscopy and sensing. *Annual Review of Physical Chemistry*, 58:267–297, 2007. doi: 10.1146/annurev.physchem.58.032806.104607.

[5] P. L. Stiles, J. A. Dieringer, N. C. Shah, and R. R. Van Duyne. Surface-enhanced Raman spectroscopy. *Annual Review of Analytical Chemistry*, 1:601–626, 2008. doi: 10.1146/annurev.anchem.1.031207.112814.

[6] S. M. Nie and S. R. Emery. Probing single molecules and single nanoparticles by surface-enhanced Raman scattering. *Science*, 275(5303):1102–1106, Feb 1997. doi: 10.1126/science.275.5303.1102.

[7] K. Kneipp, Y. Wang, H. Kneipp, L. T. Perelman, I. Itzkan, R. Dasari, and M. S. Feld. Single molecule detection using surface-enhanced Raman scattering (SERS). *Physical Review Letters*, 78(9):1667–1670, Mar 1997. doi: 10.1103/physrevlett.78.1667.

[8] E. C. Le Ru, E. Blackie, M. Meyer, and P. G. Etchegoin. Surface enhanced Raman scattering enhancement factors: A comprehensive study. *Journal of Physical Chemistry C*, 111(37):13794–13803, 2007. doi: 10.1021/jp0687908.

[9] M. Moskovits. Surface-enhanced Raman spectroscopy: a brief retrospective. *Journal of Raman Spectroscopy*, 36(6-7):485–496, Jun 2005. doi: 10.1002/jrs.1362.

[10] P. G. Etchegoin and E. C. Le Ru. A perspective on single molecule SERS: current status and future challenges. *Physical Chemistry Chemical Physics*, 10(40):6079–6089, 2008. ISSN 1463-9076. doi: 10.1039/b809196j.

[11] E. C. Le Ru, C. Galloway, and P. G. Etchegoin. On the connection between optical absorption/extinction and SERS enhancements. *Physical Chemistry Chemical Physics*, 8(26):3083–3087, 2006. ISSN 1463-9076. doi: 10.1039/b605292d.

[12] H. Metiu and P. Das. The electromagnetic theory of surface enhanced spectroscopy. *Annual Review of Physical Chemistry*, 35:507–536, 1984. doi: 10.1146/annurev.physchem.35.1.507.

[13] M. Kerker. Electromagnetic model for surface-enhanced Raman-scattering (SERS) on metal colloids. *Accounts of Chemical Research*, 17(8):271–277, 1984. doi: 10.1021/ar00104a002.

[14] A. Otto. The 'chemical' (electronic) contribution to surface-enhanced Raman scattering. *Journal of Raman Spectroscopy*, 36(6-7):497–509, Jun 2005. ISSN 0377-0486. doi: 10.1002/jrs.1355.

[15] J. R. Lombardi, R. L. Birke, T. H. Lu, and J. Xu. Charge-transfer theory of surface enhanced Raman-spectroscopy - Herzberg-Teller contributions. *Journal of Chemical Physics*, 84(8):4174–4180, Apr 1986. ISSN 0021-9606. doi: 10.1063/1.450037.

[16] N. Valley, N. Greeneltch, R. P. Van Duyne, and G. C. Schatz. A look at the origin and magnitude of the chemical contribution to the enhancement mechanism of surface-enhanced Raman spectroscopy (SERS): Theory and experiment. *Journal of Physical Chemistry Letters*, 4(16):2599–2604, Aug 2013. ISSN 1948-7185. doi: 10.1021/jz4012383.

[17] R. Fernandez-Garcia, Y. Sonnefraud, A. I. Fernandez-Dominguez, V. Giannini, and S. A. Maier. Design considerations for near-field enhancement in optical antennas. *Contemporary Physics*, 55(1):1–11, Jan 2014. ISSN 0010-7514. doi: 10.1080/00107514.2013.850788.

[18] U. S. Inan and R. A. Marshall. *Numerical Electromagnetics - The FDTD Method*. Cambridge University Press, 2011.

[19] A. Taflove and C. Hagness. *Computational Electrodynamics*. Artech House, 2005.

[20] V. R. Manfrinato, L. Zhang, D. Su, H. Duan, R. G. Hobbs, E. A. Stach, and K. K. Berggren. Resolution limits of electron-beam lithography toward the atomic

scale. *Nano Letters*, 13(4):1555–1558, Apr 2013. ISSN 1530-6984. doi: 10.1021/nl304715p.

[21] Vitor R. Manfrinato, Jianguo Wen, Lihua Zhang, Yujia Yang, Richard G. Hobbs, Bowen Baker, Dong Su, Dmitri Zakharov, Nestor J. Zaluzec, Dean J. Miller, Eric A. Stach, and Karl K. Berggren. Determining the resolution limits of electron-beam lithography: Direct measurement of the point-spread function. *Nano Letters*, 14(8):4406–4412, 2014. doi: 10.1021/nl5013773.

[22] A. L. Koh, K. Bao, I. Khan, W. E. Smith, G. Kothleitner, P. Nordlander, S. A. Maier, and D. W. McComb. Electron energy-loss spectroscopy (EELS) of surface plasmons in single silver nanoparticles and dimers: Influence of beam damage and mapping of dark modes. *ACS Nano*, 3(10):3015–3022, 2009. doi: 10.1021/nn900922z. PMID: 19772292.

[23] A. L. Koh, A. I. Fernandez-Dominguez, D. W. McComb, S. A. Maier, and J. K. W. Yang. High-resolution mapping of electron-beam-excited plasmon modes in lithographically defined gold nanostructures. *Nano Letters*, 11(3):1323–1330, Mar 2011. doi: 10.1021/nl104410t.

[24] M. Takase, H. Ajiki, Y. Mizumoto, K. Komeda, M. Nara, H. Nabika, S. Yasuda, H. Ishihara, and K. Murakoshi. Selection-rule breakdown in plasmon-induced electronic excitation of an isolated single-walled carbon nanotube. *Nature Photonics*, 7(7):550–554, Jul 2013. ISSN 1749-4885. doi: 10.1038/nphoton.2013.129.

[25] Y. Peng, C. Marcoux, P. Patoka, M. Hilgendorff, M. Giersig, and K. Kempa. Plasmonics of thin film quasitriangular nanoparticles. *Applied Physics Letters*, 96 (13):133104, Mar 2010. doi: 10.1063/1.3373918.

[26] S. Heeg, R. Fernandez-Garcia, A. Oikonomou, F. Schedin, R. Narula, S. A. Maier, A. Vijayaraghavan, and S. Reich. Polarized plasmonic enhancement by Au nanostructures probed through Raman scattering of suspended graphene. *Nano Letters*, 13(1):301–308, Jan 2013. doi: 10.1021/nl3041542.

[27] W. Zhu and K. B. Crozier. Quantum mechanical limit to plasmonic enhancement as observed by surface-enhanced Raman scattering. *Nature Communications*, 5, Oct 2014. ISSN 2041-1723. doi: 10.1038/ncomms6228.

[28] H Feilchenfeld and O Siiman. Surface raman excitation and enhancement profiles for chromate, molybdate, and tungstate on colloidal silver. *Journal Of Physical Chemistry*, 90(10):2163–2168, May 1986. ISSN 0022-3654. doi: 10.1021/j100401a035.

[29] A. D. McFarland, M. A. Young, J. A. Dieringer, and R. P. Van Duyne. Wavelength-scanned surface-enhanced Raman excitation spectroscopy. *Journal of Physical Chemistry B*, 109(22):11279–11285, Jun 2005. doi: 10.1021/jp050508u.

[30] W. Ni, T. Ambjörnsson, S. P. Apell, H. Chen, and J. Wang. Observing plasmonic molecular resonance coupling on single gold nanorods. *Nano Letters*, 10(1):77–84, 2010. doi: 10.1021/nl902851b. PMID: 19957966.

[31] D. P. Fromm, A. Sundaramurthy, P. J. Schuck, G. Kino, and W. E. Moerner. Gap-dependent optical coupling of single "Bowtie" nanoantennas resonant in the visible. *Nano Letters*, 4(5):957–961, May 2004. ISSN 1530-6984. doi: 10.1021/nl049951r.

[32] 20.7. 2008. URL http://ab-initio.mit.edu/wiki/index.php/Meep_acronym_expansions.

[33] J. D. Jackson. *Klassische Elektrodynamik*. Walter de Gruyter, 4th edition, June 2006.

[34] C. Klingshirn. *Semiconductor Optics*. Springer, 3rd edition, 2006.

[35] L. Tonks and I. Langmuir. Oscillations in ionized gases. *Physical Review*, 33: 195–210, Feb 1929. doi: 10.1103/physrev.33.195.

[36] H. Yan, T. Low, W. Zhu, Y. Wu, M. Freitag, X. Li, F. Guinea, P. Avouris, and F. Xia. Damping pathways of mid-infrared plasmons in graphene nanostructures. *Nature Photonics*, 7(5):394–399, May 2013. ISSN 1749-4885. doi: 10.1038/nphoton.2013.57.

[37] A. D. Rakic, A. B. Djurisic, J. M. Elazar, and M. L. Majewski. Optical properties of metallic films for vertical-cavity optoelectronic devices. *Applied Optics*, 37(22): 5271–5283, Aug 1998. ISSN 0003-6935. doi: 10.1364/ao.37.005271.

[38] B. E. A. Saleh and M. C. Teich. *Fundamentals of Photonics*. John Wiley & Sons, 2007.

[39] H. Vortisch. *Beobachtung von Phasenübergängen in einzelnen levitierten Schwefelsäuretröpfchen mittels Raman-Spektroskopie und elastischer Lichtstreuung*. PhD thesis, FU Berlin, 2002.

[40] J. A. Stratton. *Electromagnetic Theory*. McGraw-Hill Book Company, 1941.

[41] K. F. Riley, M. P. Hobson, and S. J. Bence. *Mathematical Methods for Physics and Engineering*. Cambrigde University Press, 3rd edition, 2006.

[42] 4.4. 2015. URL http://en.wikipedia.org/wiki/Computational_electromagnetics.

[43] C. Lanczos. An iteration method for the solution of the eigenvalue problem of linear differential and integral operators. *Journal of Research of the National Bureau of Standards*, 45(4):255–282, 1950. ISSN 0091-0635. doi: 10.6028/jres.045.026.

[44] A. F. Oskooi, D. Roundy, M. Ibanescu, P. Bermel, J. D. Joannopoulos, and S. G. Johnson. MEEP: A flexible free-software package for electromagnetic simulations by the FDTD method. *Computer Physics Communications*, 181(3):687–702, Mar 2010. ISSN 0010-4655. doi: 10.1016/j.cpc.2009.11.008.

[45] K. S. Yee. Numerical solution of initial boundary value problems involving Maxwells equations in isotropic media. *IEEE Transactions on Antennas and Propagation*, AP14(3):302–&, 1966. ISSN 0018-926X.

[46] R. Courant, K. Friedric, and H. Lewy. On partial difference equations of mathematical physics. *IBM Journal of Research and Development*, 11(2):215, 1967. ISSN 0018-8646.

[47] J. Crank and P. Nicolson. A practical method for numerical evaluation of solutions of partial differential equations of the heat-conduction type. *Proceedings Of The Cambridge Philosophical Society*, 43(1):50–67, 1947.

[48] 25.4. 2014. URL http://ab-initio.mit.edu/wiki/index.php/Meep_Reference.

[49] J. P. Berenger. A perfectly matched layer for the absorption of electromagnetic-waves. *Journal of Computational Physics*, 114(2):185–200, Oct 1994. ISSN 0021-9991. doi: 10.1006/jcph.1994.1159.

[50] 12.2. 2015. URL http://ab-initio.mit.edu/wiki/index.php/Dielectric_materials_in_Meep.

[51] A. Farjadpour, D. Roundy, A. Rodriguez, M. Ibanescu, P. Bermel, J. D. Joannopoulos, S. G. Johnson, and G. W. Burr. Improving accuracy by subpixel smoothing in the finite-difference time domain. *Optics Letters*, 31(20):2972–2974, Oct 2006. ISSN 0146-9592. doi: 10.1364/ol.31.002972.

[52] M. Meier and A. Wokaun. Enhanced fields on large metal particles - dynamic depolarization. *Optics Letters*, 8(11):581–583, 1983. ISSN 0146-9592. doi: 10.1364/ol.8.000581.

[53] A. Bouhelier, R. Bachelot, J. S. Im, G. P. Wiederrecht, G. Lerondel, S. Kostcheev, and P. Royer. Electromagnetic interactions in plasmonic nanoparticle arrays. *Journal of Physical Chemistry B*, 109(8):3195–3198, Mar 2005. doi: 10.1021/jp043224b.

[54] H. Fischer and O. J. F. Martin. Engineering the optical response of plasmonic nanoantennas. *Optics Express*, 16(12):9144–9154, Jun 2008.

[55] K. Kolwas and A. Derkachova. Plasmonic abilities of gold and silver spherical nanoantennas in terms of size dependent multipolar resonance frequencies and plasmon damping rates. *Opto-electronics Review*, 18(4):429–437, Dec 2010. doi: 10.2478/s11772-010-0043-6.

[56] I. Zoric, M. Zach, B. Kasemo, and C. Langhammer. Gold, platinum, and aluminum nanodisk plasmons: Material independence, subradiance, and damping mechanisms. *ACS Nano*, 5(4):2535–2546, Apr 2011. ISSN 1936-0851. doi: 10.1021/nn102166t.

[57] W. Rechberger, A. Hohenau, A. Leitner, J. R. Krenn, B. Lamprecht, and F. R. Aussenegg. Optical properties of two interacting gold nanoparticles. *Optics Communications*, 220(1-3):137–141, May 2003. ISSN 0030-4018. doi: 10.1016/S0030-4018(03)01357-9.

[58] I. H. Malitson. Interspecimen comparison of refractive index of fused silica. *Journal of the Optical Society of America*, 55(10P1):1205–&, 1965. ISSN 0030-3941. doi: 10.1364/josa.55.001205.

[59] G. F. Walsh, C. Forestiere, and L. Dal Negro. Plasmon-enhanced depolarization of reflected light from arrays of nanoparticle dimers. *Optics Express*, 19(21):21081–21090, Oct 2011. ISSN 1094-4087. doi: 10.1364/OE.19.021081.

[60] A. L. Demming, F. Festy, and D. Richards. Plasmon resonances on metal tips: Understanding tip-enhanced Raman scattering. *Journal of Chemical Physics*, 122 (18):184716, May 2005. doi: 10.1063/1.1896356.

[61] N. Calander, I. Gryczynski, and Z. Gryczynski. Interference of surface plasmon resonances causes enhanced depolarized light scattering from metal nanoparticles. *Chemical Physics Letters*, 434(4–6):326 – 330, 2007. ISSN 0009-2614. doi: 10.1016/j.cplett.2006.12.003.

[62] C. Hubert, R. Bachelot, J. Plain, S. Kostcheev, G. Lerondel, M. Juan, P. Royer, S. Zou, G. C. Schatz, G. P. Wiederrecht, and S. K. Gray. Near-field polarization effects in molecular-motion-induced photochemical imaging. *Journal Of Physical Chemistry C*, 112(11):4111–4116, Mar 2008. ISSN 1932-7447. doi: 10.1021/jp7096263.

[63] P. Etchegoin, L. F. Cohen, H. Hartigan, R. J. C. Brown, M. J. T. Milton, and J. C. Gallop. Electromagnetic contribution to surface enhanced Raman scattering

revisited. *Journal of Chemical Physics*, 119(10):5281–5289, Sep 2003. ISSN 0021-9606. doi: 10.1063/1.1597480.

[64] F. J. GarciaVidal and J. B. Pendry. Collective theory for surface enhanced Raman scattering. *Physical Review Letters*, 77(6):1163–1166, Aug 1996. ISSN 0031-9007. doi: 10.1103/physrevlett.77.1163.

[65] L. M. Malard, M. A. Pimenta, G. Dresselhaus, and M. S. Dresselhaus. Raman spectroscopy in graphene. *Physics Reports-review Section of Physics Letters*, 473 (5-6):51–87, Apr 2009. ISSN 0370-1573. doi: 10.1016/j.physrep.2009.02.003.

[66] S. Reich, J. Maultzsch, C. Thomsen, and P. Ordejon. Tight-binding description of graphene. *Physical Review B*, 66(3), Jul 2002. ISSN 1098-0121. doi: 10.1103/physrevb.66.035412.

[67] M. Lazzeri, C. Attaccalite, L. Wirtz, and F. Mauri. Impact of the electron-electron correlation on phonon dispersion: Failure of LDA and GGA DFT functionals in graphene and graphite. *Physical Review B*, 78(8), Aug 2008. ISSN 1098-0121. doi: 10.1103/physrevb.78.081406.

[68] W. Kohn. Image of the Fermi surface in the vibration spectrum of a metal. *Physical Review Letters*, 2(9):393–394, 1959. ISSN 0031-9007. doi: 10.1103/physrevlett.2.393.

[69] S. Piscanec, M. Lazzeri, F. Mauri, A. C. Ferrari, and J. Robertson. Kohn anomalies and electron-phonon interactions in graphite. *Physical Review Letters*, 93(18), Oct 2004. ISSN 0031-9007. doi: 10.1103/physrevlett.93.185503.

[70] P. R. Wallace. The band theory of graphite. *Physical Review*, 71(9):622–634, 1947. ISSN 0031-899X. doi: 10.1103/physrev.71.622.

[71] R. Saito, G. Dresselhaus, and M. S. Dresselhaus. Trigonal warping effect of carbon nanotubes. *Physical Review B*, 61(4):2981–2990, Jan 2000. ISSN 1098-0121. doi: 10.1103/physrevb.61.2981.

[72] G. G. Samsonidze, R. Saito, A. Jorio, A. G. Souza, A. Gruneis, M. A. Pimenta, G. Dresselhaus, and M. S. Dresselhaus. Phonon trigonal warping effect in graphite and carbon nanotubes. *Physical Review Letters*, 90(2), Jan 2003. ISSN 0031-9007. doi: 10.1103/physrevlett.90.027403.

[73] P. Yu and M. Cardona. *Fundamentals of Semiconductors*. Springer, 4th edition, Mar 2010.

[74] C. Hamaguchi. *Basic Semiconductor Physics*. Springer, 2nd edition, Sptember 2009.

[75] C.V. Raman. A new type of secondary radiation. *Nature*, 121:501–502, 1928.

[76] S. Reich, C. Thomsen, and J. Maultzsch. *Carbon Nanotubes*. Wiley-VCH, 2004.

[77] C. Kittel. *Einführung in die Festkörperphysik*. Oldenbourg, 14th edition, 2006.

[78] S. Hunklinger. *Festkörperphysik*. Oldenbourg, 3rd edition, 2011.

[79] L. Van Hove. The occurrence of singularities in the elastic frequency distribution of a crystal. *Physical Review*, 89(6):1189–1193, 1953. ISSN 0031-899X. doi: 10.1103/physrev.89.1189.

[80] R. Narula, R. Panknin, and S. Reich. Absolute Raman matrix elements of graphene and graphite. *Physical Review B*, 82(4), Jul 2010. ISSN 1098-0121. doi: 10.1103/PhysRevB.82.045418.

[81] R. Narula and S. Reich. Graphene band structure and its 2D Raman mode. *Physical Review B*, 90(8), Aug 2014. ISSN 1098-0121. doi: 10.1103/physrevb.90.085407.

[82] C. Thomsen and S. Reich. Double resonant Raman scattering in graphite. *Physical Review Letters*, 85(24):5214–5217, Dec 2000. ISSN 0031-9007. doi: 10.1103/physrevlett.85.5214.

[83] A. C. Ferrari. Raman spectroscopy of graphene and graphite: Disorder, electron-phonon coupling, doping and nonadiabatic effects. *Solid State Communications*, 143(1-2):47–57, Jul 2007. ISSN 0038-1098. doi: 10.1016/j.ssc.2007.03.052.

[84] J. Maultzsch, S. Reich, and C. Thomsen. Double-resonant Raman scattering in graphite: Interference effects, selection rules, and phonon dispersion. *Physical Review B*, 70(15):155403, Oct 2004. doi: 10.1103/physrevb.70.155403.

[85] P. Venezuela, M. Lazzeri, and F. Mauri. Theory of double-resonant Raman spectra in graphene: Intensity and line shape of defect-induced and two-phonon bands. *Physical Review B*, 84(3), Jul 2011. ISSN 1098-0121. doi: 10.1103/physrevb.84.035433.

[86] R. Narula, N. Bonini, N. Marzari, and S. Reich. Dominant phonon wave vectors and strain-induced splitting of the 2D Raman mode of graphene. *Physical Review B*, 85(11), Mar 2012. ISSN 1098-0121. doi: 10.1103/physrevb.85.115451.

[87] S. Berciaud, X. Li, H. Htoon, L. E. Brus, S. K. Doorn, and T. F. Heinz. Intrinsic line shape of the Raman 2D-mode in freestanding graphene monolayers. *Nano Letters*, 13(8):3517–3523, Aug 2013. ISSN 1530-6984. doi: 10.1021/nl400917e.

[88] V. N. Popov and P. Lambin. Theoretical polarization dependence of the two-phonon double-resonant Raman spectra of graphene. *European Physical Journal B*, 85(12), Dec 2012. ISSN 1434-6028. doi: 10.1140/epjb/e2012-30684-x.

[89] R. Narula, N. Bonini, N. Marzari, and S. Reich. Dominant phonon wavevectors of the 2D Raman mode of graphene. *Physica Status Solidi B*, 248(11):2635–2638, Nov 2011. ISSN 0370-1972. doi: 10.1002/pssb.201100510.

[90] M. Huang, H. Yan, T. F. Heinz, and J. Hone. Probing strain-induced electronic structure change in graphene by Raman spectroscopy. *Nano Letters*, 10(10):4074–4079, Oct 2010. ISSN 1530-6984. doi: 10.1021/nl102123c.

[91] V. M. Pereira, A. H. C. Neto, and N. M. R. Peres. Tight-binding approach to uniaxial strain in graphene. *Physical Review B*, 80(4), Jul 2009. ISSN 1098-0121. doi: 10.1103/physrevb.80.045401.

[92] M. Mohr, K. Papagelis, J. Maultzsch, and C. Thomsen. Two-dimensional electronic and vibrational band structure of uniaxially strained graphene from ab initio calculations. *Physical Review B*, 80(20), Nov 2009. ISSN 1098-0121. doi: 10.1103/physrevb.80.205410.

[93] M. Mohr, J. Maultzsch, and C. Thomsen. Splitting of the Raman 2D band of graphene subjected to strain. *Physical Review B*, 82(20), Nov 2010. ISSN 1098-0121. doi: 10.1103/physrevb.82.201409.

[94] S. Reich, H. Jantoljak, and C. Thomsen. Shear strain in carbon nanotubes under hydrostatic pressure. *Physical Review B*, 61(20):13389–13392, May 2000. ISSN 1098-0121.

[95] T. M. G. Mohiuddin, A. Lombardo, R. R. Nair, A. Bonetti, G. Savini, R. Jalil, N. Bonini, D. M. Basko, C. Galiotis, N. Marzari, K. S. Novoselov, A. K. Geim, and A. C. Ferrari. Uniaxial strain in graphene by Raman spectroscopy: G peak splitting, Grüneisen parameters, and sample orientation. *Physical Review B*, 79 (20), May 2009. ISSN 1098-0121. doi: 10.1103/physrevb.79.205433.

[96] R.M Martin and L.M. Falicov. *Light Scattering in Solids I*, volume 1, chapter 3, pages 79–145. Springer-Verlag, 1983.

[97] E. Hecht. *Optik*. Oldenbourg, 2009.

[98] R. R. Nair, P. Blake, A. N. Grigorenko, K. S. Novoselov, T. J. Booth, T. Stauber, N. M. R. Peres, and A. K. Geim. Fine structure constant defines visual transparency of graphene. *Science*, 320(5881):1308, Jun 2008. ISSN 0036-8075. doi: 10.1126/science.1156965.

[99] A. Kosiorek, W. Kandulski, P. Chudzinski, K. Kempa, and M. Giersig. Shadow nanosphere lithography: Simulation and experiment. *Nano Letters*, 4(7):1359–1363, Jul 2004. ISSN 1530-6984. doi: 10.1021/nl049361t.

[100] V. Geringer, M. Liebmann, T. Echtermeyer, S. Runte, M. Schmidt, R. Rueckamp, M. C. Lemme, and M. Morgenstern. Intrinsic and extrinsic corrugation of monolayer graphene deposited on SiO_2. *Physical Review Letters*, 102(7), Feb 2009. ISSN 0031-9007. doi: 10.1103/physrevlett.102.076102.

[101] J. M. McMahon, A.-I. Henry, K. L. Wustholz, M. J. Natan, R. G. Freeman, R. P. Van Duyne, and G. C. Schatz. Gold nanoparticle dimer plasmonics: finite element method calculations of the electromagnetic enhancement to surface-enhanced Raman spectroscopy. *Analytical and Bioanalytical Chemistry*, 394(7):1819–1825, Aug 2009. ISSN 1618-2642. doi: 10.1007/s00216-009-2738-4.

[102] A. Das, B. Chakraborty, and A. K. Sood. Raman spectroscopy of graphene on different substrates and influence of defects. *Bulletin of Materials Science*, 31(3): 579–584, Jun 2008. doi: 10.1007/s12034-008-0090-5.

[103] C.-F. Chen, C.-H. Park, B. W. Boudouris, J. Horng, B. Geng, C. Girit, A. Zettl, M. F. Crommie, R. A. Segalman, S. G. Louie, and F. Wang. Controlling inelastic light scattering quantum pathways in graphene. *Nature*, 471(7340):617–620, Mar 2011. ISSN 0028-0836. doi: 10.1038/nature09866.

[104] V. N. Popov and P. Lambin. Theoretical 2D Raman band of strained graphene. *Physical Review B*, 87(15), Apr 2013. ISSN 1098-0121. doi: 10.1103/physrevb.87.155425.

[105] J. Zabel, R. R. Nair, A. Ott, T. Georgiou, A. K. Geim, K. S. Noyoselov, and C. Casiraghi. Raman spectroscopy of graphene and bilayer under biaxial strain: Bubbles and balloons. *Nano Letters*, 12(2):617–621, Feb 2012. ISSN 1530-6984. doi: 10.1021/nl203359n.

The End ...